



STRUCTURAL STABILITY OF A
JOINED-WING SENSORCRAFT

THESIS

Brandon J. Adams, Ensign, USN

AFIT/GAE/ENY/07-J01

DEPARTMENT OF THE AIR FORCE
AIR UNIVERSITY

AIR FORCE INSTITUTE OF TECHNOLOGY

Wright-Patterson Air Force Base, Ohio

APPROVED FOR PUBLIC RELEASE; DISTRIBUTION UNLIMITED.

The views expressed in this thesis are those of the author and do not reflect the official policy or position of the United States Air Force, Department of Defense, or the U.S. Government.

**STRUCTURAL STABILITY OF A
JOINED-WING SENSORCRAFT**

THESIS

Presented to the Faculty

Department of Aeronautical and Astronautical Engineering

Graduate School of Engineering and Management

Air Force Institute of Technology

Air University

Air Education and Training Command

In Partial Fulfillment of the Requirements for the
Degree of Master of Science in Aeronautical Engineering

Brandon J. Adams, BS

Ensign, USN

June 2007

APPROVED FOR PUBLIC RELEASE; DISTRIBUTION UNLIMITED

STRUCTURAL STABILITY OF A JOINED-WING SENSORCRAFT

Brandon J. Adams BS
Ensign, USN

Approved:

//SIGNED//

Dr. Robert A. Canfield (Chairman)

_____ Date

//SIGNED//

Dr. Donald Kunz (Member)

_____ Date

//SIGNED//

Maj. Eric Swenson (Member)

_____ Date

Abstract

This thesis employed a multi-disciplinary design approach to determine the structural stability of the Boeing Joined-Wing SensorCraft. Specifically, this thesis sought to characterize the free vibration modes, ensure a buckling safe design and determine the influence of the geometric and aeroelastic nonlinearities associated with this joined-wing design. The clamped-free vibration modes were developed for a wind tunnel model and were compared to the free-free vibration modes, several differences were found. Linear static analyses were performed on numerous maneuver loads and gust conditions to determine the critical loading condition. The SensorCraft was then redesigned for the critical load case to be both panel and global buckling safe. The multi-disciplinary design process which incorporated both geometric nonlinearities and aeroelastic follower-force effects was then performed for the pre-gust trim and critical gust conditions. The resulting analysis showed that the deformations that resulted from the aerodynamic forces were not substantial enough to fully characterize the follower force effect. Furthermore this thesis demonstrates that the geometric and aeroelastic nonlinearities are not significant. However, for a fully optimized design incorporation of these coupled nonlinearities is critical.

Acknowledgments

I would like to express my sincere appreciation to my thesis advisor, Dr. Robert Canfield, for his guidance and instruction throughout this thesis. His patience and availability were immensely appreciated.

I would also like to thank Lt. Col. Vanessa Bond and Dr. Adrian Viisoreanu for their software support and technical perspective provided to me in this thesis as well as Mitch Williams for his grammatical expertise. Their quick and accurate advice saved me a tremendous amount of time.

Finally, I would like to thank my wife for her never ending patience and selflessness. Her love and support toward me during this endeavor have made this possible.

Yet those who wait for the Lord will gain new strength; they will mount up with wings like eagles, they will run and not get tired, they will walk and not become weary.

Isaiah 40:31

Brandon J. Adams

Table of Contents

	Page
ABSTRACT	IV
ACKNOWLEDGMENTS	V
TABLE OF CONTENTS.....	VI
LIST OF FIGURES.....	VIII
LIST OF TABLES	X
LIST OF SYMBOLS	XI
I. INTRODUCTION	1
<i>Inspiration</i>	1
<i>Overview</i>	2
<i>Problem Statement</i>	6
<i>Research Objective</i>	8
<i>Wind Tunnel Model Development</i>	8
<i>Material Search</i>	9
<i>Normal Modes Analysis</i>	9
<i>Structural Optimization & Aeroelastic Analysis</i>	10
<i>Linear Static Analysis</i>	10
<i>Linear Buckling Analysis</i>	10
<i>Normal Modes Analysis</i>	11
<i>Nonlinear Static Analysis</i>	11
II. LITERATURE REVIEW	13
<i>Introduction.....</i>	13
<i>Joined-Wing Review</i>	13
<i>SensorCraft Review</i>	20
<i>Structural Lay-up of wings.....</i>	22
<i>Normal Modes Analysis</i>	24
<i>Aeroelastic Structural Analysis</i>	24
<i>Roll, Push-Over, Pull-Up.....</i>	25
<i>Gust.....</i>	25
<i>Basis for Current Research</i>	27
III. METHODOLOGY.....	29
<i>Radar Material Search.....</i>	29
<i>Normal Modes Analysis</i>	30
<i>MSC.Nastran Normal Modes Analysis</i>	33
<i>Linear Static Analysis</i>	34
<i>Linear Buckling Analysis</i>	37
<i>MSC.Nastran Buckling Analysis</i>	39
<i>Nonlinear Static Analysis</i>	41
<i>Analysis Setup</i>	41
<i>Matlab.....</i>	41
<i>Zaero Trim</i>	43
<i>Zaero Gust</i>	44
<i>MSC.Nastran Nonlinear Analysis</i>	50

	Page
<i>Procedure</i>	56
<i>Analysis 1 – Undeformed Aerodynamic & Linear Structural Analysis</i>	58
<i>Analysis 2 - Undeformed Aerodynamic & Nonlinear Structural Analysis</i>	58
<i>Analysis 3 – Flexible Aerodynamic & Nonlinear Structural Analysis</i>	59
<i>Flight Loads</i>	60
IV. RESULTS	63
<i>Material Search</i>	63
<i>Normal Modes Analysis</i>	68
<i>Linear Static Analysis</i>	74
<i>Buckling Analysis</i>	78
<i>Nonlinear Aeroelastic & Nonlinear Structural Static Analysis</i>	83
V. CONCLUSIONS AND RECOMMENDATIONS	96
<i>Boeing Joined-Wing SensorCraft</i>	96
<i>Aerodynamic and Structural Coupling</i>	97
<i>Structural Aeroelastic Analysis Transient Response</i>	98
<i>Recommendations</i>	99
APPENDIX A	100
<i>Modes 5-10 for the Clamped Normal Modes Analysis</i>	100
<i>Modes 1-6 for Free-Free Normal Modes Analysis</i>	101
APPENDIX B	102
<i>Zaero 1G Trim Input</i>	102
<i>Zaero 2.50 Second Discrete Gust Input</i>	103
<i>Nastran Nonlinear Initial Input</i>	105
<i>Nastran Restarted Gust Input</i>	107
APPENDIX C	108
<i>Other Material around Radar Arrays</i>	108
APPENDIX D	109
<i>Gust Load Stress Results</i>	109
APPENDIX E	110
<i>Displacements from Static Loads</i>	110
BIBLIOGRAPHY	113

List of Figures

Figure	Page
1. SENSORCRAFT MISSION PROFILE [14]	2
2. TOP VIEW OF BOEING SENSORCRAFT	3
3. PROFILE VIEW OF BOEING SENSORCRAFT	3
4. FRONT VIEW OF BOEING SENSORCRAFT	4
5. CONFORMAL LOAD-BEARING ANTENNA STRUCTURE CROSS-SECTION	6
6. CANTED NORMAL FORCE IN JOINED-WING PLANE [11].....	15
7. OPTIMAL JOINED-WING STRUCTURE Vs. CANTILEVER WING STRUCTURE [3]	15
8. IN PLANE BENDING COMPARISON OF CONVENTIONAL AND JOINED-WING STRUCTURES [5]	17
9. STABILITY OF BUCKLED STRUCTURE DEPENDING ON FLIGHT CONDITIONS [8]	19
10. COMPARISON BETWEEN LINEAR AND NON-LINEAR WING-TIP DEFLECTION [13]	22
11. WING CROSS-SECTION AND SENSOR LAYOUT [14]	24
12. RADAR ARRAYS LOCATIONS [17]	29
13. LOCATION OF CLAMPED/SUPPORTED NODE FOR NORMAL MODES ANALYSES	31
14. AERODYNAMIC PANEL MODEL	41
15. GUST LENGTH PROFILES COMPARISON	48
16. NEWTON-RAPHSON METHOD	53
17. MODIFIED NEWTON METHOD	54
18. NON-CONVERGENCE EXAMPLE	54
19. FLOW CHART OF NONLINEAR ANALYSIS	57
20. ACCELERATION OF WINGTIP DURING 2.50 SECONDS GUST & LOAD TIMES	62
21. LOCATIONS IN SENSORCRAFT WHERE MATERIALS 7, 9, & 8552 ARE USED	64
22. EXTERNAL VIEW OF MATERIALS 7, 9, & 8552 IN THE SENSORCRAFT	66
23. COMPOSITE LAY-UP OF MATERIALS 7, 9, & 8552	67
24. LOCATION OF USE AND MATERIAL PROPERTIES FOR MATERIAL 2	68

	Page
25. FIRST FOUR NON-RIGID BODY MODES FOR FREE-FREE NORMAL MODES ANALYSIS.....	70
26. LOCATION OF CG AND CONSTRAINED NODE	71
27. FIRST FOUR NORMAL MODES FOR CLAMPED ANALYSIS	73
28. LOCATIONS WHERE ROD, PLATE, LAMINATE AND SOLID ELEMENTS ARE USED.....	76
29. STRESS COMPARISON FOR FOUR ELEMENT TYPES	77
30. PANEL BUCKLING IN SENSORCRAFT.....	79
31. FIRST GLOBAL BUCKLING MODE.....	80
32. SECOND GLOBAL BUCKLING MODE.....	81
33. FIRST GLOBAL BUCKLING MODE FOR UNMODIFIED MODEL	82
34. WINGTIP ACCELERATION TIME HISTORY FOR A GUST LENGTH OF 1.25 SECONDS.....	84
35. EFFECTIVE ANGLE OF ATTACK CALCULATION	85
36. COMPARISON OF MAXIMUM DEFLECTION FOR TRIM AND GUST ANALYSIS.....	87
37. PROFILE VIEW OF PEAK GUST DEFLECTION.....	89
38. WINGTIP ACCELERATION TIME HISTORY FOR 2.50 SECOND GUST	91
39. TIME HISTORY DEFORMATION FOR 2.50 SECOND GUST	93
40. WINGTIP ACCELERATION TIME HISTORY FOR 3.75 SECOND GUST	94
41. AERODYNAMIC PANEL MODEL COMPARISON	95
42. USE OF MATERIAL 1 THROUGHOUT SENSORCRAFT	108
43. USE OF MATERIAL 8 THROUGHOUT SENSORCRAFT	108
44. GUST LOAD DEFORMATIONS & MAGNITUDE OF MAXIMUM DISPLACEMENT	110
45. PULL-UP LOAD DEFORMATIONS & MAGNITUDE OF MAXIMUM DISPLACEMENT	111
46. PUSH-OVER LOAD DEFORMATIONS & MAGNITUDE OF MAXIMUM DISPLACEMENT	111
47. ROLL LOAD DEFORMATIONS & MAGNITUDE OF MAXIMUM DISPLACEMENT	112

List of Tables

Table	Page
1. COMPARISON OF LOAD CASES	26
2. APPLIED LOAD AND DISPLACEMENT COMPARISON	27
3. LOCATION OF CENTER OF GRAVITY AND CONSTRAINED/SUPPORTED NODES.....	30
4. PUSH-OVER, PULL-UP, & ROLL LOAD SET DESCRIPTIONS	35
5. GUST LOAD SET DESCRIPTION.....	35
6. ADJUSTED COMPOSITE PROPERTIES TO PREVENT PANEL BUCKLING.....	39
7. TRIMMED FLIGHT ANALYSIS INPUTS	44
8. TRANSIENT GUST ANALYSIS INPUTS.....	45
9. CALCULATED REDUCED FREQUENCIES.....	49
10. REDUCED FREQUENCIES	50
11. MATERIAL PROPERTIES FOR MATERIALS 7, 9, & 8552.....	65
12. DESCRIPTION OF NORMAL MODES FOR FREE-FREE MODEL	69
13. NORMAL MODES DESCRIPTION FOR CLAMPED MODEL	72
14. RANKING OF LOAD SETS BASED ON NUMBER OF HITS.....	75
15. DISPLACEMENT COMPARISON FOR CRITICAL LOAD CASES	78
16. 1G TRIM DETAILS FOR SENSORCRAFT.....	84
17. EFFECTIVE ANGLES OF ATTACK, GUST ALLEVIATION FACTOR, AND LOAD FACTOR.....	86
18. GUST DEFLECTION COMPARISON FOR ESTIMATION AND ANALYTICAL SOLUTIONS.....	86
19. COMPARISON OF MAXIMUM ACCELERATIONS AND DEFLECTIONS.....	88
20. COMPARISON OF ANALYSIS TECHNIQUES	89
21. ACTUAL DISPLACEMENT TIME HISTORY	92

List of Symbols

Symbol	Definition
α	Angle of Attack
α_E	Effective Angle of Attack
ρ	Air Density
ϵ	Strain
σ	Stress
σ_e	VonMises Stress
μ	Mass Ratio
C_{la}	Slope of $C_L - \alpha$
C_L	Coefficient of Lift
F_a	Aerodynamic Forces
F_e	External Forces
g	Acceleration Due to Gravity
c	Wing Chord Length
ν	Poison's Ratio
E	Elastic Modulus
G	Shear Modulus
x, y, z	Cartesian Coordinates
u, v, w	Displacements in Cartesian Coordinates
θ	Euler Pitch Angle
K	Stiffness Matrix, Gust Alleviation Factor
L	Lift

Symbol	Definition
S	Span, Wing Surface Area
V.....	Velocity
W.....	Weight
Xc.g.....	Center of Gravity Location
Xa.c.....	Aerodynamic Center Location
H.....	Altitude
Q.....	Pitch Rate
LG	Gust Length
M.....	Mass Matrix
CG	Center of Gravity
$Q_{hG}(ik)$	Generalized Aerodynamic Gust Forces In Time Domain

STRUCTURAL STABILITY OF A JOINED-WING SENSORCRAFT

I. Introduction

Inspiration

The development of Boeing's Joined-Wing SensorCraft stems from the Air Force's need for a new more capable surveillance aircraft. The driving factors behind the unique design of the SensorCraft are the necessity to maintain 360 degree radar coverage over the target area and expand the current capabilities of current unmanned aerial vehicles mission profile capabilities. That is, to perform high altitude surveillance with increased range and endurance. The current mission profile for the SensorCraft includes a gradual ingress to 55,000 feet, a 24 hour loiter between 55,000 feet and 65,000 feet over the target region, and a gradual egress back to ground level [12]. The driving requirement in the Airforce Research Laboratory/Air Vehicles (AFRL/AV) sizing studies is the *capability* of loitering at 55,000 feet at the top of climb (ToC) after a maximum takeoff gross weight (MTOGW) takeoff [14]. Figure 1 shows the proposed mission profile for the SensorCraft.

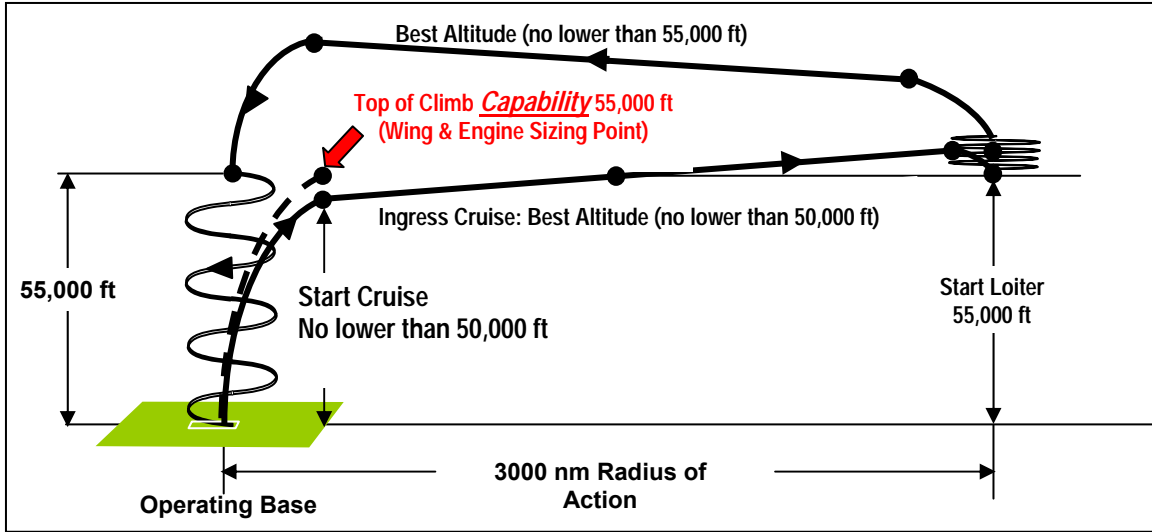


Figure 1: SensorCraft Mission Profile [14]

Overview

The Boeing SensorCraft concept employs a joined-wing layout as well as several other innovative ideas in order to enhance its mission capabilities. The layout of the SensorCraft follows the typical joined-wing description in that, if the aircraft is viewed from above or in front, the wing layout forms a diamond shape. To accomplish this, the forward wings are swept aft and the aft wings are swept forward. Figures 2, 3, and 4 provide top, profile, and front views of the SensorCraft, respectively.

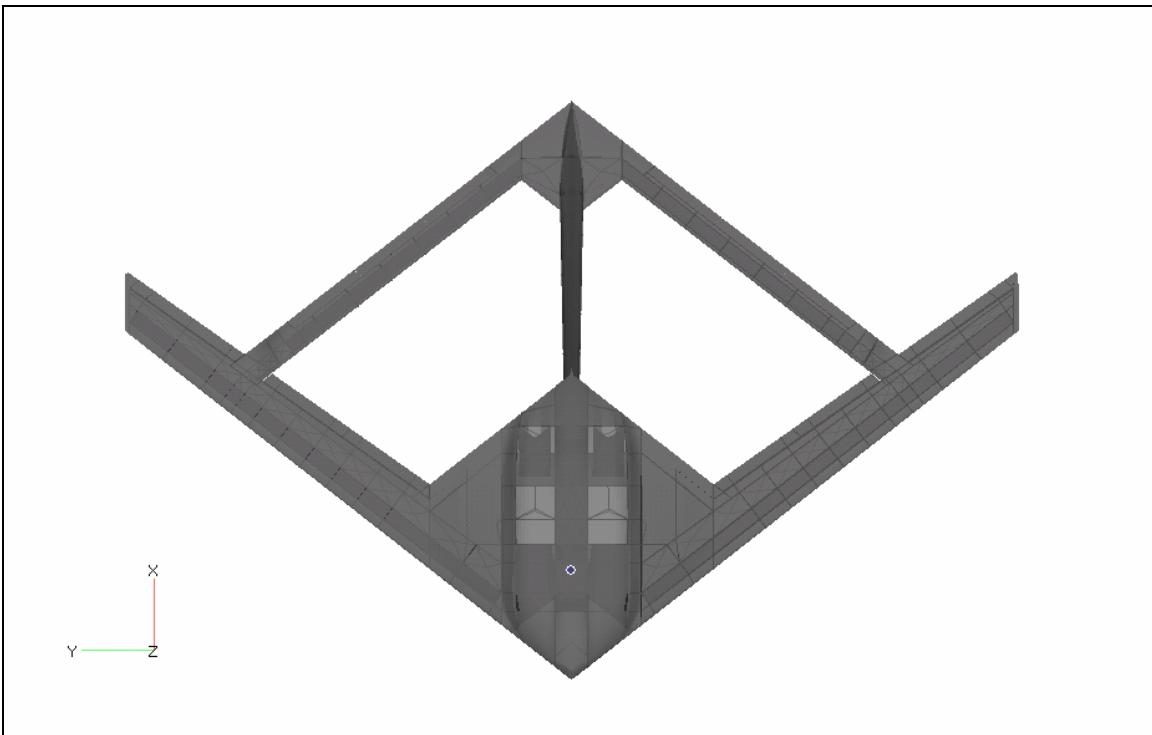


Figure 2: Top View of Boeing SensorCraft

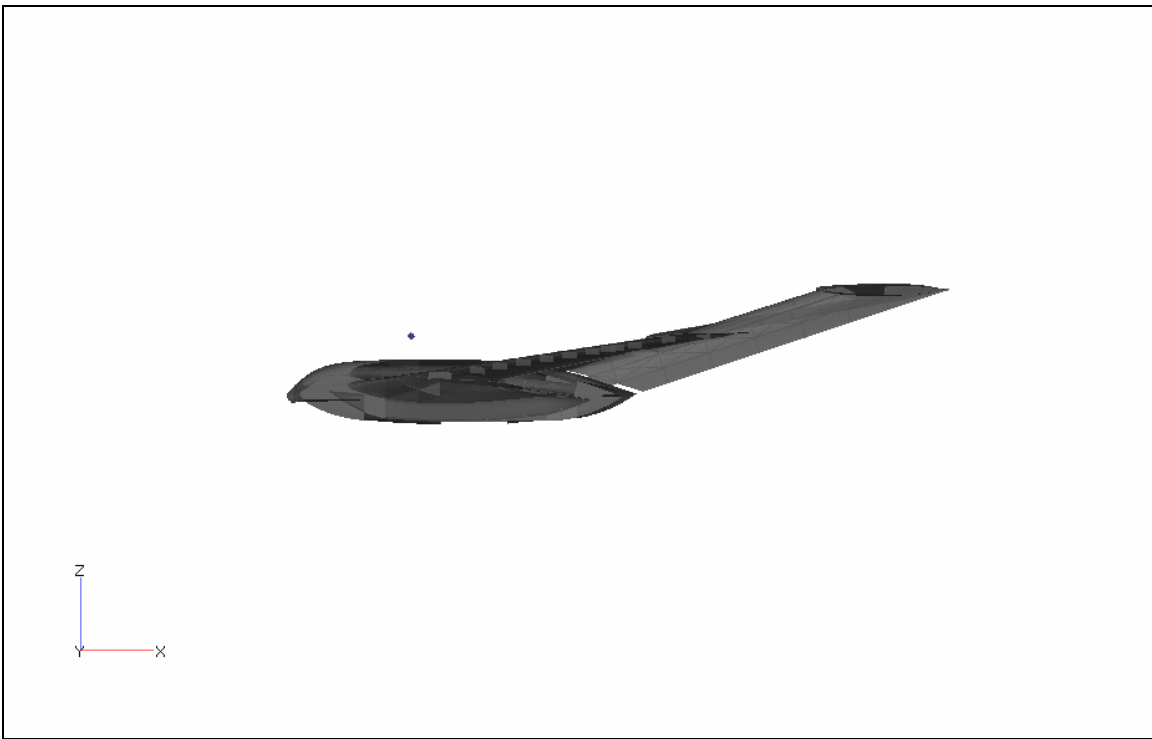


Figure 3: Profile View of Boeing SensorCraft

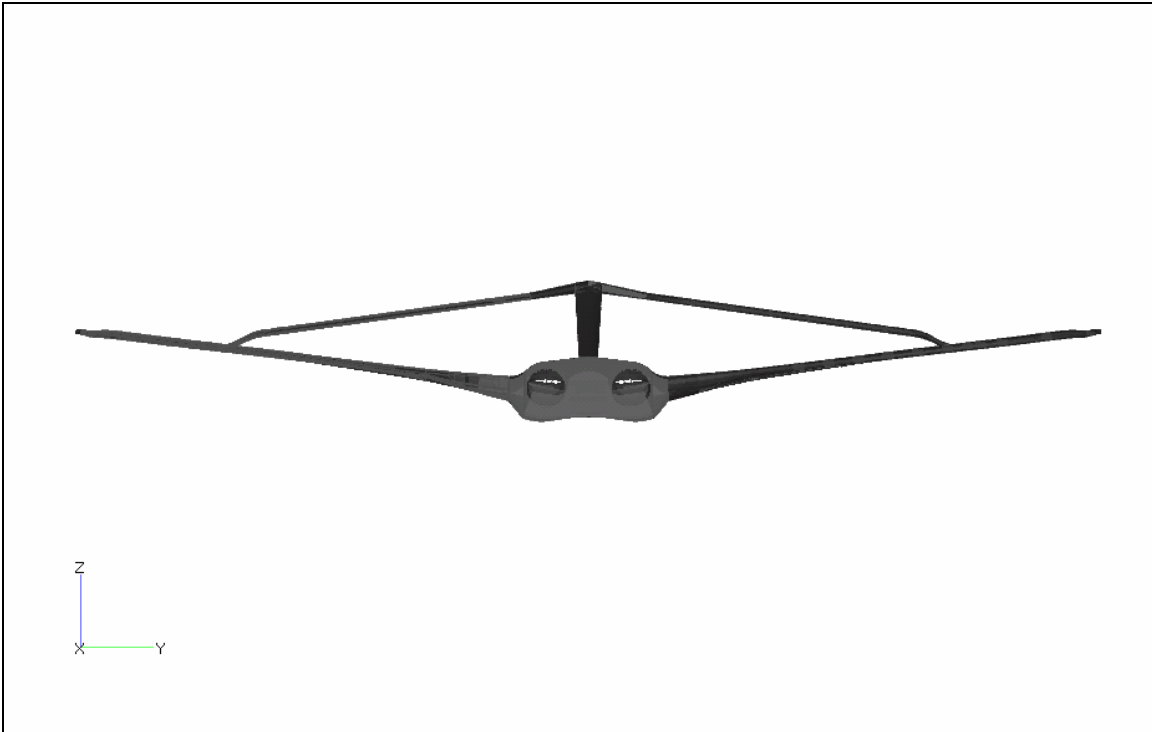


Figure 4: Front View of Boeing SensorCraft

The geometric layout of the joined wings provides three benefits unique to this design. First, to meet the requirement for 360 degree radar coverage, the radar antenna arrays are located in both the forward and aft wings as well as portions of the fuselage and tail. The large diamond planform of the wings provides for a large radar aperture. By using ultra high frequencies (UHF), along with this large aperture, the radar of the SensorCraft is able to penetrate through layers of foliage, thereby providing information on targets beneath a canopy of vegetation [11].

Second, because the aft and forward wings are connected, the need for some bending and torsion structural support material becomes superfluous. This structural weight savings is one important benefit associated with joined-wing designs when comparing it to common cantilevered designs, which rely on strong structural spars and bulkheads at the fuselage to support the weight of the entire wing. The joined-wing

design effectively enables the forward and aft wings to provide support for each other. This extra support is derived from the bending and twisting of one wing being countered by the axial resistance of the other wing and vice versa.

Third, because the aft wings are extended forward to connect with the forward wings, there is a significant increase in available fuel storage space, in the aft wings. This increased fuel capacity is advantageous to the long range and long endurance mission of the SensorCraft and is coupled with joined-wing design.

The SensorCraft also makes use of Conformal Load-Bearing Antenna Structure (CLAS). Using this multifunctional CLAS structure contributes to a significant weight savings by functioning as an antenna array and structural support. The antenna structure provides structural support by using several different materials with known strengths and mechanical properties to develop a structure that provides support for the specific loads that it will encounter, as well as provide the outer skin of the aircraft antenna locations.

The CLAS structure of the SensorCraft is laid up in a three layer sandwich configuration of Astroquartz, Honeycomb, and Graphite Epoxy (Figure 5). The Astroquartz is an electromagnetically transparent material allowing the radar to transmit and receive, as well as act as the outer shell of the skin, providing protection from the environment and external factors. Inside of this is the Honeycomb Core. This layer serves to house the radar antennas and acts to carry much of the compressive load. The core layer also serves to provide reinforcement against panel buckling. The bottom layer is the Graphite Epoxy layer which serves to bear the majority of the load incurred on the CLAS. The radar components are also mounted onto this layer [11].

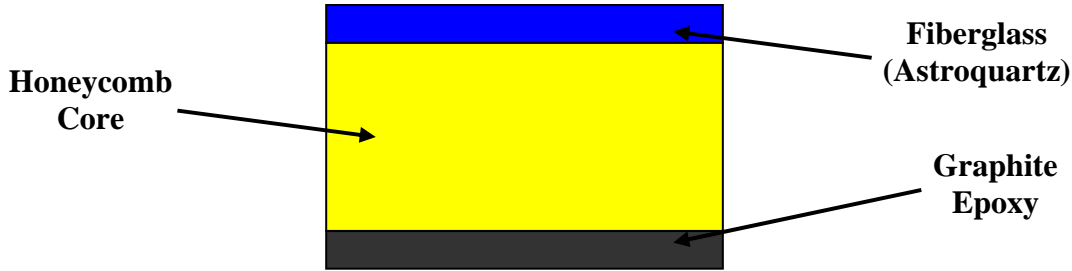


Figure 5: Conformal Load-Bearing Antenna Structure Cross-Section

Problem Statement

The joined-wing configuration presents a new set of problems unique to its design, primarily because it is a highly nonlinear system where many of the nonlinearities are interrelated. For example, the wings of the SensorCraft deflect due to the pressure force generated by the air flowing over the wings. This pressure force is normal to the surface of the wing, not necessarily opposite the weight in level flight. Additionally, because the wings do not deform linearly the direction of action of the pressure forces changes from the root to the tip of the wing. This means that as the wing deforms due to the changing pressure forces, the pressure forces themselves change due to the nonlinear change of the wing. The numerous nonlinearities of the design require the designers to incorporate several aspects at the same time, thus requiring a multidisciplinary approach to the design process for all joined-wing aircraft.

The correlation between the structural mechanics and the aerodynamics of the joined-wing is one of the principal interrelating design aspects. The importance of this relationship arises due to the aircraft's layout. Because the aft wing is mounted higher and slopes down to intercept the forward wing, lift generated by the forward wing causes it to bend upward, which places the aft wing in compression. As a result, the buckling of the aft wing becomes a significant design consideration. One key challenge with regards

to this relationship is to not only develop a structure with buckling constraints, but to determine at what load buckling will occur. Accounting for buckling constraint in the design of a joined-wing takes more time and more importantly requires extra structural support. These factors make development of a successful concept much more complicated, and in some cases not worth the tradeoff.

The current SensorCraft design features a wing span of 150 feet, and under normal flight conditions the wings will experience large bending displacements. This large wing deformation is particularly true during the later parts of the mission after much of the fuel, which is stored in the wings, has been expended. The reason for this is that the fuel mass dispersed throughout the wings provides an inertia force counter to that imposed by the aerodynamic lift forces. The implication of this large deformation is that linear finite element analysis may not be applicable, because situations concerning large displacements most often result in nonlinear deformations. This thesis will use MSC.Nastran to account for the nonlinear strain and will perform several integrated nonlinear analyses. The results from the nonlinear analyses will be compared with the linear analysis to determine how accurate the linear analysis is and where it no longer provides accurate results. MSC.Nastran is a computer finite element analysis program capable of performing linear and nonlinear structural analyses for multiple static load cases.

The large deformations of the wing also produce significant changes in the aerodynamic pressure distribution of the SensorCraft. Because the flight loads are directly related to the deflection of the wings, the process of accounting for both of these nonlinearities is an iterative one. The key aspect of the lift force is that the direction of

action will change as the wing deforms. Thus, trim lift loads generated at the beginning of an analysis are not applicable at the end. This thesis will use Zaero to develop the pre-gust level flight trim condition of the SensorCraft and various flight loads for a gust analysis. Zaero is a software system capable of using the modal solution of a finite element model to develop the aeroelastic loads for the model over a broad range of flight conditions.

Research Objective

This thesis will integrate Nastran and Zaero to account for the major nonlinearities of the system and the necessity to analyze more than a single aspect of the design at once. The focus of this research is two-fold: provide necessary analysis for the development of a scaled wind tunnel model and perform structural and aeroelastic analysis on the current Boeing Joined-Wing SensorCraft. The accomplishment of these two separate, but related tasks, will provide more information concerning the behavior of the structure, which can then be used to begin developing a more effective and efficient aircraft.

Wind Tunnel Model Development.

The purpose of the first part of this thesis is to provide the Portuguese Air Force Academy with the normal modes of the current Boeing model so that an accurate wind tunnel model could be built. As the majority of the testing done on the SensorCraft has been analytical, the experimental data of the Portuguese Air Force Academy will provide the much needed results for comparison.

Material Search.

The first step in preparing the finite element model to be given to the Portuguese Air Force Academy was to determine the material properties used for the construction of the CLAS. This was done to facilitate the clearance process and ensure that no proprietary or limited distribution information concerning the radar arrays details were being passed on. To accomplish this several reports were referenced and Finite Element Modeling And Postprocessing (FEMAP), a graphical user interface finite element analysis program, was used to confirm the location of the arrays and the materials that composed them.

Normal Modes Analysis.

The normal modes (or natural frequency) analysis computes the frequencies and mode shapes at which a structure will oscillate when excited. These natural frequencies are unique to the structure and define the dynamic motion of the structure. The importance of these natural frequencies is that when one of its corresponding modes is excited the entire structure oscillates at this natural frequency. This can result in two types of deformation from a symmetric structure: symmetric, in which the structure deforms exactly the same across its axis of symmetry, or antisymmetric, in which the structure deforms exactly opposite across the axis of symmetry. It is important to consider these natural frequencies when designing a structure as deformations that result from exciting these natural frequencies contribute to the maximum displacement. Because this normal modes analysis is to be used for the development of a wind tunnel model, it was necessary to clamp several nodes along the centerline and close to the

center of gravity, as the wind tunnel model will be mounted on a sting. This thesis uses MSC.Nastran to find the first twenty normal modes of the SensorCraft.

Structural Optimization & Aeroelastic Analysis.

The second part of this thesis was to perform a more detailed structural/aeroelastic analysis on the joined wing SensorCraft than had been done previously. This portion of the study consisted of three parts: linear static analysis, linear buckling, and non-linear static analysis. The end result of this portion of research was to compare the three results to determine the accuracy of linear analyses with the nonlinear analysis

Linear Static Analysis.

The linear static analysis makes several simplifying assumptions in order to develop solutions to complex problems. Although the SensorCraft structural analysis is neither linear nor static, the results of this analysis can be used to understand the general reaction of the model to different loading conditions. The linear static analysis takes a static fixed load and applies it to a FEM with the assumption that the stiffness of the structure will not change as it is deformed, thus resulting in a linear displacement. The purpose of the static analysis was to determine which Boeing provided load case (gust, roll, push-over, or pull-up) was the most severe and then determine which specific load set in each case resulted in the highest stressed elements. MSC.Nastran was used to solve the linear static equations for each of the four load cases. Microsoft Excel was used to process and sort the resulting stress data.

Linear Buckling Analysis.

The linear buckling analysis determines at what multiple of the applied load a structure will buckle. For a structure to be considered buckling-safe this multiple of the

reference load, or eigenvalue, λ , must at least be one, and in most cases depending on the desired factor of safety will be greater than one. In previous buckling analyses of joined-wing models two types of buckling had occurred. The first and most common was panel buckling which occurred in the skin and CLAS structures. This panel buckling consists of the panels or small sections of the aircraft's skin buckling. This is not as significant as the second type of buckling which is global buckling. Global buckling occurs when entire structural sections buckle. In the case of the SensorCraft, the aft wing is the section of concern. Global buckling is far more important in design than panel buckling as a buckled structure will result in an infinite deformation with no increase in load, this leads to a loss in structural integrity. The goal of the linear buckling analysis was to determine the location and eigenvalue of the first global buckling mode. MSC.Nastran was used to solve for the eigenvalues of the buckled SensorCraft and FEMAP was used to visually illustrate the locations of buckled panels and make appropriate corrections. The first two global buckling modes as well as multiple panel buckling modes were found.

Normal Modes Analysis.

The normal modes analysis was also necessary for the aeroelastic analysis, except that since the actual aircraft would not be supported by a sting, the normal modes were found for a free, unconstrained model. This normal modes analysis is referred to as the free-free normal modes analysis. MSC.Nastran was also used to solve the free-free normal modes analysis.

Nonlinear Static Analysis.

Nonlinear static analysis is used to improve upon the approximation of the linear static analysis by accounting for some of the nonlinearities of the system. Though the

results would be more accurate if the design were to account for all of the nonlinearities accompanied with a system, it would be an exceedingly prolonged process and more often than not the effect of many of these nonlinearities is inconsequential to the final result. Two nonlinearities to be considered are the geometric or strain nonlinearities and the follower-force nonlinearities. The geometric nonlinearities are associated with the SensorCraft structure, through the wing deformations which occur during normal flight conditions. The follower force nonlinearities come into effect through the aerodynamic load produced by the wings. Because the wings generate a pressure distribution with a force normal to the surface of the wings the direction of action of this force will change as the wings deform. To account for these follower force effects, Zaero is used to develop the aerodynamic forces at several stages in the flight envelope, MSC.Nastran to apply the loads and computes the nonlinear structural deformation, and Matlab to update the deformed aerodynamic panel model for Zaero. This process was then repeated several times using loads at incremental time points throughout the gust. Through this iterative process the follower force effects were accounted for, Boeing had not accounted for any follower force effects.

II. Literature Review

Introduction

This chapter summarizes the work that has been done concerning joined-wing aircraft, with particular focus on matters concerning structural integrity and aeroelastic effects. First, details concerning the joined-wing concept as a whole are discussed, focusing on its development and the advantages that this unique design has to offer.

Second, it examines the work that has been done with regard to the Boeing SensorCraft, concentrating on the studies that have focused on the relationship between aerodynamics and structural mechanics. Of particular interest in this area were the studies that attempted to determine the divergence of the nonlinear static solution from the linear static analysis and their relation to the buckling limit, as this is a critical design analysis for the joined-wing design.

Joined-Wing Review

The joined wing concept was first demonstrated successfully by Platz's glider in 1922 and Brown's airplane in 1932; however, it was not until Wolkovitch received his patent in March of 1976 that the concept began to be taken seriously. Ten years later Wolkovitch published "The Joined Wing: An Overview," which detailed several advantages of the joined wing concept over a conventional aircraft and gave supporting evidence derived from wind tunnel testing and finite element analysis. In his report, Wolkovitch described several advantages of the joined-wing concept over a conventional

winged aircraft, namely: less induced drag, reduced subsonic and supersonic drag, built-in direct lift and sideforce control capability, and good stability and control. Of these advantages, the most directly related to structural integrity of the joined wing airframe were the decrease in structural weight and the higher stiffness for the wing structures.

Wolkovitch [3] found that the joined wing with the optimal joint location typically weighs 65 to 78 percent of what an equivalent cantilevered wing weighs. The optimal joint location for the lightest configuration was an aft wing connection at 70 percent of the front wing's span.

Wolkovich observed that the lifting force of the forward and aft wings can be resolved into two separate components, normal and parallel to the joined-wing structure (

Figure 6). The component normal to the plane containing the forward and aft wing structure creates a bending moment about the vertical axis. This creates a canted bending axis which requires the structural lay-up of the joined wing to be different than that of a cantilevered wing. The most important consequence is a thinner wing box and thus a thinner airfoil.

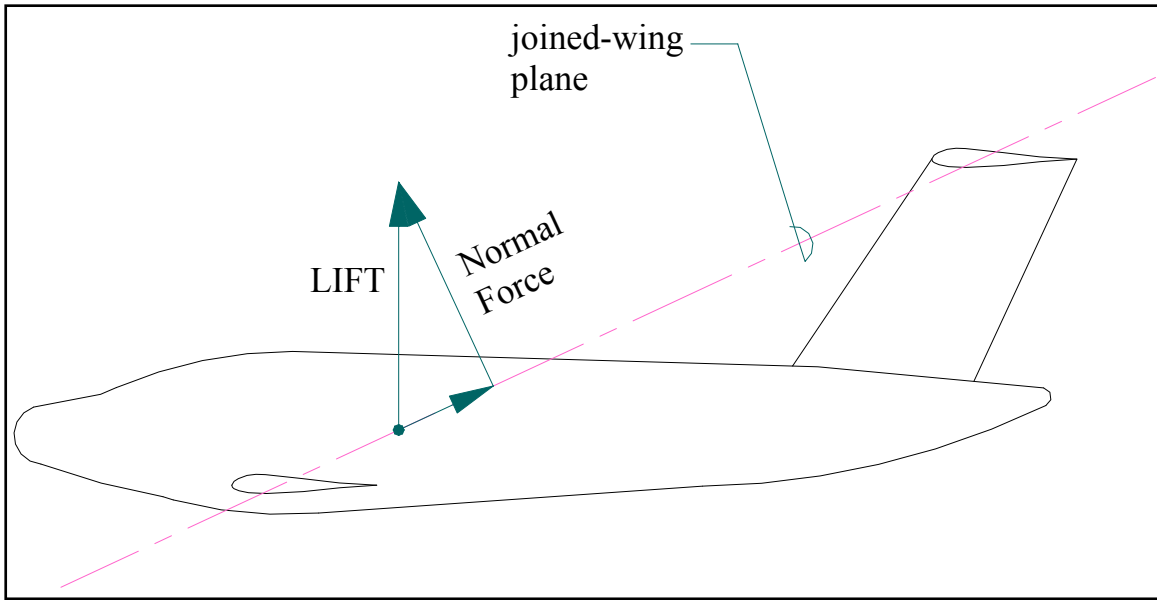


Figure 6: Canted Normal Force in Joined-Wing Plane [11]

To resist the bending moment, it is necessary to place the material as far from the neutral axis as is possible. This is because the stress is highest furthest from the neutral axis. The added benefit of doing this creates a much larger wing box which increases the storage capacity for fuel for the same thickness-to-chord ratio or a smaller thickness to chord ratio (Figure 7).

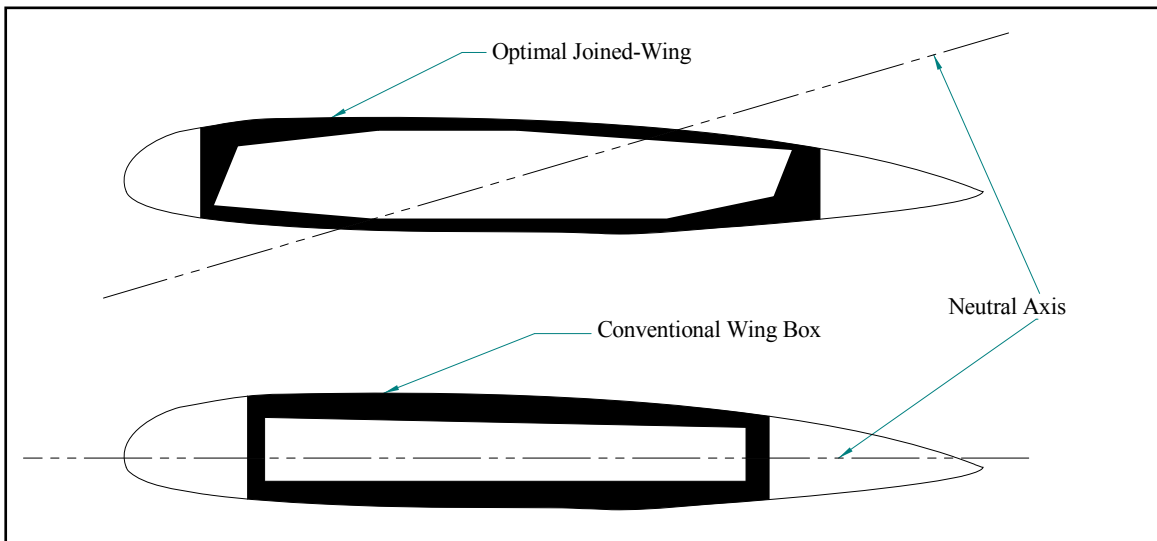


Figure 7: Optimal Joined-Wing Structure Vs. Cantilever Wing Structure [3]

Wolkovitch showed that, depending on joint location, the joined wing could carry between 16% and 54% more fuel than a conventional wing. This added fuel storage comes from the addition of the aft wings and from the increase in size of the wing box structure of the joined-wing. It should also be noted that the increase in box structure size decreases the available area for flaps and other control surfaces.

The joined wing concept also helps reduce the necessary structural support in both the wing and the fuselage. By joining the wings the torsion and bending stiffness of one wing is increased by the axial resistance of the other and vice versa. Also, because both wings exert an upward lifting force, the fuselage bending moment will be decreased considerably, as compared to a conventional cantilevered wing design where the tail exerts a downward lifting force to counter the pitching moment created by the upward lifting force from the wing.

Gallman and Kroo [5] compared the in-plane bending moment of a conventional and joined-wing aircraft (Figure 8). They made notable discoveries concerning the joined-wing plane (Figure 6) bending moment, M_x , of the joined wing configuration, finding a considerable decrease in magnitude at the root, two sign changes (negative, positive) through the transition from the root to the joint location, and a discontinuity in the loads at the joint location. This thesis will consider these findings when modifying the SensorCraft panels in order to analyze the buckling modes of the joined wing.

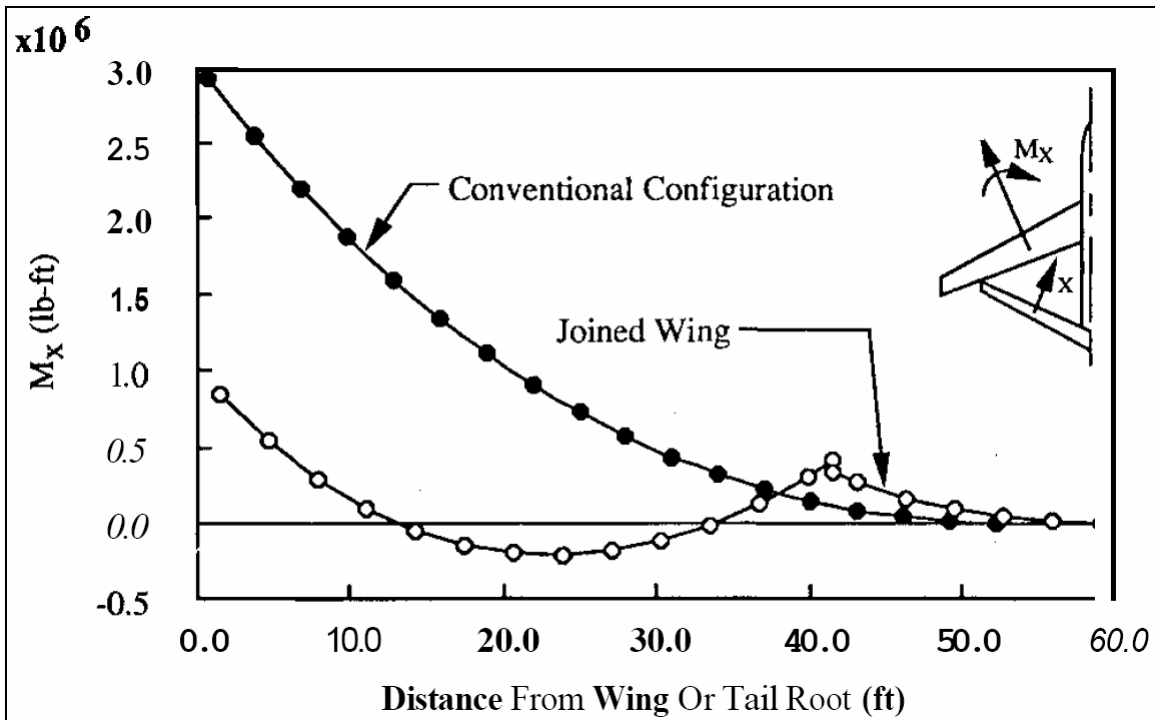


Figure 8: In Plane Bending Comparison of Conventional and Joined-Wing Structures [5]

Gallman and Kroo [5] used numerical optimization to develop a single-point design of a joined-wing transport aircraft and compared the direct operating cost (DOC) to a similar conventional aircraft. After including buckling constraints in their analysis, they found that the structural weight increased by approximately 13% in a fully stressed design that was 0.9% heavier than the minimal weight design. This increase in weight led to a 5% higher DOC when compared to a conventional transport when buckling was included. They also found that the computation time required to apply the buckling constraint was significant. In the end, they concluded that, though the buckling constraint required an increase in design time and DOC, “A different set of mission specifications and design assumptions may produce joined wings that perform significantly better.” This thesis will seek to determine when the applied load is buckling critical, as the

joined-wing planform is more suitably arranged for sensor arrays embedded in wing skins requiring 360° radar coverage. Furthermore, the increased capacity for fuel is advantageous to the extended range and loiter requirements of SensorCraft mission profile.

Livne [7] evaluated past work and attempted to develop a method for future studies and optimization of joined-wing configurations. He determined that the joined-wing configuration created complex interactions between aerodynamics and structural mechanics. Livne concluded that a multidisciplinary design approach must be utilized in order to design a concept that would meet both requirements simultaneously. This study will utilize this approach by combining nonlinear aeroelastic analysis with structural analysis.

Lee and Chen [8] performed nonlinear aeroelastic studies focusing on stability and buckling of nonlinear joined-wing systems. Their studies were performed using several different gust and trim conditions. To accomplish this, the nonlinear system was divided into several linear subsystems with nonlinear parameters. Lee and Chen concluded that a buckled structure does not necessarily become unstable, but its post-buckling stability depends on initial trim condition and gust velocity. Figure 9 shows a comparison of the results for a buckled aft wing at varying trim and gust conditions. This thesis will compare the linear buckling case with a nonlinear static analysis derived from initial trim conditions and aeroelastic gust analysis.

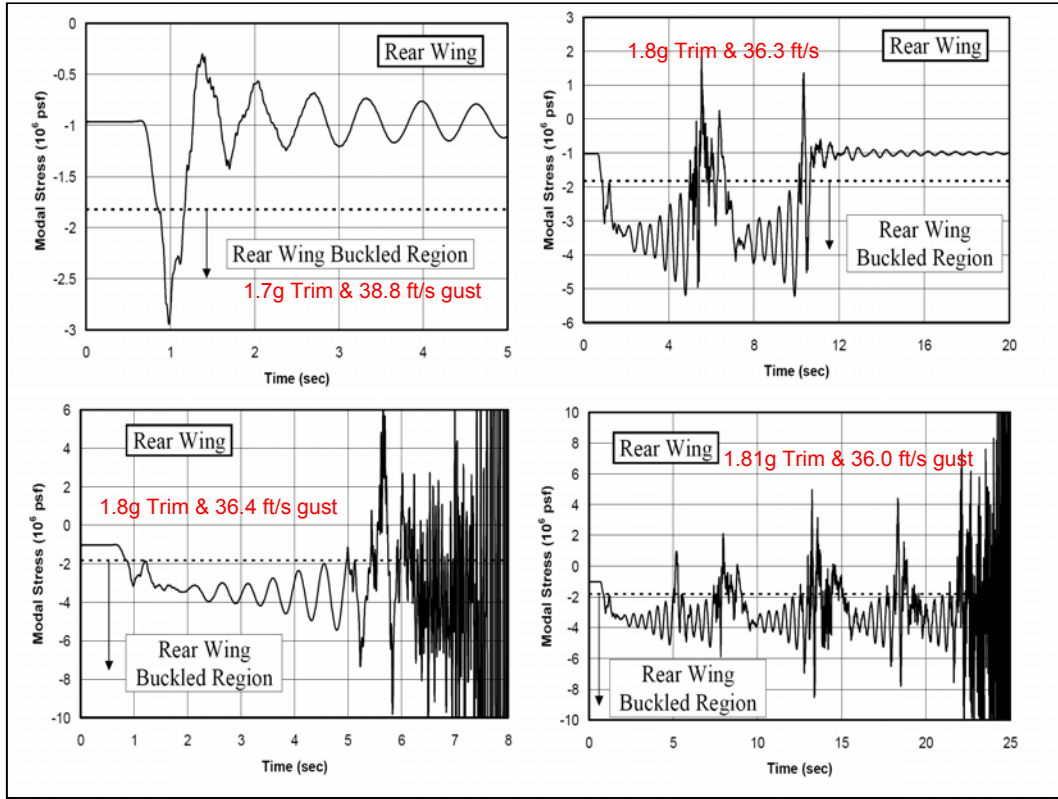


Figure 9: Stability of Buckled Structure Depending on Flight Conditions [8]

Nees and Canfield [7] conducted research in fracture mechanics from fatigue failure due to opening, the most significant mode for fatigue in shell structures. The purpose of the study was to reduce unexpected fatigue problems and decrease the overall weight of the structure by implementing weight savings in less critical panels. Nees and Canfield concluded that the most important factors in panel fatigue stress were material fatigue properties, stiffened panels design, panel thickness, and location. It was also found that the panels' design impacts panel buckling, stress distribution, and surface cracks. This thesis modifies the panel design to improve the structural integrity of the joined-wing concept.

SensorCraft Review

Blair and Canfield [4] began developing an integrated design method for joined-wing configurations to improve the multidisciplinary design process necessary in joined-wing design. Through the use of Adaptive Modeling Language (AML), MSC.Nastran and PanAir, an integrated geometric model and user interface was developed called Air Vehicles Technology Integration Environment (AVTIE). They concluded that non-linear analysis was essential in order to gain accurate information concerning large deformation. This study will attempt to advance the integration process between the aerodynamics and structural mechanics of the Boeing joined wing concept and provide detailed information with regards to the divergence of the linear and nonlinear analysis results of the SensorCraft.

Roberts [11] developed two SensorCraft models, one of aluminum and one utilizing the CLAS lay-up consisting of graphite epoxy material. His study validated that the joined-wing concept is highly multi-disciplinary and the design process is intensely iterative, and that the gust load case is the most critical design load case. Roberts also concluded that a buckling analysis is insufficient in predicting the onset of nonlinear effects in joined-wing configurations for vehicles sized according to linear stress analysis alone. This was because non-linear deformations were shown to be much larger than the deformations from the linear analysis. This study will compare the linear and nonlinear static analyses for of the Boeing configuration, cases incorporating rigid and flexible aerodynamic loads for the gust load case validated as the most severe.

Rasmussen [12] developed weight-optimized configurations for the SensorCraft based on the 360° radar coverage requirement. He then performed buckling and non-

linear analysis on the two optimized configurations, one with a low vertical offset and another that followed typical joined-wing design in which, if viewed from the front or top, the wings formed a diamond, with a high vertical offset. He concluded that to resist buckling a lower thickness-to-cord (t/c) ratio can be used in designs with a high vertical offset, and for designs with low vertical offset a higher t/c ratio must be used. He also found the critical failure is significantly dependent on the vertical offset: lower offset lends itself towards panel buckling, while higher offset tends towards global buckling. This should be expected as wings with a lower vertical offset will not be subjected to compression due to the deflection of the other wing. This study will develop a more refined nonlinear gust analysis for the current SensorCraft configuration which has a high vertical offset.

Viisoreanu [13] performed linear and non-linear static analysis on the Boeing joined-wing FEM. The preliminary results showed that the non-linear analysis only converged up to 92.2% of the ultimate strength. He summarized that if the solution approached global instability that, the slope of the deformation should increase rapidly. However, because both the vertical deflection and wing twist exhibit a decreasing slope, Viisoreanu stated that global buckling was not an issue. He cited the alternative for the lack of convergence as local panel buckling. Vissoreanu also showed that the non-linear deformation is approximately one-third the magnitude of the linear deformation without accounting for the follower force effects. Figure 10 shows a comparison of deflected wing shape and magnitude for linear and non-linear analysis, where **Dz**, indicates deflection in the vertical direction, and **Twist**, refers to twist of the wings. This thesis

will attempt to correct the panel buckling and obtain results for the non-linear analysis closer to the global buckling load factor.

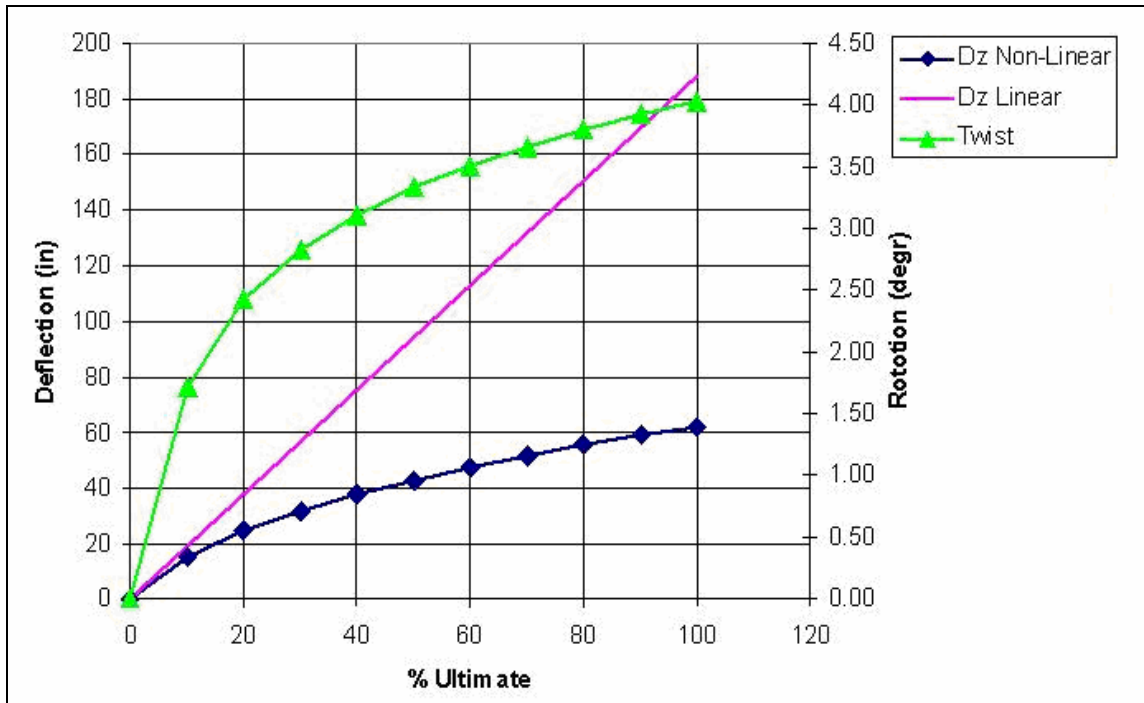


Figure 10: Comparison between linear and non-linear wing-tip deflection [13]

The Aerodynamic Efficiency Improvement (AEI) [14] study done by Boeing provided a exhaustive description of the current state of the SensorCraft with particular regards to its aerodynamics and structural mechanics. The information presented by the AEI study that is pertinent to this study is presented in the following section.

Structural Lay-up of wings.

The forward wing structure consists of three main spars (front, mid, aft), one secondary spar (closeout spar), ribs and skins. The antennas are embedded in the skins between the front and mid spars and on the forward surface of the front spar. The area surrounding the antennas is filled with honeycomb core to increase buckling resistance. To allow the radar to operate effectively the leading edge is constructed from fiberglass.

The forward wing includes three control surfaces (aileron, outboard flap, inboard flap). The control surfaces operate in an aileron style fashion by rotating relative to a hinge line. The forward control surfaces consist of a spar, ribs, and skins, and the area between the upper and lower skins surface is filled with honeycomb core.

The aft wing structure houses two spars, ribs and skins. The antennas are embedded in the skins between the spars and on the back surface of the aft spar. The area surrounding the antennas is filled with honeycomb core to increase buckling resistance.

The aft wing also consist of three control surfaces, however these surfaces do not operate in the same fashion as the forward wing. The aft wing upper and lower control surfaces are of clam shell type in that surfaces are independently actuated. The outboard flaps move counter to each other while the middle and inboard flaps move in the same direction. Figure 5 presents a cross-sectional view of the forward and aft wings with the layout of the sensors and a depiction of the actuation of the control surfaces. This information is particularly relevant with regards to the panel buckling of the model and the normal modes analysis.

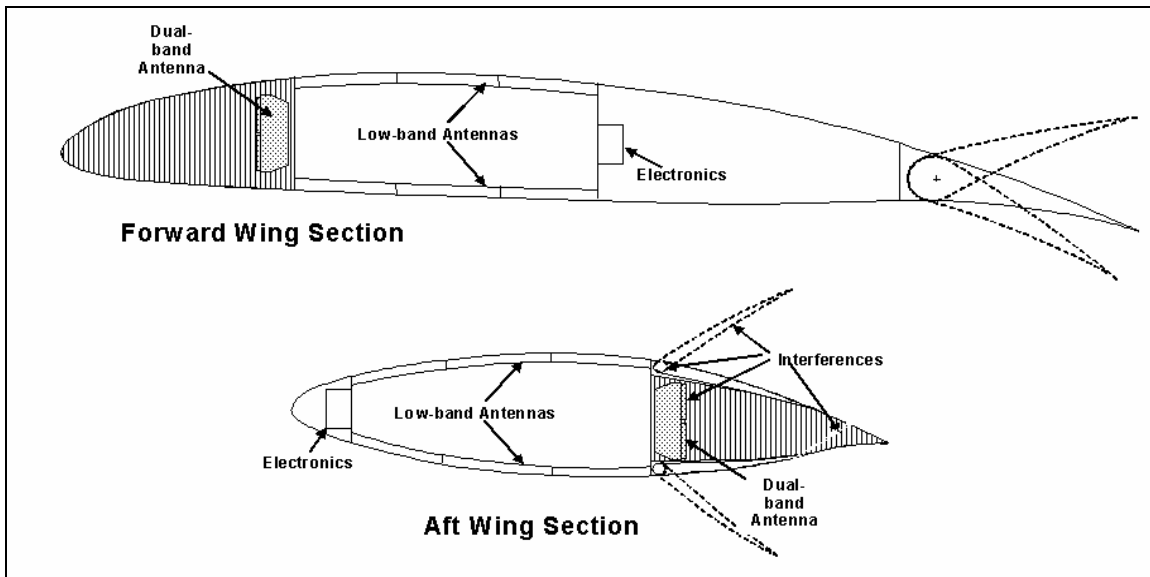


Figure 11: Wing Cross-section and Sensor Layout [14]

Normal Modes Analysis.

Boeing performed a normal modes analysis on the SensorCraft to determine the effect of fuel loading on the modal frequencies. They determined that the mode shapes and order were not significantly altered, but that the frequency at which the mode appears did increase as fuel loads decreased. Boeing also found that the aft control surfaces, because they were clam shell type, exhibited bending modes at low frequencies. This study will confirm and expound upon these results to provide more information concerning the modes of the SensorCraft after the model has been updated to prevent panel buckling.

Aeroelastic Structural Analysis.

The AEI study performed by Boeing conducted aeroelastic stability analysis for three internal fuel levels (10%, 60%, 100%) and four flight conditions for each fuel level; Mach=0.255 at sea level, Mach=0.5 at 32,874 feet, Mach=0.70 at 46,921 feet, and

Mach=0.85 at 55,000 feet. They also identified the two critical flutter mechanisms as symmetric aft wing 1st bending & forward wing 2nd bending, and antisymmetric aft wing 2nd bending & forward wing torsion. Boeing found that both critical flutter conditions had the smallest margin of safety for the 100% fuel case, Mach=0.85 at 55,000 feet. Boeing also confirmed that the gust load case was the most critical of all load cases.

Roll, Push-Over, Pull-Up.

Boeing then developed a monitoring scheme in order to rank the loads to determine the most critical load cases. Using certain CQUAD elements to monitor membrane forces and a few CROD elements to monitor axial forces, the loads were ranked based on the number of maximum and minimum stress occurrences. For the push-over, roll, and pull-up load cases the internal fuel level of 100% was most significantly linked to cases exhibiting higher stresses. The flight conditions coupled with the higher stresses were Mach=0.85 at 55,000 feet and Mach=0.255 at sea level. This study will confirm these results and then analyze the most severe case determine the structural stability with regards to linear static, buckling, and non-linear static analyses.

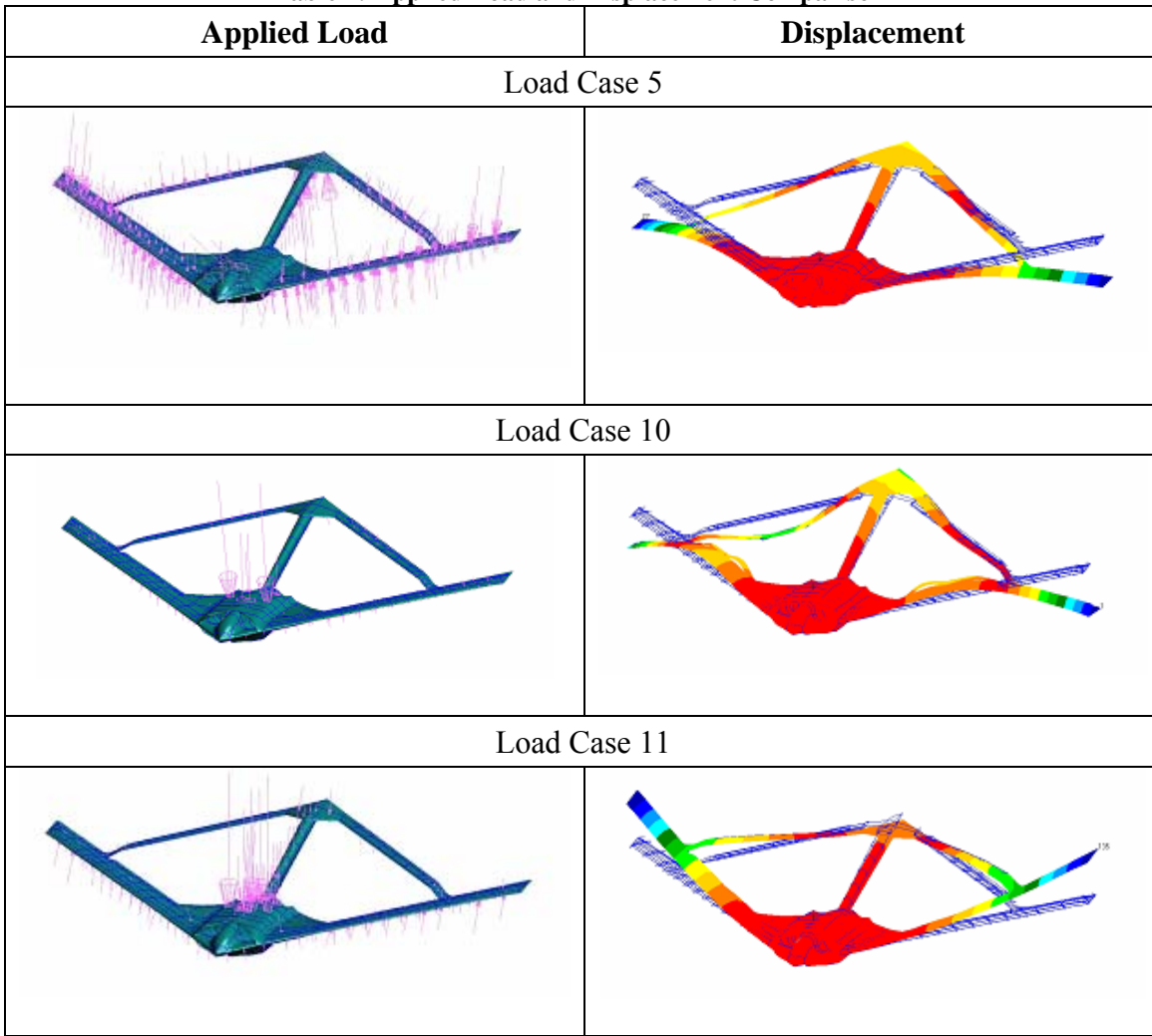
Gust.

Boeing performed a similar study for the gust analysis, monitoring rod elements to evaluate the bending moment and quad elements to evaluate the torsion moment. They determined that the critical gust frequencies 0.8, 2.0, and 2.7 Hz would be used for their analysis. Boeing found for a transient gust analysis that as soon as the gust impacts the forward apex of the aircraft, the effect becomes noticeable approximately 0.21 seconds later and that the effect fades out after four seconds. For the transient gust analysis the

low Mach, low altitude flight condition was found to be critical in all cases and the critical fuel levels were found to be 100% with an upward gust and 10% for a downward gust, whereas 60% was never found to be critical. Three critical load cases were analyzed and the deflection and stress contour was plotted. A comparison of the cases is tabulated in the Table 1 and Table 2. All cases were for a Mach number of 0.255, sea level altitude, and a gust intensity of 62.0 feet/second (negative for cases 5 and 10 and positive for 11).

Table 1: Comparison of Load Cases

Name	Gust Case 5	Gust Case 10	Gust Case 11
Fuel Level	10%	100%	100%
Gust Freq. (Hz)	1.3	8.1	0.8
Time (sec)	1.025	0.674	1.188
Force (Gust & Trim)	-137.0 lbs	2634.5 lbs	21911.0 lbs
Maximum Displacement	-77.7 in	-15.4 in	135 in

Table 2: Applied Load and Displacement Comparison

Basis for Current Research

This thesis will expand upon the research performed by Boeing and will seek to provide more accurate results. To provide more accurate results several aspects in the analysis process will be either included or accounted for differently.

First, Boeing accounted for the trim condition of the aircraft simply by adding the static trim loads to the dynamic response of the gust load. This thesis will separate the gust analysis into incremental load cases and will perform a nonlinear static analysis, which includes the static trim condition as the first case.

Second, Boeing developed the “inertia relief” from the fuel loads by applying equivalent static loads to the airframe. To ensure that the fuel mass loads were equivalent to the applied static load the sum of the applied load was compared to a static analysis. In Boeing’s study, the 100% fuel case produced the largest strains and deformations in all flight conditions, when compared with lesser fuel levels. This seems counterintuitive since the mass of the fuel should help to balance the upward lift forces in certain maneuvers. In order to validate this result, this study will analyze the transient response of the model to several gust cases.

III. Methodology

Radar Material Search

The locations of the radar arrays and their material properties were found by using FEMAP and several references. A starting point for obtaining the location of the arrays and the properties used to construct the arrays was acquired from referencing 7.0_Model_Sim_Anal.ppt [16] for the radar locations, Figure 12, and the composite lay-up of the CLAS from referencing previous theses [11, 12, 15].

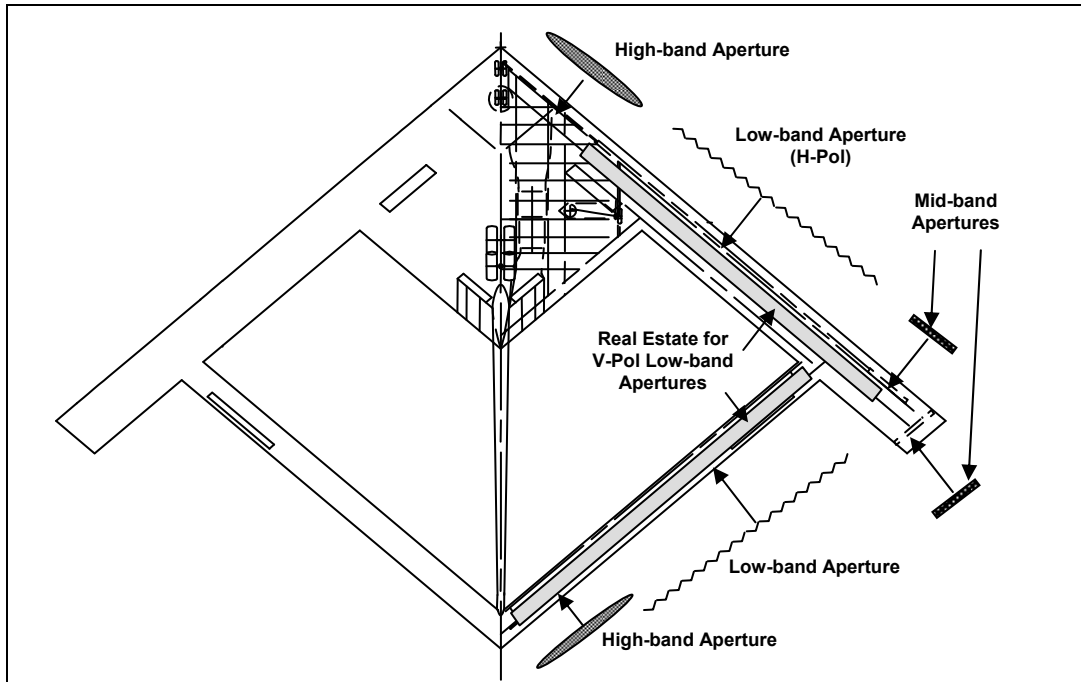


Figure 12: Radar Arrays Locations [17]

With this information, FEMAP was used to locate all the materials used in the wings and form them into groups. The materials were then compared to the references based on location of use and material properties.

Normal Modes Analysis

To accomplish the clamped normal modes analysis for the wind tunnel model, node 48056 which is connected by rigid elements along the centerline of the SensorCraft and is near the center of gravity (Figure 13) was constrained. Table 3 lists the location of the center of gravity and node 48056 relative to the origin. All six degrees of freedom for this node were constrained using a single point constraint (SPC). This was necessary because the wind tunnel model would be mounted on a sting during testing and would not behave the same as a free aircraft or model. After a preliminary run, it was found that for the clamped normal modes analysis the model exhibited large aft wing control surface oscillations. The modes that resulted from this vibration were irrelevant, as the actual aircraft would have sufficient actuator stiffness in order to prevent this. To correct the modes associated with the control surface flutter, the trailing edges of the control surfaces along the aft wings were connected. This is not accurate of the actual clam shell control surface design of the SensorCraft, but is an acceptable means to suppress those modes for scaling and flutter analysis. With a single point constraint and the trailing edges of the aft control surfaces connected the first twenty normal modes for the clamped analysis were found.

Table 3: Location of Center of Gravity and Constrained/Supported Nodes

	X (in)	Y (in)	Z (in)
Center of Gravity	219.02	0	-65.56
Support/Constrained Node 48056	168.125	0	-119.94

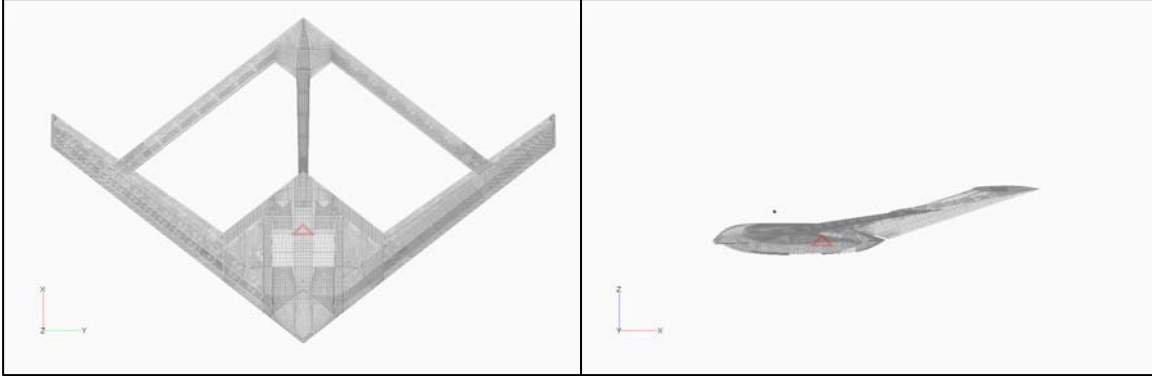


Figure 13: Location of Clamped/Supported Node for Normal Modes Analyses

The normal modes analysis for the nonlinear procedure required several alternate steps in order to obtain the required results. First, the output from MSC.Nastran was modified using a set of “Alter Statements”. These statements generated the modal mass matrix for the normal modes analysis which is the product of the mass matrix and the modal displacement matrix in the global degrees-of-freedom coordinate system. The purpose of this file is to enable Zaero to generate the aerodynamic forces for the rigid body modes which occur at zero frequency. The inertial forces due to rigid body accelerations can be related to the accelerations of the rigid body motions by the rigid body modes such as [19]:

$$\{F_I\} = [\bar{M}][D]\{\ddot{u}_r\} \quad (1)$$

Where \bar{M} is the structural mass matrix, D are the rigid body modes, and \ddot{u}_r are the accelerations of the rigid body motion. These accelerations are also referred to as the “trim degrees-of-freedom” [19].

Second, because the results for this normal modes analysis are only used by Zaero when generating the flight loads, only the displacements of the grid points that make up the aerodynamic spline are needed, not the entire model. This is because only the grid

points along the spline are referenced by Zaero when updating the aerodynamic panel model.

Third, because Zaero references the normal modes analysis to determine flight dynamics and stability of the model it is necessary to find a substantial number of normal modes, forty-five were found for this thesis. Furthermore, it was discovered during early runs that including all forty-five modes resulted in the model behaving asymmetrically, that is that the displacements due to the gust were not the same for each wing. To correct this only the symmetric modes were used, which ensured that the model did not exhibit any asymmetric motion during the Zaero runs. It is important to note that the normal modes include the rigid body modes as well. The symmetric rigid body modes that should be kept are the pitch and plunge modes. Removing the forward-aft translation mode is also necessary, as it generates no aerodynamic forces and its inclusion otherwise skews the results. These rigid body modes are recalculated by Zaero and have no reference to the Nastran solution. Furthermore Zaero finds pure rigid body mode, that is each rigid body mode exhibits only translation along a single coordinate axis or rotation about a single coordinate axis. Considering this the plunge and pitch modes from Zaero correspond to modes 3 and 5 respectively. For this thesis the plunge mode was not used and as such the results are more representative of a wind tunnel analysis. Additionally, because the model was not allowed to translate in the z direction the results are more conservative. Removing the non-symmetric modes reduced the number of normal modes used for the analysis from forty-five to twenty-one. This emphasizes the need for incorporating a significant number of normal modes in the analysis.

Fourth, it was necessary for the first six rigid-body modes to occur at zero frequency, not approximately zero. To accomplish this, a support card referencing the same node as the clamped analysis, 48056, with all six degrees of freedom was used. This is not the same as using a single point constraint, as these completely constrain the prescribed degrees of freedom, thereby clamping the model and altering the natural frequencies. Using such a support informs MSC.Nastran that the first six normal modes will occur at zero frequency, which bypasses the need for MSC.Nastran to determine the rigid body modes from the stiffness matrix singularities. In addition to forcing rigid body modes to occur at zero frequency using a support also ensures that the modes exhibit only translation or rotation. This is important because for an unconstrained model the rigid body modes can be any combination of translations and rotations.

MSC.Nastran Normal Modes Analysis.

The two separate normal modes analyses were performed using the solution method 103 in MSC.Nastran. The motion of structural dynamic systems is described by a set of equations that expresses the balance between external applied loads, the internal forces and the inertial forces [1]

$$[M]\{\ddot{u}\} + [B]\{\dot{u}\} + [K]\{u\} = \{P(t)\} \quad (2)$$

where $[M]$ is the mass matrix, $[B]$ is the damping matrix, and $[K]$ is the stiffness matrix. For normal modes analysis, Equation 2 is simplified, because the solutions of interest are those associated with an undamped ($[B] = 0$) and unforced ($\{P\} = 0$) system.

$$[M]\{\ddot{u}\} + [K]\{u\} = 0 \quad (3)$$

Assuming separation of variables and harmonic motion yields the following:

$$\{u((x, y, z), t)\} = \{\phi(x, y, z)\} e^{i\omega_n t} \quad (4)$$

Making this substitution into Equation 2 gives:

$$[K]\{\phi\} - \omega_n^2 [M]\{\phi\} = 0 \quad (5)$$

Equation 5 can be rewritten as an eigenvalue problem:

$$(\{K\} - \lambda[M])\{\phi\} = 0 \quad (6)$$

where:

$$\lambda = \omega_n^2 \quad (7)$$

In order for the eigenvalue problem to have nontrivial solutions, the determinant of the coefficient matrix must equal zero.

$$\det(\{K\} - \lambda[M]) = 0 \quad (8)$$

Each one of the roots, λ_i ($i=1,2,\dots,n$), then satisfies the eigenvalue problem such that the result is:

$$(\{K\} - \lambda_i[M])\{\phi_i\} = 0 \quad (9)$$

For Equation 9, each mode $\{\phi_i\}$ is a vector of displacement amplitudes that corresponds to the eigenvalue, λ_i .

Linear Static Analysis

The purpose of the linear static analysis served two functions. The first was to determine which load case (gust, roll, push-over, or pull-up) was the most severe and which specific load set in each case resulted in the highest stressed elements. Linear static analysis was done to determine which load set, of the gust, roll, push-over and pull-up load cases should be used for the nonlinear analysis. The second purpose was to analyze the most severe load set and determine the shape and magnitude of the maximum

deflection. This was done for the buckling analysis in order to determine which cases were the most prone to buckling.

Table 4 and Table 5 describe the load cases and their corresponding load sets that were provided by Boeing. In these tables, **Fuel** describes the percentage of maximum fuel on board, **Mach** describes the Mach number at which the maneuver takes place, **Push-Over**, **Pull-Up** and **Roll** describe the maneuver and **Gust** describes the flight condition.

Table 4: Push-Over, Pull-Up, & Roll Load Set Descriptions

Fuel	Mach	Push-Over (-1g)	Pull-Up (2g)	ROLL (Point)		
				1	2	8
10%	0.255	1111	1121			1138
	0.50	1211	1221			
	0.70	1311	1321			
	0.85	1411	1421			
60%	0.255		2121			2138
	0.50		2221			
	0.70		2321			
	0.85		2421			
100%	0.255	3111	3121		3132	3138
	0.50	3211	3221			
	0.70	3311	3321			
	0.85	3411	3421	3431	3432	3438
110%	0.255		4121			
	0.85		4421			
1st Digit	2nd Digit	3rd Digit				

Table 5: Gust Load Set Description

Fuel	Mach	Freq.	GUST (Time)			
			1	2	3	4
10%	0.255	1	11411	11412	11413	
		2	11421	11422	11423	
		3	11431	11432		
		4	11441	11442		
100%	0.255	1	31411	31412	31413	31414
		2	31421	31422	31423	31424
1st Digit	2nd Digit	4th Digit	5th Digit			

After running all the load cases, the maximum stress in key element types was stored and imported into Microsoft Excel. For plate, laminate and solid elements the VonMises stress was used to compare the maximum stresses because it accounts for both positive and negative stress. Equation (10) is the VonMises stress equation. For the rod elements, the axial stress was used to compare the different load cases. Equation (11) is the axial stress equation.

$$\frac{1}{\sqrt{2}} \sqrt{\sigma_x^2 + \sigma_y^2 + 6 \cdot (\tau_{xy}^2)} = \sigma_e \quad (10)$$

$$\sigma = \frac{P}{A} \quad (11)$$

The load sets were then ranked based on the magnitude and frequency of the maximum stress that occurred within a specified sample, which was referred to as a hit. The number of elements examined (sample size) varied for each load case and was dependant on the number of load sets involved (sample space), more load sets led to a large sample size. This was done so that even load sets which exhibited few hits could be compared against each other. For the situation where the number of hits was the same for multiple sets, a refined sample size was used. This provided more detail as to which of the tied load sets experienced higher stress magnitudes than the other.

The linear static analyses were performed using the solution method 101 in MSC.Nastran. The displacements for a linear static analysis are described by a set of equations that consist of the stiffness of the structure, $[K]$, the displacements, $\{u_l\}$, and the applied forces, $\{P_l\}$.

$$[K]\{u_l\} = \{P_l\} \quad (12)$$

These set of equations are solved by first decomposing the stiffness matrix into its upper and lower triangular factors. A forward-backward substitution is then performed for all load cases that have the same constraints [1].

Linear Buckling Analysis

The goal of the linear buckling analysis was to be able to determine where and at what magnitude the first global buckling mode would appear. The first step in the process was to determine the most severe of these twelve remaining load sets (three most severe load sets from each load case) with regards to buckling. This was accomplished by running linear buckling analyses on the remaining load sets. It was found that the first buckling modes appeared in the gust load case far sooner than in roll, pull-up, and push-over. Considering these results, the roll, pull-up and push-over load cases were disregarded because the onset of buckling occurs much later than in the gust cases.

The most severe gust load set was found by comparing the three buckling analyses. After this comparison gust set 31411, which corresponds to a Mach of 0.255, sea level altitude, 100% fuel and a gust frequency of 0.8 Hz was deemed the most severe for two reasons. First, it exhibited panel buckling far earlier than the other gust load set, and second the linear deformation of gust case 31411 was geometrically identical to the other two critical gust cases (symmetric forward wing 1st bending), but greater in magnitude. Because the deformations were geometrically the same the stress contours for each gust load should follow the same pattern.

To find the first global buckling mode it was necessary to correct the model in order to eliminate some of the early panel buckling. This was also necessary for the nonlinear static analysis, as the results would not converge if panel buckling was present.

The process employed to accomplish this task was an iterative process of running a buckling analysis, adjusting the core thickness of the buckled panels, re-running the analysis with the corrected panels and fixing the next set of buckled panels. The panel correction process was repeated until the load scale factor, λ_i , exceeded 2.5. In general, a safety factor of 1.5 is used, that is to say that the structure will not fail until 150% of the original load has been applied. Because the model did not experience global buckling until much later than expected, the model's panel buckling was corrected until 250% of the original load resulted in the first buckling mode, panel buckling.

The panels were modified by increasing the thickness of the core section of the composite sandwich panels (Figure 5). Table 6 shows the properties that buckled as well as their initial and final thickness, where 'PCOMP' stands for property composite. It should be noted that, only half of the model was created and then mirrored to obtain the complete model. Considering this several property names were not reflected however in all cases, the actual mechanical properties were reflected. This is the reason for three property changes where it would seem that either two or four would be necessary. The property names are those listed in the MSC.Nastran bulk data file.

Table 6: Adjusted Composite Properties to Prevent Panel Buckling

Section	Property	Original	Final
Tail	PCOMP 16	0.5	2.0
	PCOMP 45	0.5	2.0
	PCOMP 58	0.5	2.0
Yehudi	PCOMP 177	1.0	2.0
	PCOMP 174	1.0	2.0
Wing	PCOMP 122	0.5	1.0
	PCOMP 117	0.5	1.0
	PCOMP 31	0.5	1.0
Connection	PCOMP 22	0.5	1.0
	PCOMP 95	0.5	1.0
	PCOMP 98	0.5	1.0

MSC.Nastran Buckling Analysis.

The linear buckling analyses were performed using the Nastran solution method 105. In MSC.Nastran, adding the differential stiffness (K_d) to the linear stiffness matrix (K_l) leads to an eigenvalue problem that is solved for linear buckling [24]. The differential stiffness matrix is based on the first, higher-order terms in the strain/displacement relationship [11]. By adding the linear and differential stiffness matrices, the stiffness for the model becomes:

$$[K] = [K_l] + [K_d] \quad (13)$$

In equilibrium, the total potential must be stationary.

$$\frac{\partial[U]}{\partial u_i} = [K_l]\{u\} + [K_d]\{u\} = 0 \quad (14)$$

This can be rewritten as:

$$([K_l] + P_a[\bar{K}_d])\{u\} = 0 \quad (15)$$

where P_a is the magnitude of applied load. Non-trivial values of P_a can be solved for by:

$$[K_l] + P_{\text{critical}}[\bar{K}_d] = 0 \quad (16)$$

The non-trivial values of P_a are the critical buckling loads, P_{critical} [11]. “The number of buckling loads obtainable...is equal to the number of degrees of freedom in the model” [24]. This implies,

$$\lambda_i \bullet P_a = P_{\text{critical},i} \quad (17)$$

Incorporating this into equation (15) yields:

$$[K_l] + \lambda_i [\bar{K}_d] = 0 \quad (18)$$

Equation 18 is an eigenvalue problem where the solutions of λ_i are scale factors of the applied load that results in a buckling condition, either panel or global. The smallest value of λ_i must be greater than one for a structure to not buckle under the applied load P_a .

MSC.Nastran uses the Lanczos method to extract eigenvalues for buckling analysis. The Lanczos method is similar to the inverse power method, but uses each vector in the sequence, equation (19) to determine the most accurate approximation to the eigenvalue.

$$\{r\}, [A_0]^{-1}[M]\{r\}, ([A_0]^{-1}[M])^2\{r\}, \dots, ([A_0]^{-1}[M])^n\{r\} \quad (19)$$

Where

$$[A_0] = ([K] - \lambda_0[M]) \quad (20)$$

and $[M]$ is the mass matrix and $\{r\}$ is a starting vector.

Nonlinear Static Analysis

The nonlinear analysis portion of this thesis utilized several different programs in order to capture two of the key nonlinearities associated with the SensorCraft. To accomplish the nonlinear analysis, Matlab code developed specifically for this thesis by Garmann and Alyanak of AFRL/VA was used to refine the aerodynamic panel model of the SensorCraft, Figure 14. Zaero was used to develop the aerodynamic loads accounting for follower force effects, and MSC.Nastran was used to apply the flight loads and perform nonlinear structural analysis.

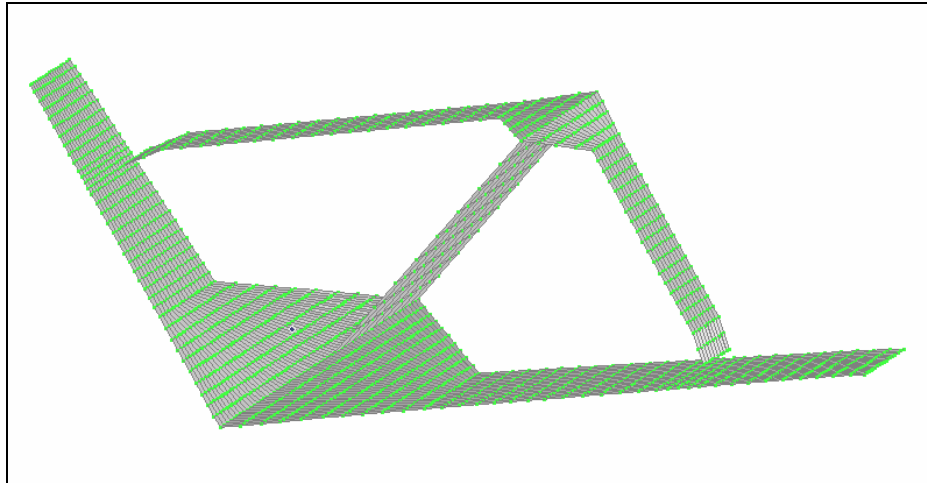


Figure 14: Aerodynamic Panel Model

Analysis Setup.

Matlab.

To generate the updated aerodynamic panel model, four functions needed to be called from Matlab referencing either the MSC.Nastran input or output file, GETGRID, CAERONODES, AERO, and GETDISP. Via a sequential execution of these four functions and a step where the original grid points are added to the displacements the updated panel models are generated.

GETGRID scans the MSC.Nastran input file for all grid data. It then exports the details of the grid points into a n by four matrix where n is the number of grid points in the model. The first column of the matrix is the grid point identification number used in the model, and the second, third and fourth column are the x, y and z position of the grid points relative to the global coordinate system.

CAERONODES takes the grid point matrix from GETGRID and generates the baseline aero model based on the prescribed panel characteristics. It is only necessary to run this function one time as the panel characteristics remain constant throughout the analysis.

To characterize the panels, the user inputs parameters defining the number of panels, the number of spanwise and cordwise divisions, and the spacing for each panel inside of the CAERONODES M-file. CAERNODES then scans the grid points of the model and uses these preexisting grid points to develop the panels. When defining the panels it is important to be conscious of key geometric features such as the aft and forward wing connection regions and breaks in control surfaces. By defining panels, that overlap or mask these characteristics, errors can result due to non-existent grid points. More importantly, the panels will not accurately describe the aerodynamic surfaces of the aircraft.

AERO takes the constant panel characteristics generated by CAERONODES and the grid point details from GETGRID and writes the Zaero include files. The include files needed by Zaero are the refined panel definitions (CAERO7.dat), the spline information (SPLINE.dat) and control surface definitions and coordinate systems

(CONTROL_SURFACES.dat). These are the three include files that must be altered after each iteration in order to account for the follower-force effect.

GETDISP scans the MSC.Nastran output file from the previous iteration for all displacement data. GETDISP then exports the details of the grid points into a n by four matrix. The first column of the matrix is the grid point identification number used in the model the second, third and fourth column are the displacements of x, y and z respectively relative to the previous location. Because all of the previous results are stored in the MSC.Nastran output file for a restarted analysis, it is not necessary to keep track of the displacements from the previous runs.

Rerunning AERO will use the original unchanging panel parameters and generate the new displaced panel definitions for Zaero. The Matlab code outputs the inputs for Zaero to the Zaero folder inside the Matlab functions file. It should be noted that rerunning AERO overwrites the previous CAERO7.dat, SPLINE.dat, and CONTROL_SURFACES.dat files.

Zaero Trim.

Two separate analyses were done in Zaero in order to capture the dynamics of the aerodynamic forces with regards to the SensorCraft. The first was the trim analysis for a Mach 0.255 flight at sea level, and the second was a 62.0 feet/second vertical gust at the trimmed condition. For both analyses it was necessary to include the modal information generated by the MSC.Nastran normal modes analysis.

To setup the trim analysis, several details concerning the geometric properties of the SensorCraft as well as the flight conditions needed to be described. The details used

by this thesis for setting up the Mach 0.255 sea-level trim analysis are described in Table 7.

Table 7: Trimmed Flight Analysis Inputs

TRIM ANALYSIS		
<i>SensorCraft</i>		
Parameter	Units	Value
Mach		0.255
X _{cg}	In	219.203
Y _{cg}	In	0.0
Z _{cg}	In	-65.564
I _{xx}	in ⁴	1.259E10
I _{xy}	in ⁴	1.070E7
I _{yy}	in ⁴	7.683E9
I _{xz}	in ⁴	1.460E9
I _{yz}	in ⁴	7.047E5
I _{zz}	in ⁴	1.950E10
Weight	Lbm	1.456E5
Ref _{cord}	In	142.53
Ref _{span}	In	1798.00
Ref _{area}	in ²	246187.00
<i>Environment</i>		
Altitude	In	0.0
Density	sln/in ³	1.1456E-7
Dynamic Pressure	sln/(in*sec ²)	0.67

Zaero Gust.

The gust analysis used for this thesis was a discrete gust, which is used to analyze an aircraft encountering a specific type of gust profile. For a discrete gust the time-domain generalized aerodynamic gust forces are obtained by the inverse Fourier transform, i.e. no rational aerodynamic approximations are involved [19]. The discrete gust analysis provides the transient responses of the aircraft to the gust.

The Fourier transform used to calculate the aerodynamic gust forces is:

$$P(t) = \frac{1}{\pi} \int_0^{F_{MAX}} \text{Re} \left[Q_{hG}(ik) e^{ikx_0} T(i\omega) e^{i\omega x} \right] d\omega \quad (21)$$

Where $P(t)$ is the generalized aerodynamic gust forces in the time domain, $Q_{hG}(ik)$ is the generalized aerodynamic gust force in the frequency domain, x_0 is the gust reference point, and $T(i\omega)$ is the Fourier transform corresponding to the gust type. In addition to the geometric and environmental details, described in the trim analysis the gust analysis required details concerning the dynamic response of the SensorCraft, the flight conditions prior to the gust, and the conditions of the gust. Table 8 describes the additional inputs for the 62.0 feet/second gust analysis. Examples of the Zaero inputs for the trim and gust analysis are included in Appendix B.

Table 8: Transient Gust Analysis Inputs

GUST ANALYSIS		
<i>SensorCraft</i>		
Parameter	Units	Value
Omitted Normal Modes	Sequential MSC.Nastran Output	1, 2, 3, 4, 8, 9, 12, 14, 15, 16, 18, 21, 24, 26, 27, 29, 31, 33, 35, 37, 38, 39, 41, 43
Support Node	Grid #	48056
Four States	α, θ, Q, H	0.05, 0.0, 0.0, 0.0
$\text{Alpha}_{\text{Trim}}$	Degrees	2.78
<i>Gust</i>		
Type		1-Cosine
$\text{Alpha}_{\text{gust}}$	Degrees	90.00
$\frac{\text{Velocity}_G}{\text{Velocity}_{SC}}$		0.2178
Gust Length	Sec	2.50
T_{start}	Sec	-1.25
T_{end}	Sec	7.00
Reduced Frequencies		0.025, 0.05, 0.1, 1.25

The normal modes of the model have a tremendous effect on a transient analysis and are referenced by several cards in the Zaero code. To ensure that the normal modes of the model do not predict unrealistic behavior several steps were taken. First, as

described previously, all the antisymmetric modes were removed and the first six rigid body modes were supported to ensure that they occurred at zero frequency.

Second, the time history of the rigid body modes was computed via integrating their respective velocity time histories. This was done because they occurred at zero frequency, and helps to provide more accurate displacement time histories of the modes. This was accomplished by setting DXTOX=YES in the MLDSTAT card. Third, it was necessary to define four airframe states, provided that only the pitch and plunge rigid body modes are left. These four states (angle-of-attack, α , Euler pitch angle, θ , pitch rate, Q , and altitude, H) are perturbations from the rigid body modes. For this analysis all states were defined as zero because no change from the trim and condition was desired. Lastly, the mode acceleration method or Summation of Forces (SOF) was used instead of the mode displacement method, because it generally provides more accurate results than the mode displacement method [19]. The mode displacement method calculates forces at grid points by:

$$\{F\} = [K]\{x\} \quad (22)$$

The mode acceleration method calculates the forces by summing all forces from the equation of motion:

$$\{F\} = -[M]\{\ddot{x}\} + F_a(t) + F_e(t) \quad (23)$$

Where $[M]$ is the mass matrix, F_a is the aerodynamic forces, and F_e is the external applied forces, in the case of this analysis. This was done by specifying SOF=YES in the MLDPRNT card.

The angle of attack used for the gust analysis was obtained from the Zaero trim analysis output file. The trim analysis was run twice to ensure that follower force effects had been accounted for.

The gust profile file chosen for this thesis was the one minus cosine (1-cosine) gust profile because this profile was best suited for a nonlinear quasi-steady gust response. This gust profiled represents steady level flight, followed by an increase in gust velocity to the peak and then a regress back to zero gust velocity. The 1-cosine profile is described by equation (24).

$$T(\tau) = \begin{cases} 0 & \text{for } \tau < 0 \\ \frac{1}{2} \left(1 - \cos \left(\frac{2\pi\tau}{L_G} \right) \right) & \text{for } 0 \leq \tau \leq L_G \\ 0 & \text{for } \tau > L_G \end{cases} \quad (24)$$

The angle of attack for the gust case of interest to this thesis was of an upward rising gust from directly below the SensorCraft. To account for this, the gust angle of attack was chosen to be 90°.

The gust velocity was chosen due to the results of the linear static analyses provided by Boeing. The desire was to choose a flight condition where the aerodynamic forces imparted to the wings played a key role. Considering that the gust velocity of 62.0 feet/second produced the largest deflections, this seemed to be the ideal choice. The velocity of the gust was defined in Zaero by taking the ratio of gust velocity to forward velocity, 284.86 feet/second in this case.

The gust frequency of 0.8 Hz was chosen because it was close to the first flexible natural frequency of the SensorCraft found from the MSC.Nastran normal modes

analysis. This was also confirmed by Boeing to be one of critical frequencies of the SensorCraft. The length of the gust in seconds was then found by taking the inverse of this frequency, Equation (25).

$$L_G = \frac{1}{f} \quad (25)$$

Figure 15 shows the four gust profiles used for this thesis and their lengths relative to the SensorCraft, (scale representation). The goal was to find a gust length which would not interact with the SensorCraft too quickly, resulting in the majority of the deflection being from inertia rather than aerodynamic forces, and not too gradually thereby providing no substantial increase in aerodynamic forces. Neither of these would allow the follower force effect to be considered. A gust length of 2.50 seconds was chosen because 1.25 seconds did not exhibit a maximum response until after the gust had ended (indicating prominent inertial forces), and by 5.00 seconds the SensorCraft was experiencing only a minimal increase in deflection.

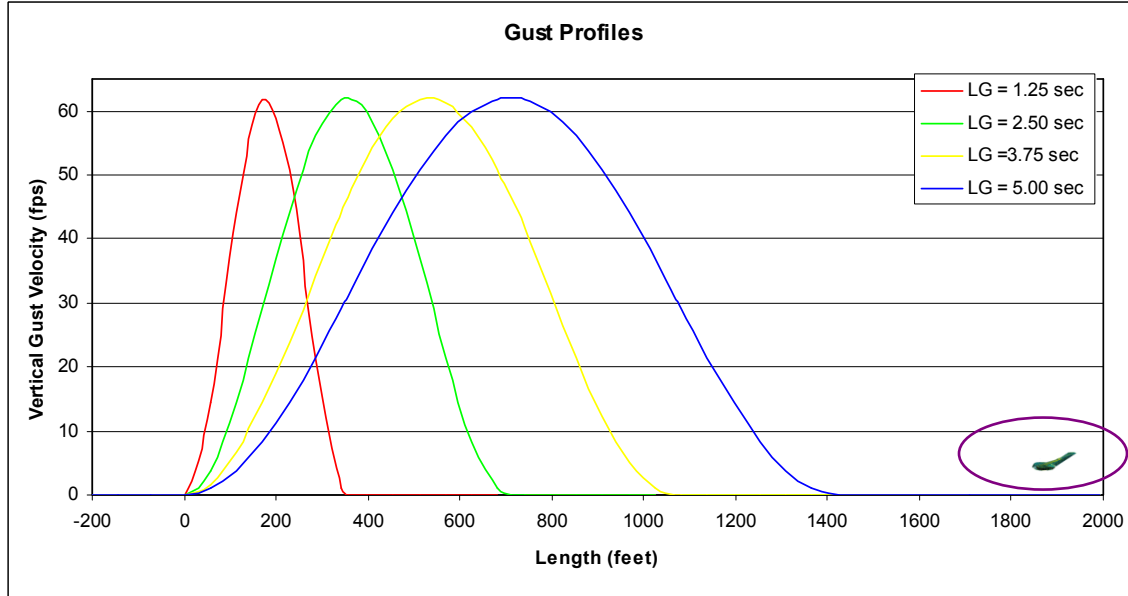


Figure 15: Gust Length Profiles Comparison

Setting the start time to a negative time provided a period of dead time for the SensorCraft prior to encountering the gust. This was done to ensure that the model was properly defined and not experiencing any forcing functions other than the gust. This was accomplished by reviewing the outputs for the displacement and acceleration of specific grid points which should be constant for this time period if the analysis was properly defined. Negative 1.25 seconds was chosen as the starting time because this would extend the total time of the analysis, which was important for the computation of the inverse Fourier transform used for calculating gust forces, and placed the SensorCraft a sufficient distance aft of the gust to ensure that it encountered the full gust and that any instability would be clearly visible.

The accuracy of the unsteady aerodynamics of the model is highly dependent on the reduced frequencies, k . Considering this, and considering that the development of this matrix requires a substantial amount of computational time, careful attention was paid to ensure that the proper reduced frequencies were chosen. First, equation (26) was used to calculate k for all four gust lengths. Table 9 lists these calculated gust frequencies for the corresponding gust length using the reference cord, $REFC$ and velocity, V from

Table 6.

$$k = \left(\frac{\pi \cdot REFC}{LG \cdot V} \right) \quad (26)$$

Table 9: Calculated Reduced Frequencies

Gust Length (sec)	1.25	2.50	3.75	5.00
Reduced Frequency (Hz)	0.1048	0.0524	0.0349	0.026

Several additional considerations were also taken into account as stipulated by the Zaero Users Manual [19]. First, from the profile of the 1-cosine gust, (equation 24) it can be seen that there exist peaks at $\omega=2\pi/LG$. This implies that $Q_{hG}(ik)$ must have an accurate frequency content as given by equation (27). Second, the smallest reduced frequency should be greater than 0.02 to avoid numerical truncation errors, which can lead to an inaccurate imaginary part of the unsteady aerodynamics [19]. Third, to handle the aerodynamic lag roots and rigid body modes several reduced frequencies were chosen between 0.02 and 0.05. Last, to avoid numerical calculation problems within Zaero the range of frequencies was not too broad and the highest reduced frequency was greater than:

$$k_{\max} > \frac{2\pi(\omega)(c/2)}{V} \quad (27)$$

Where ω is the frequency of the gust, c , is the reference cord and V , is the SensorCraft velocity.

Table 10: Reduced Frequencies

Reduced Frequencies Used For Gust Analysis			
0.025	0.05	0.1	1.25

MSC.Nastran Nonlinear Analysis.

The nonlinear static analysis was performed by MSC.Nastran using the nonlinear static analysis solution procedure, SOL 106, the Newton-Raphson and modified Newton's methods for the nonlinear iteration technique.

MSC.Nastran solves a nonlinear problem by dividing the total applied load into smaller increments. Each increment is solved through an updated stiffness matrix and

updated element coordinates. This thesis accounted for the follower force effects by dividing up the total gust load into subcases, which were the Zaero results.

MSC.Nastran employs an approximate updated Lagrangian approach for geometric nonlinear problems. This method computes the linear strains in the updated element coordinate system in order to eliminate the effects of the rigid body rotation, but equilibrium is established at the final positions in the stationary coordinate system [25]. This means that the finite element mesh is updated after each load increment and is a valid method for problems featuring large inelastic strain.

In MSC.Nastran the equilibrium equation for nodal forces is:

$$\{F\}^e = \int_V [\bar{B}]^T \{\sigma\} dV \quad (28)$$

These nodal forces are equivalent to the elements boundary stresses and balance the applied load $\{P\}^e$. Differentiating the equation for the nodal forces yields:

$$dF = \int_V \bar{B}^T (d\sigma) dV + \int_V (d\bar{B}^T) \sigma dV \quad (29)$$

This reduces to:

$$dF = [K_L + K_R + K_\sigma] du \quad (30)$$

Where:

$$\begin{aligned} K_L &= \int_V B_L^T D B_L dV \\ K_\sigma &= \int_V d B_N^T \sigma dV \\ K_R &= \int_V [B_L^T D B_N + B_N^T D B_N + B_N^T D B_L] dV \end{aligned} \quad (31 \text{ a,b,c })$$

This differentiation yields the linear stiffness matrix, K_L , the geometric stiffness matrix, K_σ , and the stiffness due to large rotations, K_R . The significance of these stiffness matrices is that, for nonlinear analyses, updating them is one of the most time consuming processes. As such, MSC.Nastran has several methods which can be used enhance the step.

Newton's method of iteration is able to define the unbalanced forces at any iteration step as an error vector because the error vanishes at constraint points and the constraint forces vanish at free points [20]. The error vector is

$$\{R_a\} = \{P_a\} - \{F_a\} \quad (32)$$

The linear system of equations is then solved by decomposition and forward backward substitution for incremental displacements. The tangential stiffness matrix then results from determining the Jacobian of the error vector. The stiffness matrix equation to solve at the i -th iteration is:

$$[K_T] \{\Delta u^i\} = \{R^{i-1}\} \quad (33)$$

Where

$$[K_T] = - \left[\frac{\partial R}{\partial u} \right]_{u=u^i} = \left[\frac{\partial F}{\partial u} \right]_{u=u^i}$$

$$\{\Delta u^i\} = \{u^i\} - \{u^{i-1}\} \quad (34 \text{ a,b,c})$$

$$\{R^{i-1}\} = \{P\} - \{F(u^i)\}$$

The iteration process continues until the residual error $\{R\}$ and the incremental displacements $\{\Delta u\}$ become negligible, which is signified by the convergence criteria

[25]. The residual error is then carried into the next iteration to recalculate internal forces. The Newton-Raphson method converges when,

$$\|u^* - u^{i+1}\| \leq q \|u^* - u^i\|^2 \quad (35)$$

Where q is a for convergence criteria and u^* is the true displacement. An equilibrium state is achieved when the true displacement converges with the applied load. Once the increment is converged, the stiffness matrix is then updated.

The iteration process of the Newton-Raphson method is depicted by Figure 16. The stiffness matrix of the structure is represented by the slope of the dashed red line and is updated after each iteration in accordance with the Newton-Raphson method. Though the stiffness matrix update takes a significant amount of time the solution will converge in the fewest number of iterations.

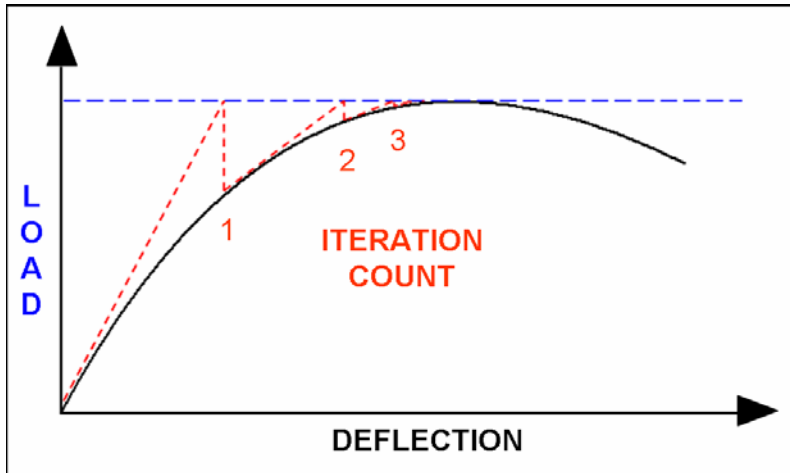


Figure 16: Newton-Raphson Method

The Modified Newton method uses the stiffness matrix developed at the initial position for the entire nonlinear analysis. Figure 17 is an example of the iteration process employed by the Modified Newton method. Though time is saved because the stiffness matrix is not updated the number of required iterations is increased.

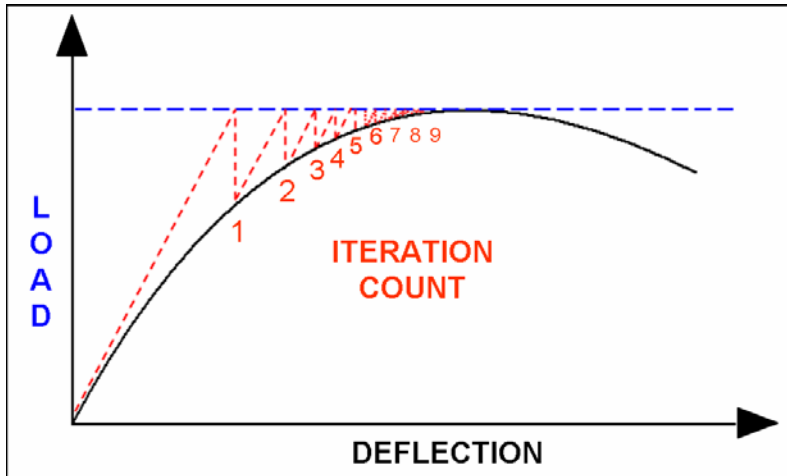


Figure 17: Modified Newton Method

Not updating the stiffness matrix can lead to the solution failing to converge (Figure 18). This could occur if the stiffness of the material or the structure increased significantly as the load increased, thus the original slope would result in the predicted displacement to be less than the actual displacement for an applied load. The problem results when the program attempts to converge the solution without updating the stiffness matrix, because the initial calculated stiffness is significantly less than the actual stiffness.

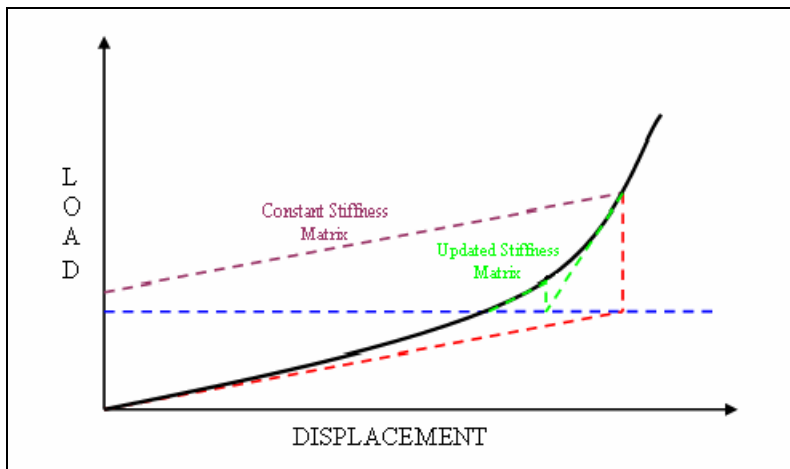


Figure 18: Non-Convergence Example

This thesis tested both methods and because the deformations were not overly large the modified Newton's method was six times faster than the Newton-Raphson method.

The restart process was an essential process for the nonlinear analysis portion of this thesis. To reduce the time required for the MSC.Nastran portion of the analysis and because the previous results did not need to be recalculated each time, the bulk data file was set up to allow the analysis to be restarted from the previous converged solution. Following the completion of this primary run, the remaining iterations were simple repetitions of the preceding analysis procedure. To enable the analysis to be restarted SCRATCH=NO was entered into the command window. This is necessary because MSC.Nastran is set up for multiple users and in order to prevent excess file buildup the default setting is to delete the MASTER and DBALL files once the analysis has completed. The MASTER and DBALL files are necessary for a restart and by using the assign command specific names were given to these files; this was done to prevent MSC.Nastran from overwriting previously written files.

To restart a converged solution a new bulk data file was created that defined the solution method via the executive and case control sections of the bulk data file and assigned the MASTER file from the previous analysis. It was also necessary to obtain from the converged solution's output file the last 'Loop Id' and 'Sub Id' number. These were used to inform MSC.Nastran where it would be restarting from 'Loop Id,' and where it was going next, 'Sub Id.' For this thesis, because the load increment was the only new set of information, it was all that was included. It should also be noted that a copy of the restart file should be made prior to attempting a restart, because if an error

should occur the altered MASTER and DBALL files can no longer be used for the restart.

Examples of the original input and restart files for the gust analysis are included in

Appendix B.

Procedure.

The multidisciplinary nonlinear analysis procedure is depicted by Figure 19.

The independent inputs are located on the left except for the “Displacements” which is the output of the last iteration. The blue-grey boxes are the programs used to perform each step of the analysis. The outputs and dependant inputs are located on the right. The orange boxes are inputs that remain unchanged and are independent of iteration. The light blue boxes are the outputs of the respective program and are to be used as the inputs for the next program. Because these outputs are dependent on the previous iteration, they were modified for each iteration. The yellow box represents the time history of the wingtips and two central grid points’ accelerations and displacements. This was used as a check to ensure that the both wings encountered the gust symmetrically, that the reactions to the magnitude and direction of the loads made sense, and that the SensorCraft was stable prior to encountering the gust. The acceleration details were also used to determine at what point in time the SensorCraft was subjected to the most significant amount of force. Finally the bright green box signifies the completion of a given iteration.

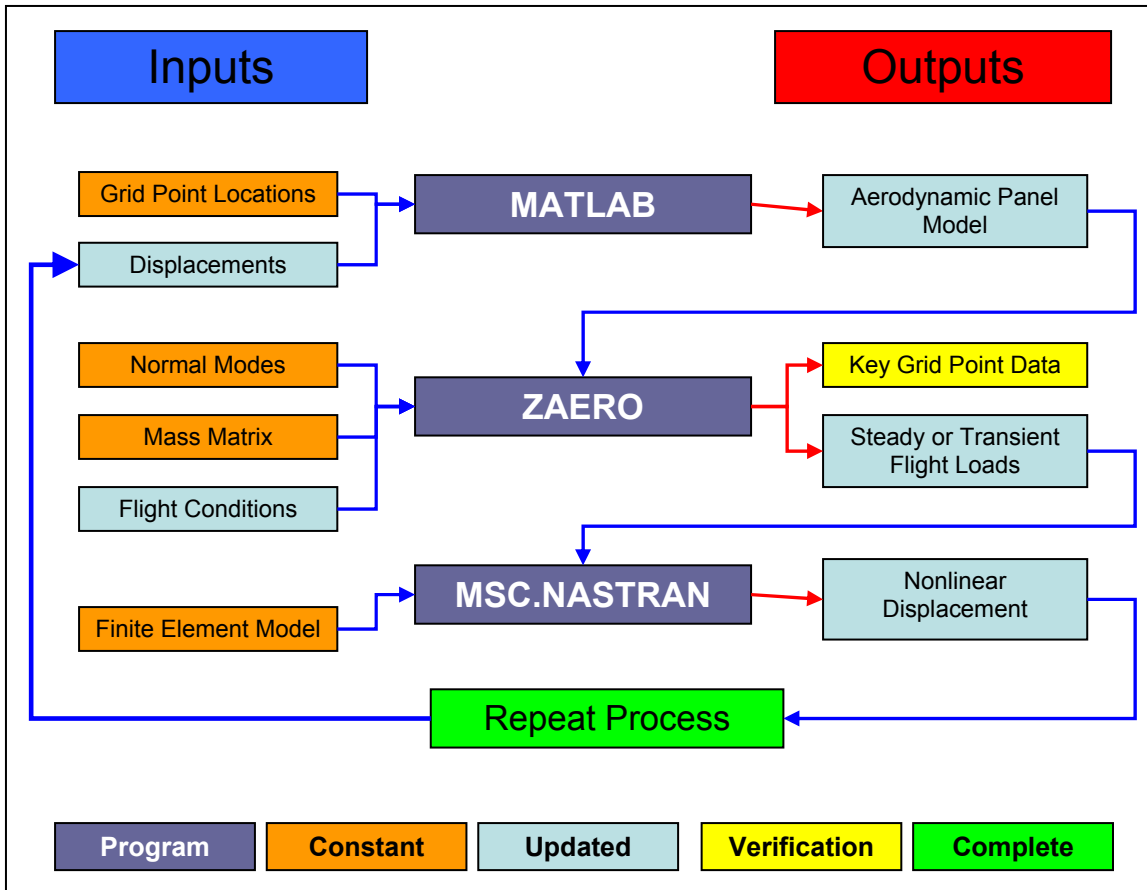


Figure 19: Flow Chart of Nonlinear Analysis

For the nonlinear analysis four separate sets of analyses were performed in order to compare the difference in the results of linear structural analysis, nonlinear structural analysis, undeformed aerodynamic flight loads, and flexible flight loads. Undeformed, refers to the position of the aerodynamic panel model relative to its initial position, flat. Deformed, refers to a panel model that has been processed through Matlab to the deformed position of the previous analysis. It should be noted that even for the analyses which use the rigid panel model, Zaero linearly estimates the position of the panel model once in the deformed position using the normal modes. Although this is not as accurate as deforming to the nonlinear shape of the wings, it does account for some wing deformation.

Analysis 1 –Undeformed Aerodynamic & Linear Structural Analysis.

The first step was to establish the baseline standard. For this thesis the standard was an analysis with flexible aerodynamic flight loads that employed linear structural analysis to solve for the deformations. Flexible loads, refers to loads where the magnitude and direction of the load changes slightly in an attempt to account for follower force effects. For this first analysis the angle of attack and SMODAL output were taken from the trim analysis and included in the gust analysis to describe the trim condition, without updating the panels. The SMODAL input transforms the elastic body modes linearly into the deformed trim condition without updating the panels. The procedure for this analysis was as follows:

Step 1: Matlab

Result: Original Undeformed Aerodynamic Panel Model

Step 2: Zaero (Trim1)

Result: Undeformed Aerodynamic Trimmed Flight Details

Step 3: Zaero (Gust1)

Result: Undeformed Aerodynamic Gust Loads

Step 4: MSC.Nastran (Linear1)

Result: Linear Deformations Due to Rigid Flight Loads

Analysis 2 - Undeformed Aerodynamic & Nonlinear Structural Analysis.

The second analysis was done to compare the effect of accounting for the geometric nonlinearities by performing nonlinear structural analysis. For this analysis the initial trim condition details were again included from the trim analysis and the aerodynamic panel model was undeformed prior to running the gust analysis. The difference between this procedure and analysis one was that a nonlinear static analysis

instead of a linear static analysis was performed by MSC.Nastran. The procedure for this analysis was as follows:

Step 1: Matlab

Result: Original Undeformed Aerodynamic Panel Model

Step 2: Zaero (Trim)

Result: Undeformed Aerodynamic Trimmed Flight Details

Step 3: Zaero (Gust + Trim Conditions)

Result: Undeformed Trim and Undeformed Gust Loads

Step 4: MSC.Nastran (Nonlinear)

Result: Nonlinear Deformations Due to Undeformed Trim and Undeformed Gust Loads

Analysis 3 – Flexible Aerodynamic & Nonlinear Structural Analysis.

The third analysis was done to account for the follower force effect of the trim condition and gust loads as well as account for the geometric nonlinearities by performing nonlinear structural analysis. To simulate the SensorCraft transitioning through the gust, the gust analysis was run multiple times with the panel model updated prior to each gust analysis run. Furthermore, because the gust is a transient analysis, the loads at specified time points were used to capture the transition from steady level flight to full gust effect. The procedure for this analysis was as follows:

Step 1: Matlab

Result: Regenerate Original Undeformed Aerodynamic Panel Model

Step 2: Zaero (Trim1)

Result: Undeformed Aerodynamic Trimmed Flight Details

Step 3: MSC.Nastran (Nonlinear)

Result: Nonlinear Deformations Due to Undeformed Trim Loads

Step 4: Matlab (Deformed)

Result: Updated Aerodynamic Panel Model

Step 5: Zaero (Trim 2)
Result: Deformed Trim Loads

Step 6: MSC.Nastran (Nonlinear)
Result: Nonlinear Deformations Due to Deformed Trim

Step 7: Zaero (Gust1 + Trim Conditions)
Result: Undeformed Trim and Gust Loads

Step 8: MSC.Nastran (Nonlinear)
Result: Nonlinear Deformations Due to Undeformed Trim and Gust Loads

Step 9: Matlab (Deformed)
Result: Updated Aerodynamic Panel Model

Step 10: Zaero (Gust2 + Trim Conditions)
Result: Deformed Trim and Gust Loads

Step 11: MSC.Nastran (Nonlinear)
Result: Nonlinear Deformations Due to Deformed Trim and Gust Loads

Step 12: Matlab (Deformed)
Result: Updated Aerodynamic Panel Model

..... Repeat steps 10 through 12 three more times to imitate the SensorCraft encountering the gust.....

Step 22: Matlab (Deformed)
Result: Deformed Aerodynamic Panel Model

Step 23: Zaero (Gust6)
Result: Deformed Trim and Deformed Gust Loads

Step 24: MSC.Nastran (Nonlinear)
Result: Nonlinear Deformations Due to Deformed Trim and Gust Loads

Flight Loads.

The flight loads generated by Zaero for the three analyses were taken from the gust analysis results with the trim conditions specified. The resulting flight loads

accounted for the trimmed flight load and the gust loads. Considering this, it was not necessary to combine the trim loads with the gust loads for the MSC.Nastran structural analysis. To mimic the transition, from steady level flight to the peak of the gust sequential load increments were used. Figure 20 shows the acceleration time history for the wingtip of the SensorCraft for the 2.50 second gust. It can be seen that the first peak acceleration and the first maximum wingtip deflection (acceleration equal to zero), occur during 2.50 seconds. This makes a 2.50 second gust a valid choice for analyzing the follower force effects. It was necessary for the peak reaction to occur during the gust for this thesis, because the loads of importance are the aerodynamic flight loads not the inertial loads which are characterized by the reactions of the SensorCraft after the gust has subsided. To characterize the transition, six time points were analyzed 0.0, 1.0, 1.7, 1.9, 2.1, and 2.3 seconds. The last five data points are marked on the acceleration time history graph for the wingtip, Figure 19 and serve to encompass the development of the gust. The three key points for this analysis were 0.0, 1.9, and 2.3. These points corresponded to the trim loads, maximum acceleration and maximum displacement respectively.

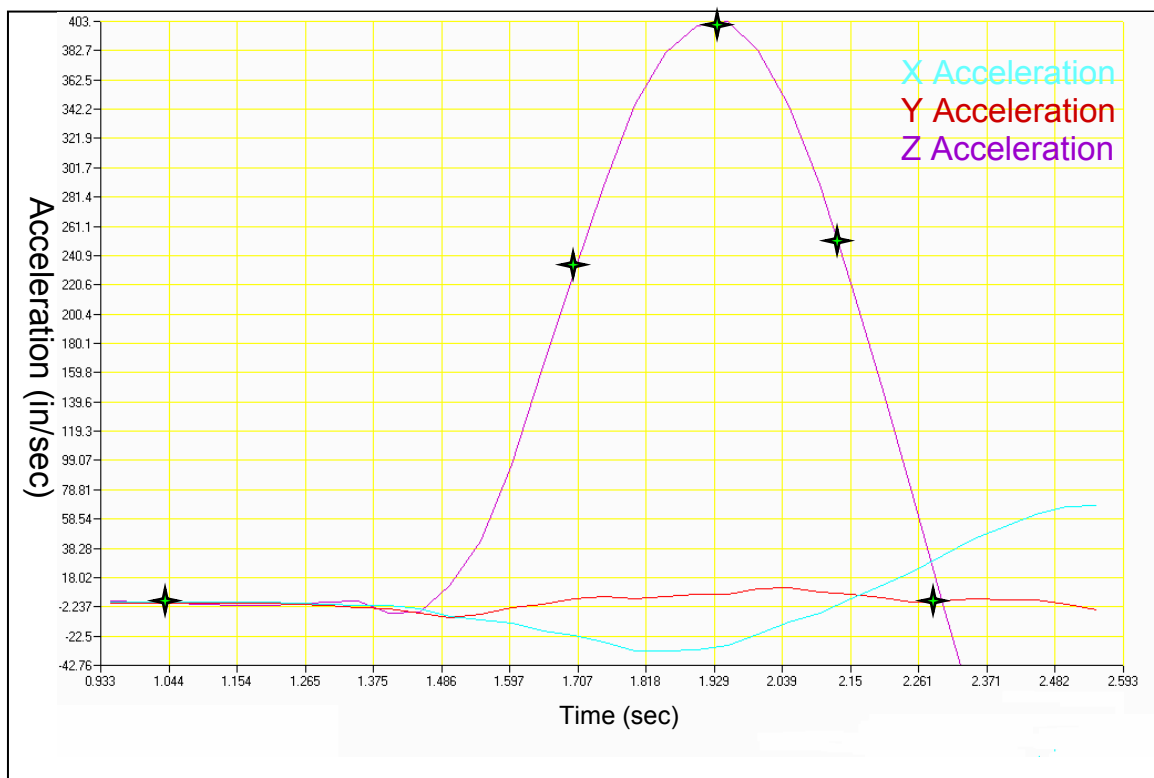


Figure 20: Acceleration of Wingtip during 2.50 Seconds Gust & Load Times

IV. Results

Material Search

The results of the material search yielded four materials used in the current SensorCraft model (410E5-04) that were important with regards to this thesis. Materials 7, 9, and 8552 were used extensively in areas known to consist of radar materials, which was important because panel buckling had occurred in early designs of the radar elements and because no radar array material specifications could be passed on to those developing the wind tunnel model. There were only two other materials used around the radar arrays and their location of use and material properties are listed in Appendix C.

Material 2 was found to be important with regards to the panel buckling which resulted from the buckling analysis. The buckled panels were corrected by increasing the thickness of the middle ply, material 2, of the composite panels. The thickness of the material 2 layer in the composite panels was the only material that was adjusted in order to prevent panel buckling.

Figure 21 displays a top view of where materials 7, 9, and 8552 are used throughout the SensorCraft. Material 7 (Fiberglass) is the outermost layer of the three materials used around known radar locations. It is also seen from the figure that material 7 is used exclusively in areas where radar arrays are supposed to be located. Material 9 (Honeycomb) is the inner most layer of the three materials. Material 8552 (Graphite Epoxy) is the middle layer and like material 9 is also used in the control surfaces of the SensorCraft on the forward wings.

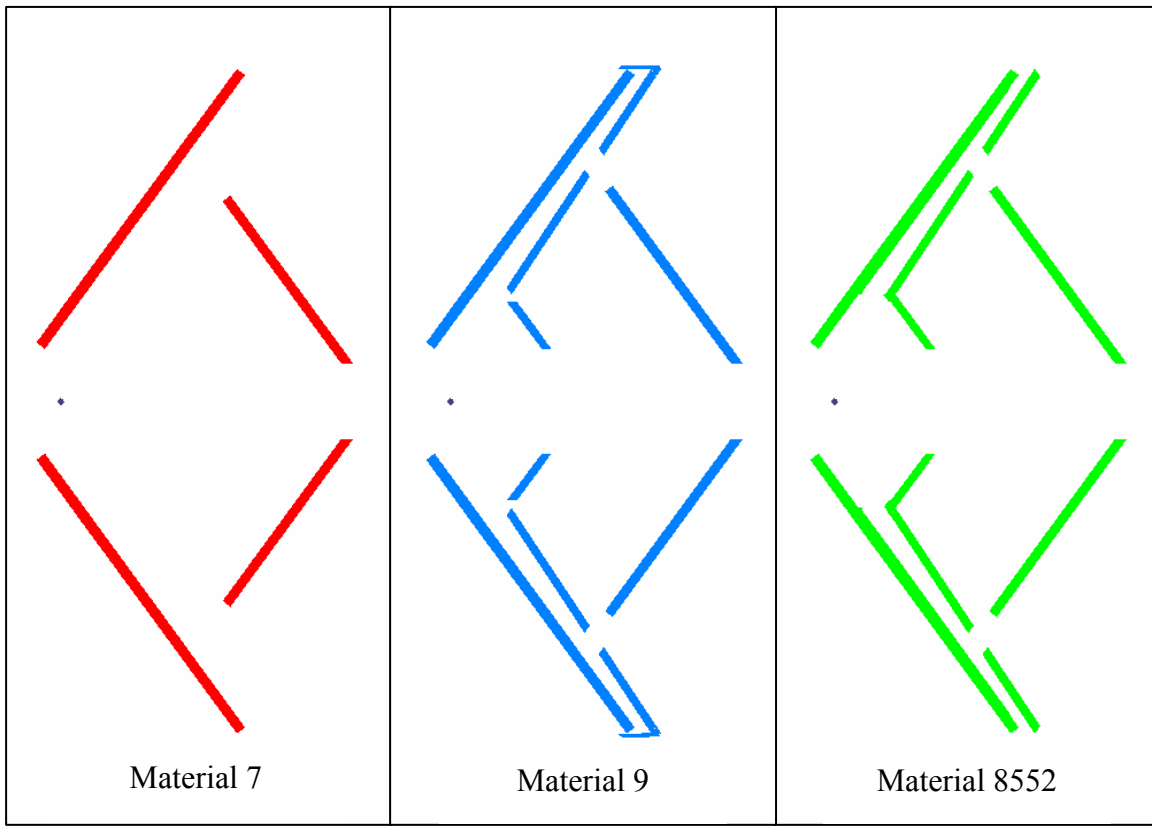


Figure 21: Locations in SensorCraft Where Materials 7, 9, & 8552 Are Used

The material properties for materials 7, 9, and 8552 are described in Table 11, where Poisson's Ratio is listed as ν , the material density is ρ , the elastic modulus is E , and the shear modulus is G . The subscripts x, y, and z refer to the direction of the respective stiffness; this is particularly relevant with material 9 which is highly anisotropic.

Table 11: Material Properties for Materials 7, 9, & 8552

Material 7 (Fiberglass)			Material 8552 (Graphite Epoxy)		
v	0.3		v	0.31	
ρ	0.064	lbs/in ³	ρ	0.056	lbs/in ³
E_x	2400000	psi	E_x	2400000	psi
E_y	2400000	psi	E_y	2400000	psi
G_{xy}	930000	psi	G_{xy}	2900000	psi
G_{xy}	330000	psi	G_{xy}	330000	psi
G_{yz}	330000	psi	G_{yz}	330000	psi
Material 9 (Honeycomb)					
ρ	0.0318	lbs/in ³	G (psi)		
xx	yy	zz	xy	yz	zx
111.19	37.0521	371.633	0	0	0
	123.466	1235.03	0	0	0
		112354	0	0	0
			10	0	0
Symmetric				8400	0
					17052

Material 7 is the outermost layer of three materials used around the radar elements, thus it is the only visible material when viewed externally, except for the control surfaces. Figure 22 is an external view of materials 7, 9, and 8552, with the yellow box on the right wing marking the location where Figure 22 was taken.

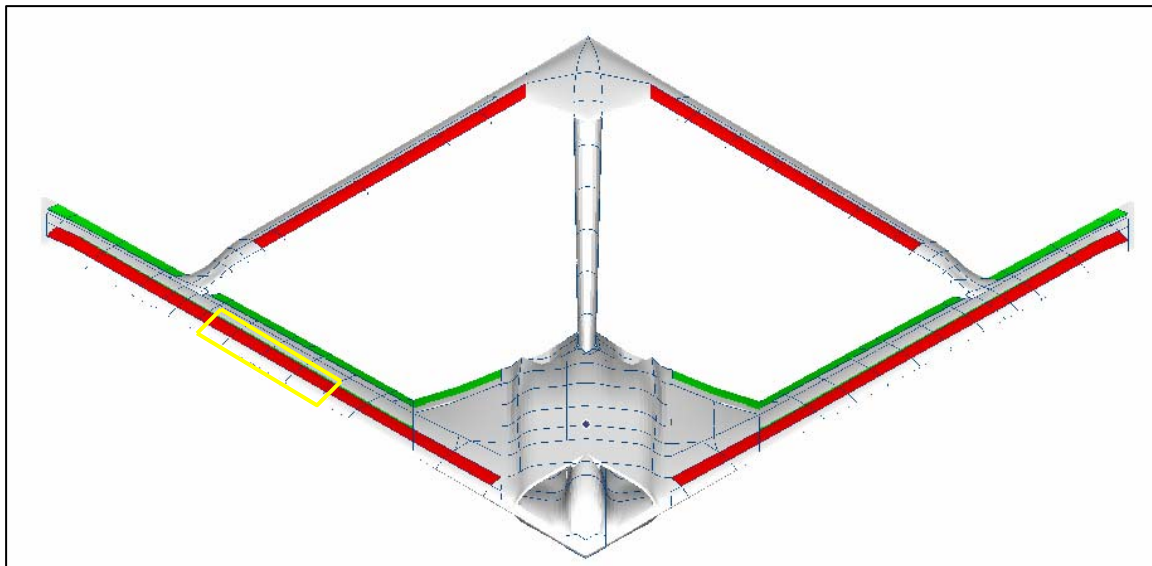


Figure 22: External View of Materials 7, 9, & 8552 in the SensorCraft

Figure 23 is an internal view of these materials with two separate views of the same cross-section, high view and low view. The upper and lower surfaces are two separate surfaces with material 7 forming the outer most skin for portions of the upper and lower surfaces of the wings. The two views show the order of the layers with material 7 (red) being first followed by material 8552 (green), and then material 9 (blue).

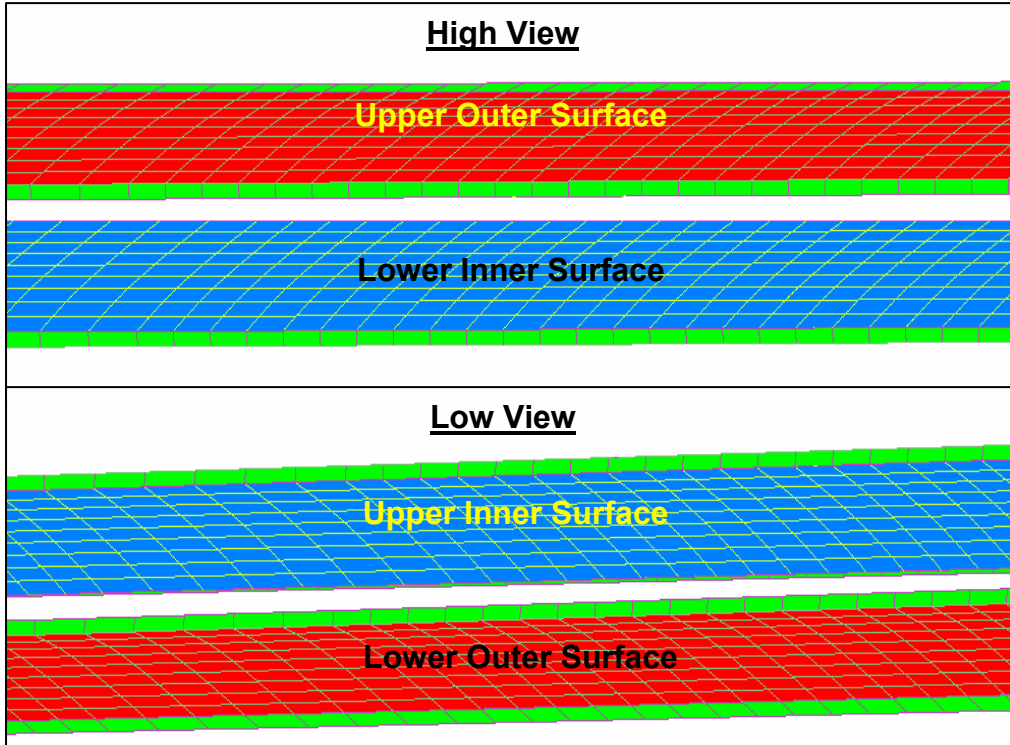


Figure 23: Composite Lay-up of Materials 7, 9, & 8552

Material 2 is used throughout the SensorCraft as the middle ply in the composite layers. Figure 24 shows the panels where the thickness of material 2 was increased to prevent panel buckling and the material properties associated with this material. The two outer layers for these composite panels were the same with respect to each other. The outer layers did vary depending on the properties and location of use. In the connection region between the two wings, the yehudi sections, and part of the diamond sections in the tail the outer layers of the composite was material 8552. In the wing and the other portion of the tail the outer layers were material 7.

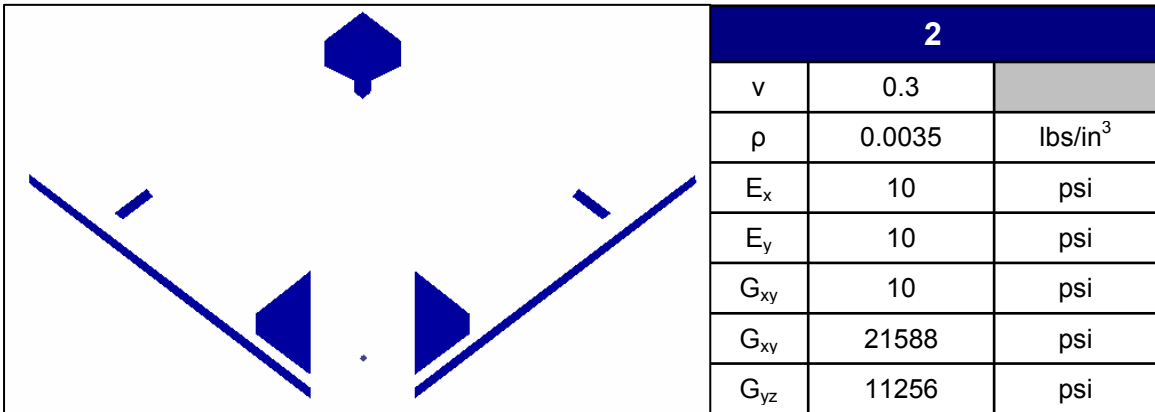


Figure 24: Location of Use and Material properties for Material 2

Normal Modes Analysis

Table 12 describes the results for the first twenty modes for the free-free normal modes analysis. **Symmetry**, describes whether the motion of the wings relative to each other is symmetric (**S**) or anti-symmetric (**A**). **Motion**, describes the type of travel exhibited by the forward and aft wings, or the boom respectively, bending (**B**), torsion (**T**), and rigid translation (**R**). **Mode**, describes the degree of the motion. For example a motion of “**B**” and a mode of “**1**”, represents 1st bending. The tables describe the most prominent deformations, that is to say that both bending and torsion may have occurred in the same mode, but if one was significantly less in magnitude then the other it was not recorded.

As is expected the first six modes exhibit only rigid body motion. The first flexible normal mode for the free-free analysis occurs at a frequency of 0.744 Hz. It is also shown that the first non-rigid body mode is a symmetric mode and the second is anti-symmetric. Even though both bending and torsion do occur simultaneously in several of the modes, only prominent deformations were recorded. Considering this it should also be noted that bending is the dominant modal shape of the aft wing and that torsion is

either not existent or is minimal in comparison. This table also shows that for all anti-symmetric modes the boom experiences either bending in the YZ plane or torsion and that boom torsion is never involved in a symmetric mode.

Table 12: Description of Normal Modes for Free-Free Model

Mode	Frequency (Hz)	Symmetry	Forward Wings		Aft Wings		Boom			Rigid Body Motion
			Motion	Mode	Motion	Mode	Motion	Mode	Plane	
1	0.0000000	NA	NA	NA	NA	NA	NA	NA	NA	RX
2	0.0000000	NA	NA	NA	NA	NA	NA	NA	NA	RX
3	0.0000000	NA	NA	NA	NA	NA	NA	NA	NA	RY
4	0.0000000	NA	NA	NA	NA	NA	NA	NA	NA	TY
5	0.0000000	NA	NA	NA	NA	NA	NA	NA	NA	RY
6	0.0000000	NA	NA	NA	NA	NA	NA	NA	NA	TZ
7	0.7428480	S	B	1	R	NA	B	1	XZ	NA
8	0.9496210	A	B	2	B	1	B	1	YZ	NA
9	1.9091580	A	T	1	B	1	T	1	NA	NA
10	2.0147960	S	B	2	B	2	B	1	XZ	NA
11	2.4107930	S	T	1	B	1	B	1	XZ	NA
12	2.6962840	A	B	3	B	2	B	1	YZ	NA
13	2.8500630	S	T	2	B	1	B	1	XZ	NA
14	3.9803640	A	B	1	B	1	T	1	NA	NA
15	4.4499570	A	T	1	B	2	B	1	YZ	NA
16	5.1664310	S	B	3	B	2	R	NA	XZ	NA
17	5.2625620	A	T	2	B	2	T	1	YZ	NA
18	6.2203730	A	B	3	B	1	B	1	NA	NA
19	6.6895690	S	T	1	B	2	B	1	XZ	NA
20	6.8868620	S	B	1	B	2	B	1	XZ	NA

Figure 25 displays the first four non-rigid body modes for the free-free normal modes analysis. The gray image is the undeformed SensorCraft model and the contour mapped image is of the deformed model. As can be seen from the images the normal modes for the free-free analysis are very clean and control surface vibration is minimal. It is also seen that the first non-rigid body mode is symmetric and the aft wings are relatively rigid,

and the second mode is anti-symmetric with the aft wings bending slightly. The first six rigid body modes can be seen in Appendix A.

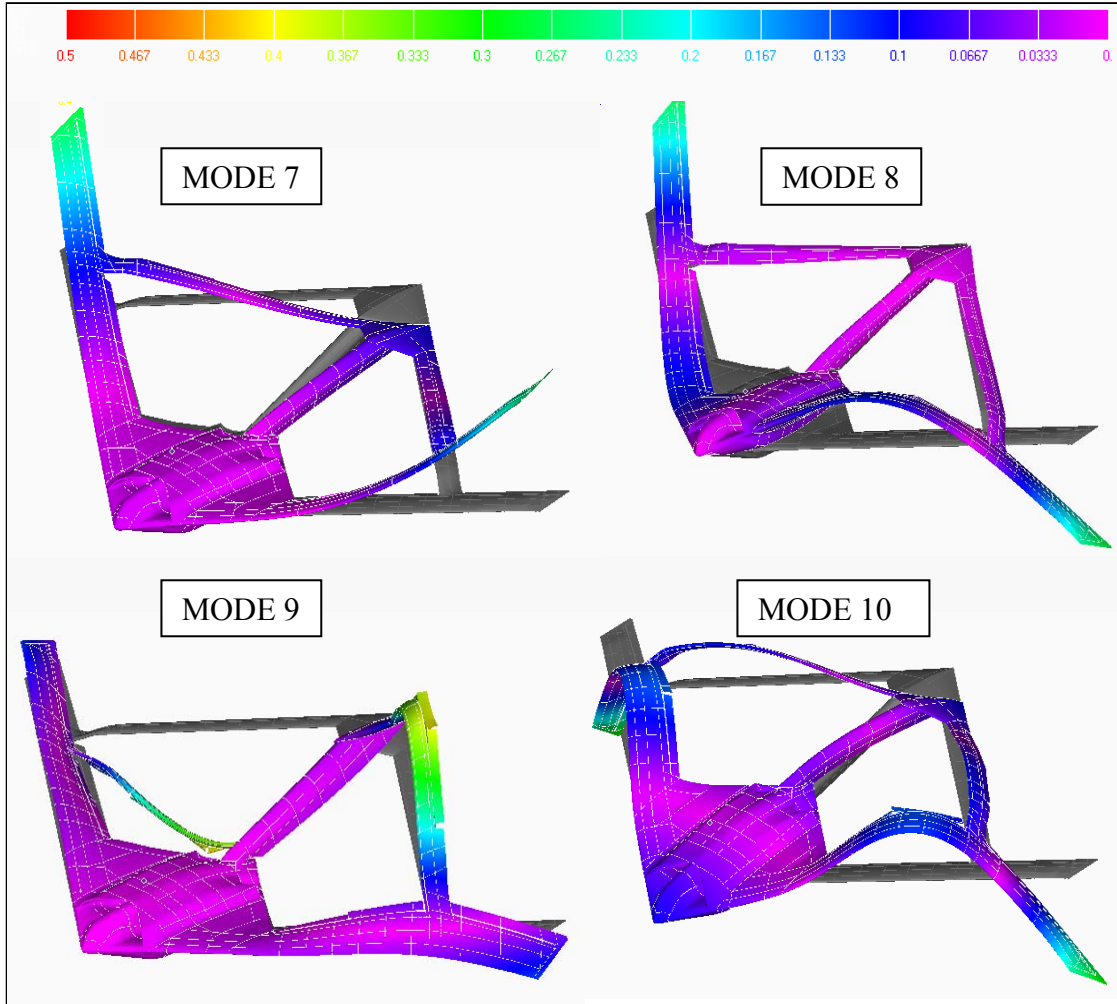


Figure 25: First Four Non-Rigid Body Modes for Free-Free Normal Modes Analysis

Table 13 describes the results for the first twenty modes for the clamped normal modes analysis. Figure 26 shows the clamped node relative to the center of gravity found from the trim analysis. The node for the center of gravity does not exist in the Boeing model. The notation for this table is the same as the previous table.

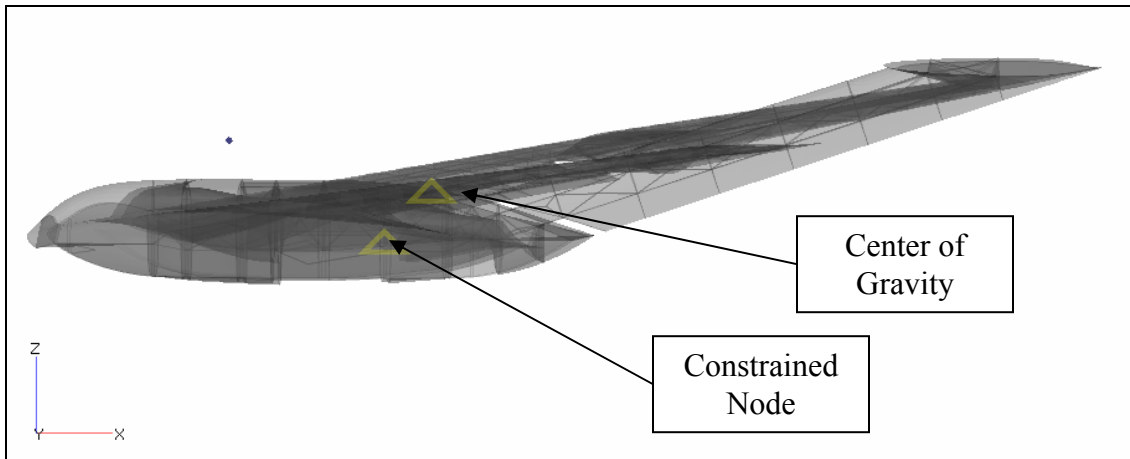


Figure 26: Location of CG and Constrained Node

The first normal mode for the clamped analysis occurs at a frequency of 0.440 Hz and is anti-symmetric. Mode 9 at a frequency of 4.37 Hz is the first normal mode to exhibit both significant bending and torsion in the forward wings during a single mode. Bending is also shown to be a dominant modal shape of the aft wings for the clamped normal modes analysis. This table also shows that for all anti-symmetric modes the boom experiences either bending in the YZ plane and/or torsion and that torsion of the boom is never involved in a symmetric mode.

Table 13: Normal Modes Description for Clamped Model

Mode	Frequency (Hz)	Symmetry	Forward Wings		Aft Wings		Boom		
			Motion	Mode	Motion	Mode	Motion	Mode	Plane
1	0.4395345	A	B	1	R	NA	B	1	XY
2	0.7272263	S	B	1	B	1	B	1	XZ
3	0.8723732	S	T	1	R	NA	B	1	XZ
4	1.6809690	A	B	2	B	1	B	1	XY
5	1.9695870	A	T	1	B	1	T	1	NA
6	2.0988630	S	B	2	B	1	B	1	XZ
7	2.2241810	A	B	2	B	1	T	1	NA
8	2.7840850	S	T	1	B	1	B	1	XZ
9	4.3671840	A	B,T	2,1	B	1	B	1	XY
10	4.7927040	A	B	3	B	2	T	1	NA
11	4.9677950	S	B	3	B	1	B	1	XZ
12	5.4040060	A	T	2	B	2	B,T	1,1	XY
13	6.5906900	S	T	1	B	1	B	1	XZ
14	6.9163640	S	T	1	B	2	B	1	XZ
15	7.6239510	A	B,T	3,1	B	1	B	1	XY
16	7.7613120	A	T	1	B	2	B	1	XY
17	7.9590870	S	T	1	B	1	B	1	XZ
18	8.3943080	S	T	1	B	2	B	1	XZ
19	8.9552070	A	T	1	B	1	B	1	XY
20	9.0283350	S	B	3	B	2	B	1	XZ

Figure 27 displays the first four modes for the clamped normal modes analysis.

The figure properties are the same as for the free-free analysis. As can be seen from the images the normal modes for the clamped analysis demonstrate significant control surface flutter. The next six modes for the clamped analysis can be seen in Appendix A.

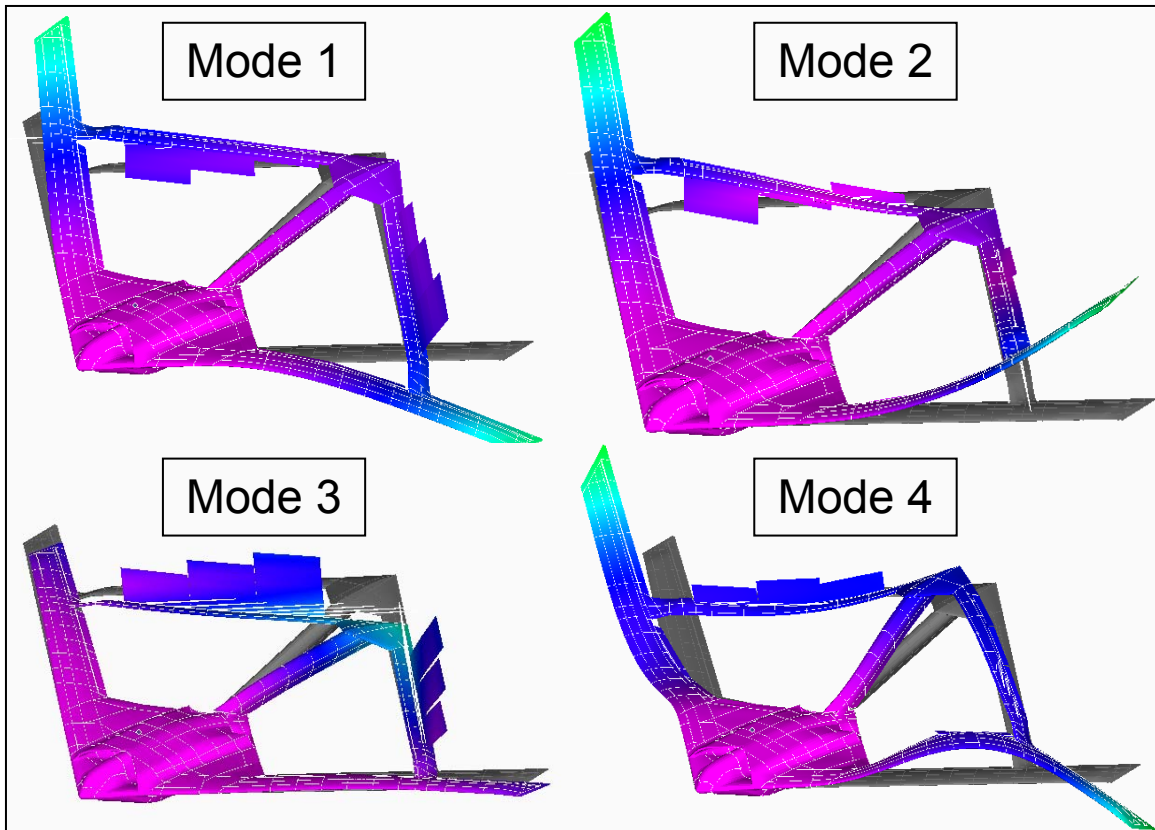


Figure 27: First Four Normal Modes for Clamped Analysis

A comparison of the normal modes analyses for the free-free analysis and the clamped analysis yield several interesting differences. First, the first mode for the free-free analysis occurs at roughly 0.7 Hz while the first mode for the clamped analysis occurs at roughly 0.4 Hz. Second, the first flexible mode for the free-free analysis is symmetric while the first mode for the clamped analysis is anti-symmetric. Thus, even at roughly equivalent frequencies the modal shapes for the two analyses are drastically different. Fourth, within the first twenty modes the clamped modal analysis exhibits both torsion and bending of the forward wings and boom during a single mode, while the free-free analysis does not. Fifth, the free-free analysis has minimal control surface activity while the clamped model exhibits significant motion of the aft control surfaces. The forward control surfaces remain motionless for both analyses.

Linear Static Analysis

Table 14 shows the results for the linear static analysis with the most severe load sets highlighted in yellow. In the first row, the first number corresponds to the number of elements considered (sample size) out of the total number of maximum stressed elements (sample space). A hit refers to the number of times a maximum stress occurred in the corresponding sample size. For example, the number of recorded maximum stressed elements for the eighteen gust load cases was 4681. Of these 4681 the top 1000 maximum stressed elements were compared. From this comparison load cases 31411, 31412, and 31413 each had 102 recorded maximum stressed elements out of 1000. The 102 hits for each case corresponds to the highest frequency of maximum stressed elements out of 1000 samples. An example of the first 100 maximum stressed elements for the gust comparison, can be seen in Appendix D. From Table 13 and from the load name definitions the critical parameter can be discerned for each case. For all load cases, the critical parameter is the 100% fuel capacity, this is designated by the first digit in the load set name being three. For the pull-up case, the two most critical conditions begin with a designation of four, which corresponds to a 10% increase in the applied loads generated from the 100% fuel condition. For the roll maneuver high mach, indicated by second digit of four, is also a critical parameter.

Table 14: Ranking of Load Sets Based On Number of Hits

1000 of 4681		500 of 2341		500 of 2081		500 of 1821	
Gust		PULL-UP		PUSH-OVER		ROLL	
Load Set	# Hits	Load Set	# Hits	Load Set	# Hits	Load Set	# Hits
31411	102	4121	76	3411	92	3431	82
31412	102	4421	76	3311	89	3438	81
31413	102	3421	74	3111	89	3432	78
31414	97	3221	74	3211	89	3132	78
31421	97	3121	74	1411	48	3138	76
11411	96	1121	35	1311	33	2138	64
31422	88	1421	33	1111	30	1138	41
31423	81	1321	31	1211	30		
31424	75	1221	27				
11412	40						
11421	31						
11413	26						
11422	20						
11432	18						
11423	12						
11431	7						
11442	6						
11441	4						

The maximum stresses were monitored in four element types used in the construction of the SensorCraft; rod, plate, laminate, and solid elements. The locations where these elements are used in the construction of the SensorCraft can be seen in Figure 28.

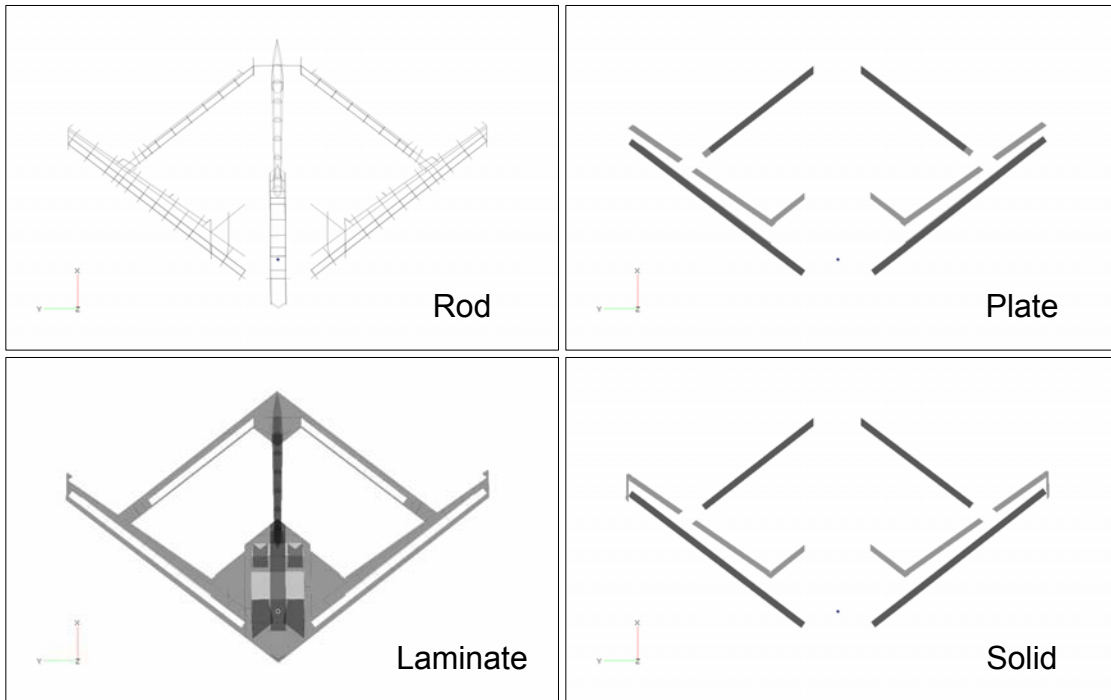


Figure 28: Locations Where Rod, Plate, Laminate and Solid Elements Are Used

Figure 29 shows a comparison for each of the linear static analyses and the maximum stresses found in these elements. For the rod elements the maximum stress compared was the axial stress and for the plate, laminate, and solid elements the VonMises stress was used. It can be seen from the graphs that the rod elements experience the highest stress in every case, and that the solid elements experience by far the least amount of stress. These graphs also clearly show that the gust load case experiences significantly more stress than the other load cases. Furthermore, gust set 31411 is the most severe loading condition and experiences at least double the stress as the other load sets.

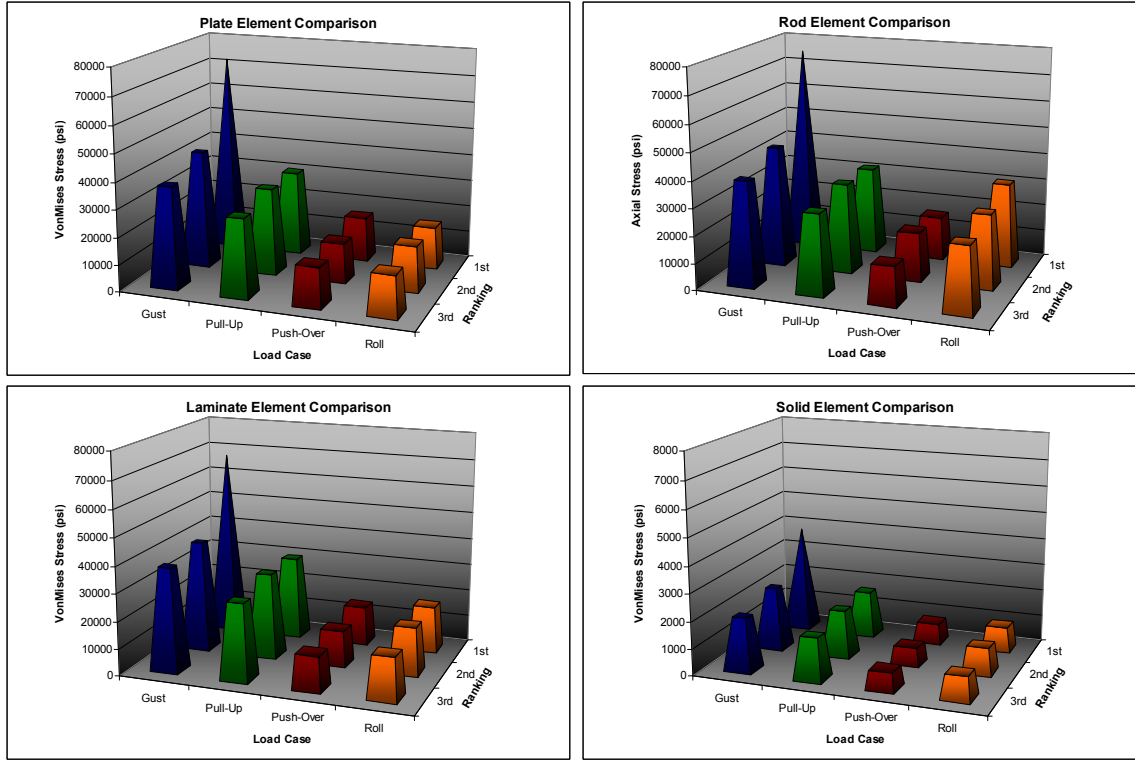


Figure 29: Stress Comparison for Four Element Types

Table 15 lists the deformations from the linear static analysis for the three most critical load cases for each load set. The deformations for each of these cases can be seen in Appendix E. For each of the gust sets, the maximum displacement occurs at the wing tips. For each of the pull-up sets, the maximum displacement occurs in the wing tips. Also the maximum displacement occurs in load set 4421, which was not the most stressed load set. This can be attributed to the slight torsion in the boom for load set 4121, which results in an increase in the bending of the left wing, when compared to 4421. For each of the push-over sets, the maximum displacement occurs at the wing tips. For each of the roll sets, the maximum displacement occurs at the wing tips. The maximum displacement occurs in load set 3438, which was not the most stressed load case. This can be attributed to torsion in the boom for load case 3431. This torsion

results in an increase in bending of the right aft wing, when compared with load case 3438.

Table 15: Displacement Comparison for Critical Load Cases

GUST		PULL-UP	
Load Set	Displacement	Load Set	Displacement
31411	55.08"	4121	23.76"
31412	34.15"	4421	24.62"
31413	32.69"	3421	22.38"
PUSH-OVER		ROLL	
Load Set	Displacement	Load Set	Displacement
3411	12.64"	3431	12.01"
3311	11.13"	3438	12.99"
3111	11.49"	3432	11.81"

Buckling Analysis

The iterative process in optimizing the panel structure for the SensorCraft consisted of four essential modifications to the panel structure and one nonessential modification done to clean-up the global buckling mode. The modifications made to the SensorCraft were done to prevent the model from exhibiting panel buckling up until a load factor (eigenvalue) of 2.6. Once this load factor had been reached it was considered buckling safe because it was well beyond the critical limit of 1.5. Panel buckling was corrected significantly beyond the buckling limit because the buckled panel could prevent the nonlinear analysis from converging past the point of the buckled panels. The result of this is that the range of comparison between the linear and nonlinear analysis would be severely limited. It should be noted though that if all the panels were modified to prevent buckling up to the first global buckling mode then the current value of the global buckling load factor would increase. This is as expected in that if more material is

included in the structure the structure will become stronger. This hypothesis was tested and found to be true.

The first panel buckling occurred at an eigenvalue of 1.44 in the tail section of the SensorCraft. Because panel buckling does not occur until an eigenvalue of nearly 1.5 it is apparent that some measures have been taken to develop a buckling safe design. To eliminate the panel buckling, the core thicknesses of the composite elements (material 2) were doubled. Figure 30 shows the locations of the eliminated panel buckling modes and their corresponding eigenvalue when they occurred.

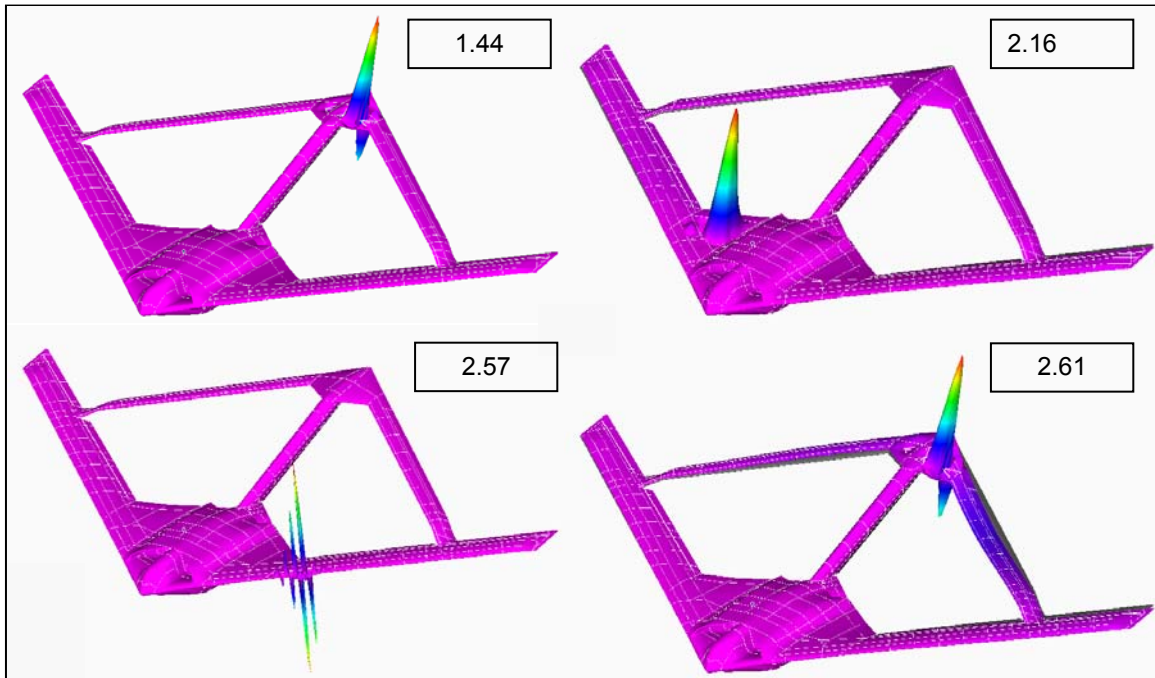


Figure 30: Panel Buckling In SensorCraft

Removing the panel buckling was necessary in order to find the global buckling mode, because the only buckling results obtained prior to the modifications were repetitive panel buckling. The nineteen remaining panel buckling modes before the global buckling mode are repetitions of these modes; this is to say that the adjusted

properties are not sufficient to eliminate panel buckling until the onset of global buckling, but further modifications to these properties should prevent panel buckling until global buckling occurs. However the modifications necessary to accomplish this seem to be unrealistic. For example the tail section core thickness was increased to four times the original thickness and panel buckling in this region still occurred prior to global buckling.

Figure 31 shows the first global buckling mode. The first global mode occurs at an eigenvalue of 3.71, which is well beyond the safety limit. These results show that the model is buckling safe within the confines of a linear analysis. The buckled structure is the aft wing, which is expected, as bending was the only mode present in the normal modes analysis for the aft wings and because a gust will increase the lift developed by the forward wings, thereby further compressing the aft wings. It should also be noted that this is an antisymmetric buckling case; the aft wings deflect in opposite directions.

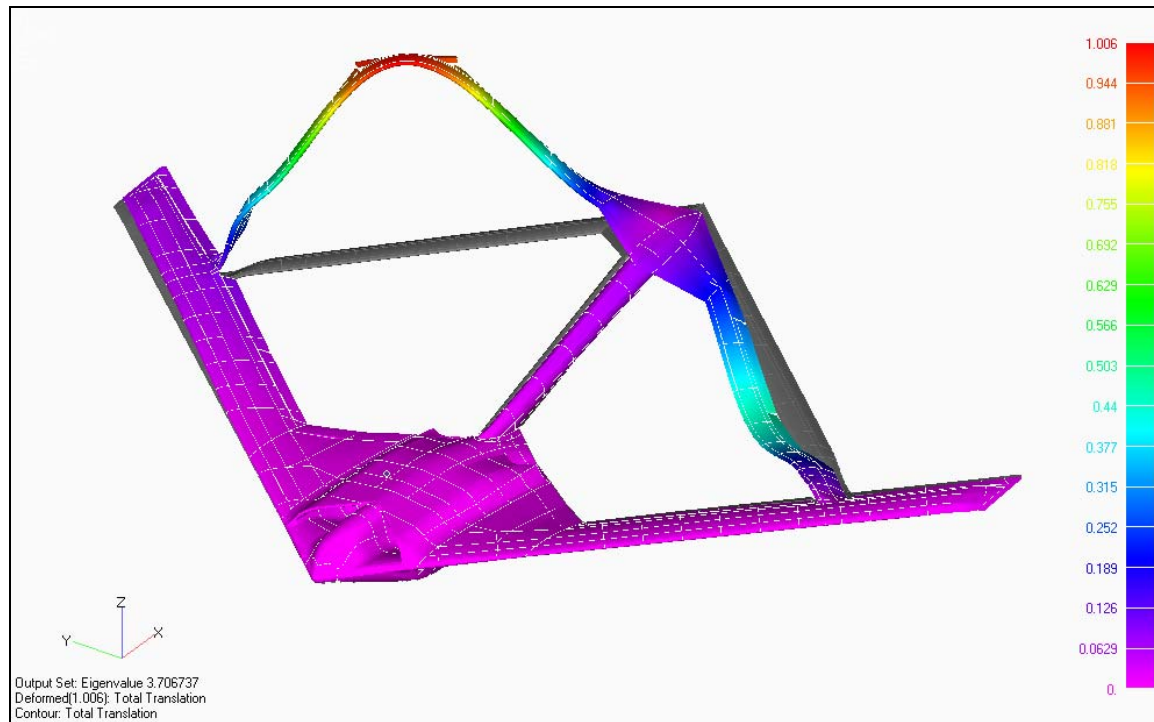


Figure 31: First Global Buckling Mode

Figure 32 shows the second global buckling mode, which occurs at an eigenvalue of 3.97. This mode also exhibits torsion in the boom but unlike the first mode both aft wings deflect upward. The buckled section of the SensorCraft with the largest displacement in the second mode is the right aft wing, opposite from the first. These results are interesting, because for all the panel buckling modes the first pair of modes would exhibit buckling on half of the structure and the second would mirror the panel buckling, but on the opposite side.

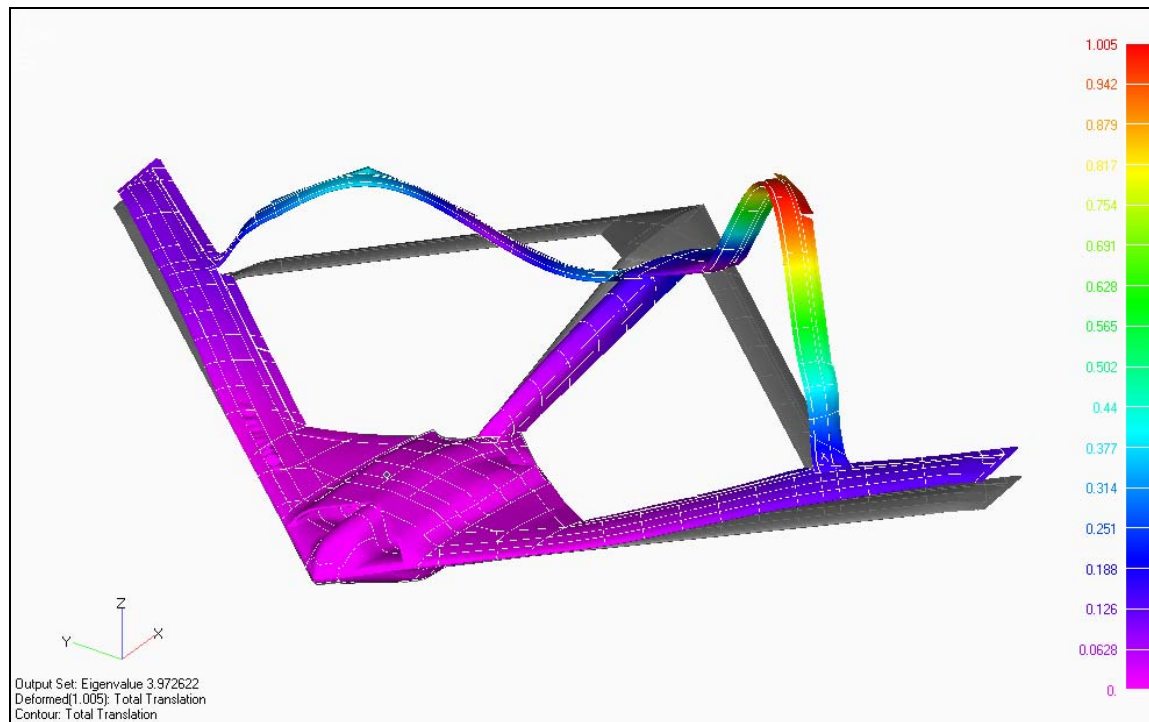


Figure 32: Second Global Buckling Mode

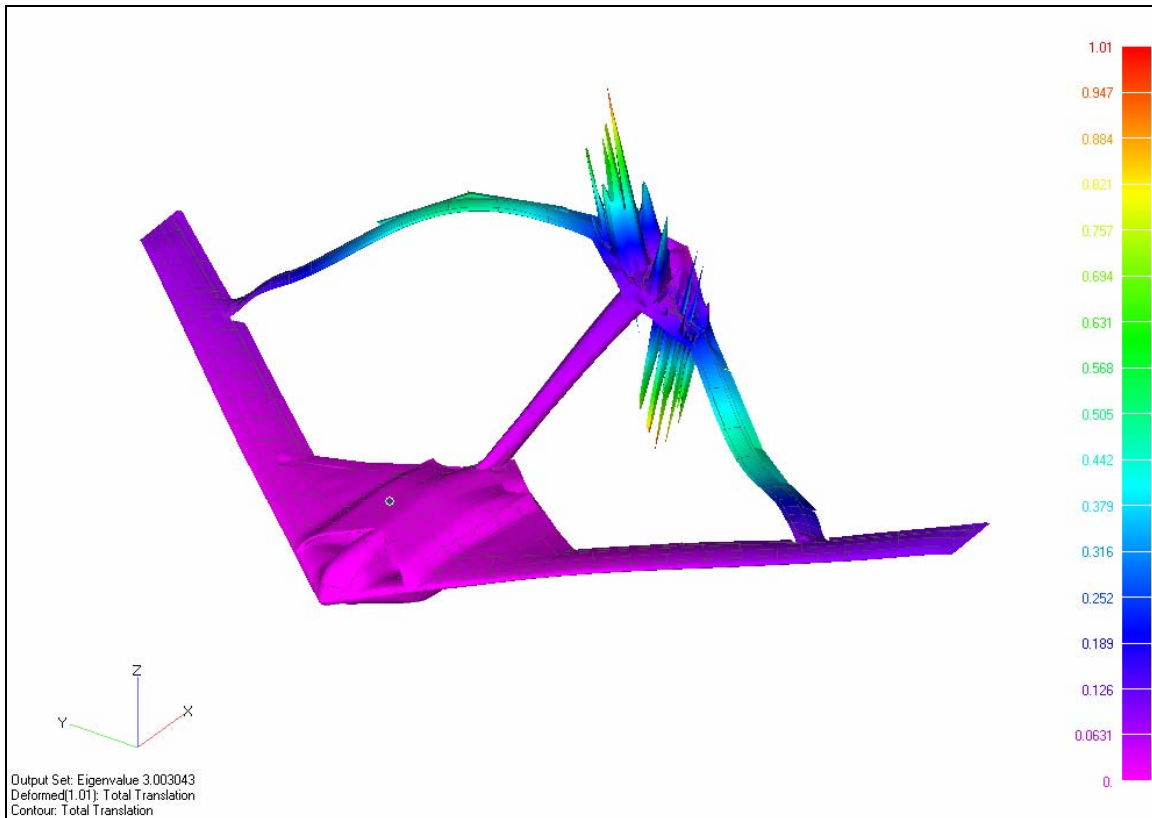


Figure 33: First Global Buckling Mode for Unmodified Model

Figure 33 depicts the first global buckling mode for the original model without any panel modifications imposed. This panel and global buckling mode occurs at an eigenvalue of 3.00. From the figure it can be seen that panel buckling is substantial as the magnitude of the panel deformation is more than twice the global deformation. From these results it is also seen that even though the global buckling mode may occur in sections were no modifications have been made to the panels, the load factor where the global buckling does occur is impacted. This is seen from the fact the modified SensorCraft can incur 70% more load than the unmodified SensorCraft before aft wing global buckling occurs.

Nonlinear Aeroelastic & Nonlinear Structural Static Analysis

For the combined nonlinear aeroelastic and structural static analysis, the examination of the gust accelerations profiles provided the necessary details concerning the best gust length. Because the desire for this thesis was to incorporate the follower force effect on the SensorCraft it was necessary for the reaction to occur during the gust and not after.

Figure 34 displays the acceleration time history for the wingtips of the SensorCraft during a gust with a length of 1.25 seconds. The results from this gust acceleration profile provided information concerning the reasoning behind the 100% fuel cases being the most critical condition. This was important because this was contradictory to previous joined-wing research by AFIT personnel, on simplified structures. This can be attributed to the fact that the previous studies were optimized with fewer load cases, thus a more flexible structure, where as this study incorporates the involves a much stiffer model and the transient effects of the gust. Examining the wingtip acceleration time history for a gust length that is still relatively long, compared to the SensorCraft helps to explain these results. First, the second positive acceleration peak is roughly twice the first positive peak. Second, the maximum acceleration is in the negative z-direction, thus counter to the direction of the lifting forces. Third, the gust has completely subsided before the wings react substantially. Consequently the gust effect is more of an impulse response than the desired steady state response. This gust length provides larger deflections, but these deflections are a result of inertial forces rather than aerodynamic forces and thus incorporating follower force effect would be futile.

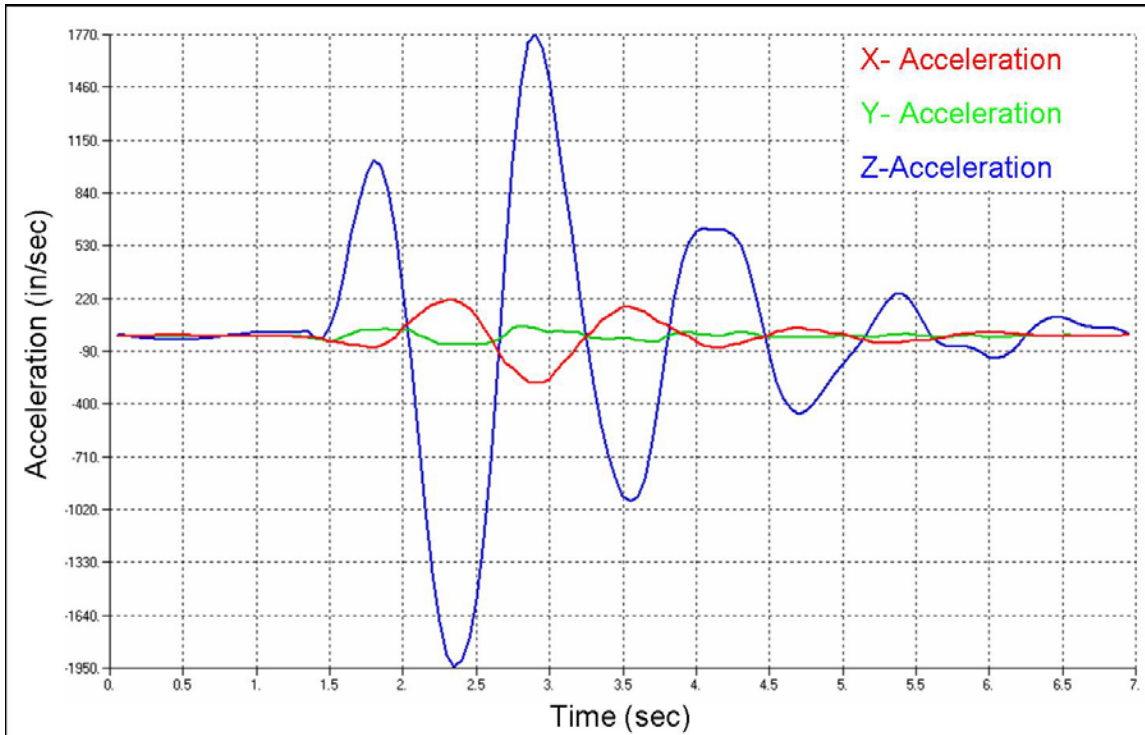


Figure 34: Wingtip Acceleration Time History for a Gust Length of 1.25 Seconds

The 1.25 second length gust did however play an important role in the validation of the results. The trim angle of attack and the lift curve slope for the SensorCraft were obtained from the trim analysis. Using this information, the effective angle of attack, α_e of the trim condition was derived. Table 16 lists the 1g trim details calculated by the Zaero trim analysis and the zero lift angle of attack derived from the intersection of the lift curve slope, $C_{L\alpha}$ and the coefficient of lift equaling zero.

Table 16: 1G Trim Details for SensorCraft

$C_{L\alpha}$ (1/Degrees)	Trim α (Degrees)	Trim C_L	α of Zero Lift (Degrees)
0.13973	2.78	0.88272	-3.537

Figure 35 depicts the results for calculating the effective angle of attack of the gust .

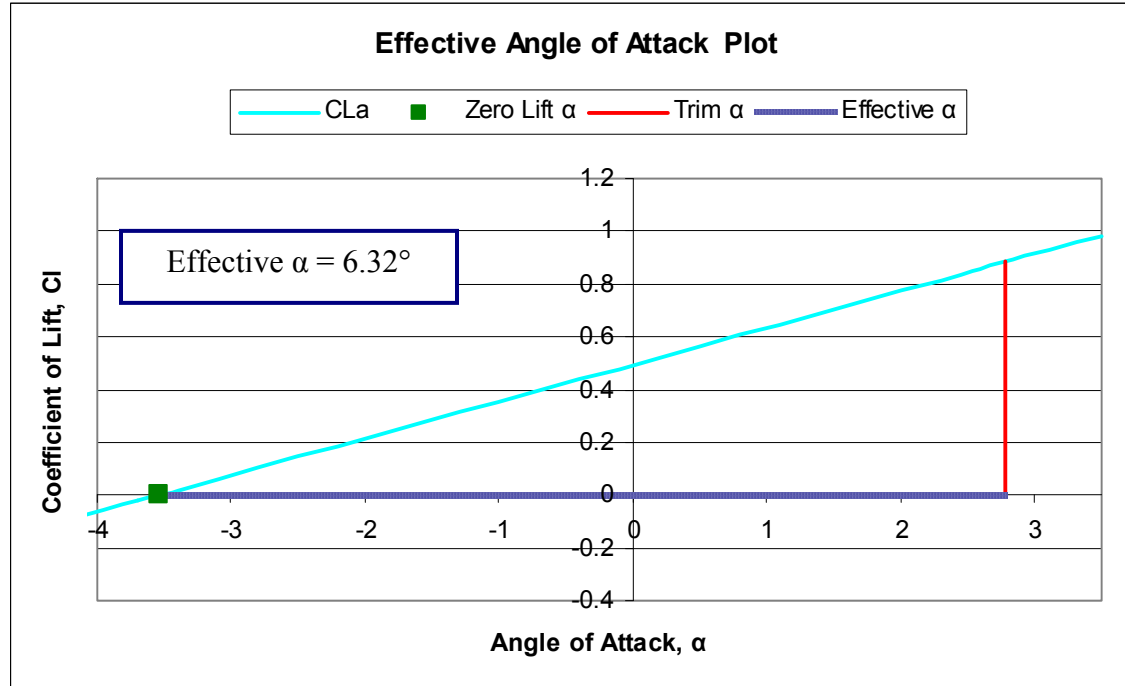


Figure 35: Effective Angle of Attack Calculation

The instantaneous angle of attack change due to the gust was calculated.

$$\alpha_{i,Gust} = \tan^{-1} \left(\frac{V_{Gust}}{V_{SensorCraft}} \right) \quad (36)$$

The next step was to include a gust alleviation factor

$$K = \frac{0.88\mu}{5.3 + \mu} \quad (37)$$

where the mass ratio, μ is defined as:

$$\mu = \frac{2(W/S)}{\rho g \bar{c} C_{L\alpha}} \quad (38)$$

The effective angle of attack of the gust then becomes

$$\alpha_{e,GUST} = K \alpha_{i,GUST} \quad (39)$$

By taking the ratio of the gust effective angle of attack to the trim effective angle of attack and multiplying by the gust alleviation factor, a load factor estimate can be obtained for the gust load based on the trim load, equation (40).

$$\lambda_{Gust} = \left(\frac{\alpha_{e,GUST}}{\alpha_{e,TRIM}} \right) (K) \quad (40)$$

Table 17 lists the calculated effective angles of attack for the trim and gust conditions respectively, as well as the gust alleviation and load factor.

Table 17: Effective Angles of Attack, Gust Alleviation Factor, and Load Factor

Trim α_E	Gust α_E	Gust K	λ_{Gust}
6.32°	12.3°	72%	1.40

Nonlinear static structural analysis was performed by MSC.Nastran with the gust loads from the 1.25 second gust. Table 18 lists the results from the estimation and MSC.Nastran analytical solutions and confirmed that the gust effect had been accurately accounted for.

Table 18: Gust Deflection Comparison for Estimation and Analytical Solutions

Estimated Gust Deflection	Analytical Gust Deflection
23 inches	24.19 inches

Figure 36 depicts the deflections due to the two loading conditions. It should be noted that the illustration for the gust deflection depicts the trimmed gust condition, which is the trim loads plus the gust load. The listed value for the gust deflection are the result of subtracting the trim deflection from the total deflection. The Zaero/MSC.Nastran analysis calculated a deflection that was 1.19 inches larger than with the effective angle of attack estimation.



Figure 36: Comparison of Maximum Deflection for Trim and Gust Analysis

Table 19 lists the first positive peak accelerations produced by the respective gust on the wingtips of the SensorCraft. The tabulated deflections are the results from a linear analysis which includes the trim force deflections. The 5.00 second gust does not have a substantial effect on the SensorCraft as the transition is too gradual, thus the resulting deflection only being approximately five inches greater at them time of maximum acceleration. The gust lengths of 2.50 seconds and 3.75 seconds produce roughly the same amount of deflection. After examining the transient effects of the gust by applying the forces following the second positive peak acceleration, both the 2.50 and 3.75 second gust length resulted in a larger deformation after the gust had subsided than during the gust. However, because the peak acceleration from the 2.50 second gust was almost twice that of the 3.75 second gust and because the deflection due to the 5.00 second gust was unsubstantial, the 2.50 second gust length was chosen as the gust length to use for the nonlinear static with follower forces analysis.

Table 19: Comparison of Maximum Accelerations and Deflections

Gust Length (sec)	Time (sec)	First Peak Acceleration (in/sec ²)	Displacement (in)
1.25	1.9	1034	40.85
2.50	1.9	402	28.71
3.75	2.0	204	28.31
5.00	2.0	122	21.66

Table 20 tabulates the calculated wingtip deflection for three different analysis techniques. The **Linear** column list the wingtip deflection calculated by a MSC.Nastran linear static analysis from applying the steady 1-g trim loads generated by zero for the 2.50 second gust on an originally undeformed aerodynamic panel model. The **Nonlinear** column lists the deflection from a MSC.Nastran nonlinear static analysis with the large displacement option activated. **Nonlinear Up** lists the wingtip deformations from the iterative procedure of updating the panel model for each time step and performing a nonlinear static analysis with the resulting loads. To clarify the first and second analysis techniques did not update the panel model; **Nonlinear Up**, updated the panel model five times. These results confirm that for small deflections, less than three feet for a 150 foot span, the geometric nonlinearities and follower force effects do not produce a substantial difference in deflection. By accounting for the follower force effect through updating the panel model and regenerating the forces, **Nonlinear Up**, the deflections were only slightly larger then the other analysis techniques. Several aspects of these analyses should be considered. First, the maximum nonlinear wingtip deflection of 2.82 feet produces a change in the dihedral of the wing by a little more than two degrees. This small change in dihedral does not provide substantial change in the direction of the lift vector. Second, Zaero used the SMODAL card from the trim analysis. This transformation, accompanied with the small displacement supports the equivalent

displacements for the first several time points between the two nonlinear analyses.

Considering these details, it is not surprising that the difference between the three analysis techniques was not substantial. However, for larger deflections accounting for these aeroelastic nonlinearities could prove essential.

Table 20: Comparison of Analysis Techniques

Time (sec)	Linear (in)	Nonlinear (in)	Nonlinear UP (in)
0.0	16.35	16.42	16.47
1.0	18.08	18.13	18.14
1.7	23.23	23.31	23.31
1.9	28.67	28.72	28.72
2.1	32.77	32.77	32.78
2.3	33.78	33.80	33.81

Figure 37 illustrates a unique characteristic of joined-wing aircraft in that as the wings deflect up, it also deflects forward. For the gust deflection of 33.81 inches the wing tips deflected 8.51 inches in the negative x direction.

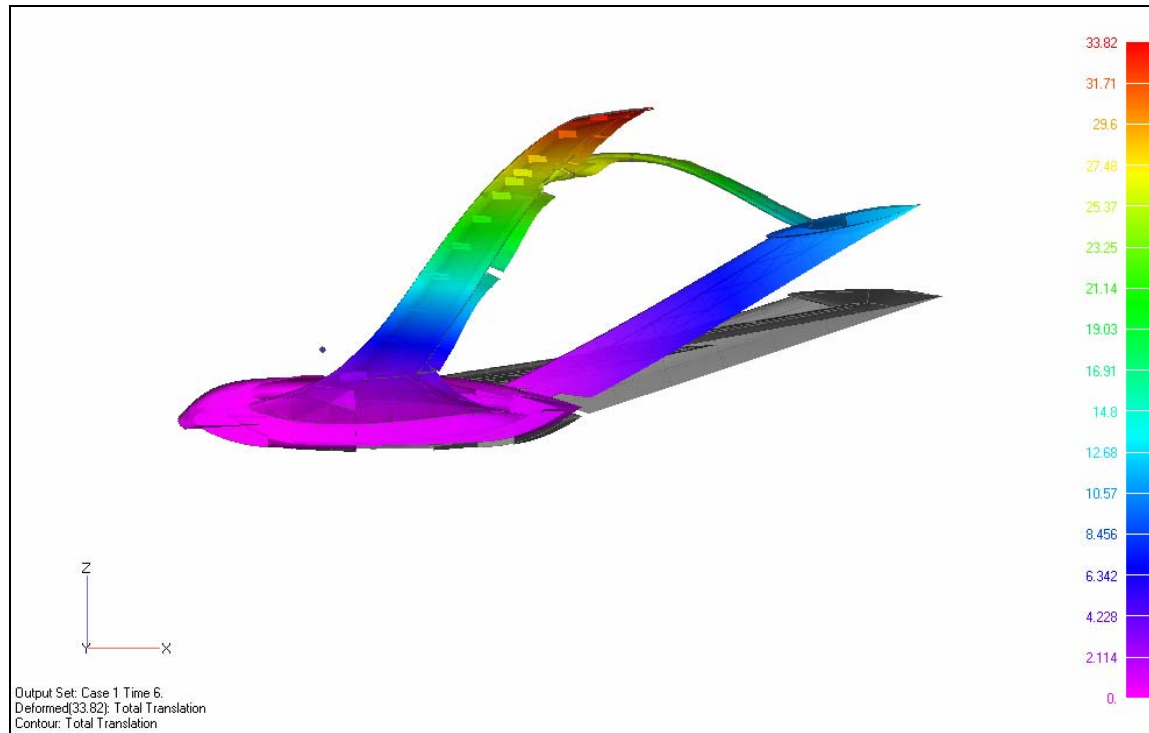


Figure 37: Profile View of Peak Gust Deflection

Figure 38 displays the Zaero output for the wingtip acceleration time history for the 2.50 second gust length and the time points for nonlinear static analysis with the respective time dependant forces. The circled stars are the points used for the analysis technique comparison. The acceleration time history plots were exactly the same for each iteration of the 2.50 second gust analysis even after updating the panels. The significance of examining this graph is that incorrect conclusions can be drawn.

First, the acceleration time history graph shows the first positive acceleration to be roughly 70.0 inches/second² greater than the second positive peak, such that the wings positive deflection should be dampening out. This is not the case as the deflection following the second positive peak is greater than the first.

The acceleration time history graph does however provide much more accurate information concerning the wingtip deflection over time. The maximum positive deflections should occur when the acceleration crosses the x-axis after a positive peak, additionally the maximum negative deflection should occur when the acceleration crosses the x-axis after a negative peak. These conclusions are both correct.

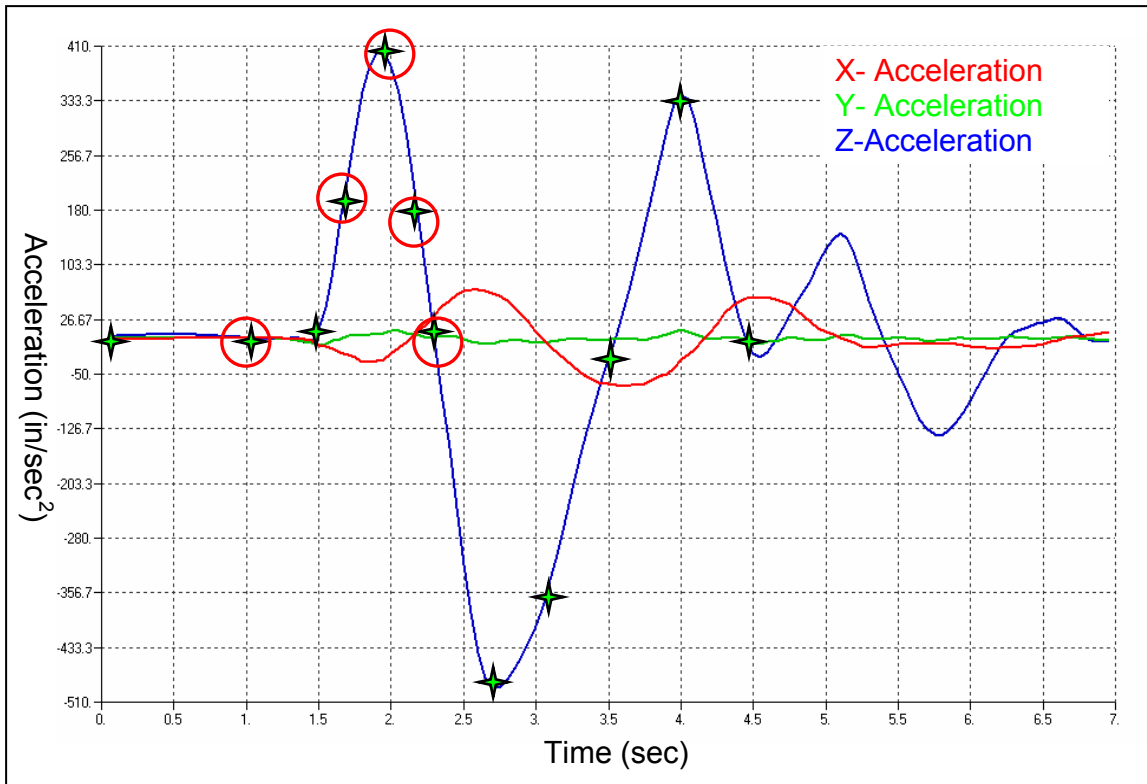


Figure 38: Wingtip Acceleration Time History for 2.50 Second Gust

The displacement time history outputted from Zaero does not provide accurate results and relying on this can lead to several incorrect conclusions. First, it shows the maximum wingtip displacement occurring at 2.7 seconds, this incorrect. Furthermore the graph shows the deflections to all be positive until approximately 3.8 seconds and then remains negative. Both of these conclusions are wrong.

The results from several MSC.Nastran nonlinear analyses for the resulting displacement from the loads applied at the respective time increments are listed in Table 21. One important point to note is that the maximum deflection occurs well after the gust has subsided; this further confirms that the nonlinear effects are insignificant.

Table 21: Actual Displacement Time History

Actual Displacement Time History	
Time (sec)	Wingtip Displacement (in)
0.0	16.42
1.0	18.13
1.5	19.15
1.7	23.31
1.9	28.72
2.1	32.77
2.3	33.80
2.7	23.24
3.1	2.09
3.5	-10.68
4.0	19.15
4.5	34.60

Figure 39 shows the deformed shapes of the SensorCraft at the 2.3, 3.1, 3.5 and 4.5 second respectively. These figures illustrate the maximum deformation occurs at 4.5 seconds (well after the gust has passed). Another aspect worth noting is the drastic translation that the boom experiences. At 3.50 seconds the SensorCraft experiences the largest negative deformation during the 2.50 second gust. At the lowest peak the most aft tip of the boom translates -10.38 inches in the vertical direction, and at 4.50 seconds the boom translates 29.99 inches. This 40.0 inch deformation is substantial, especially for the current design and should be considered because this pitching motion could be prone to fatigue failure.

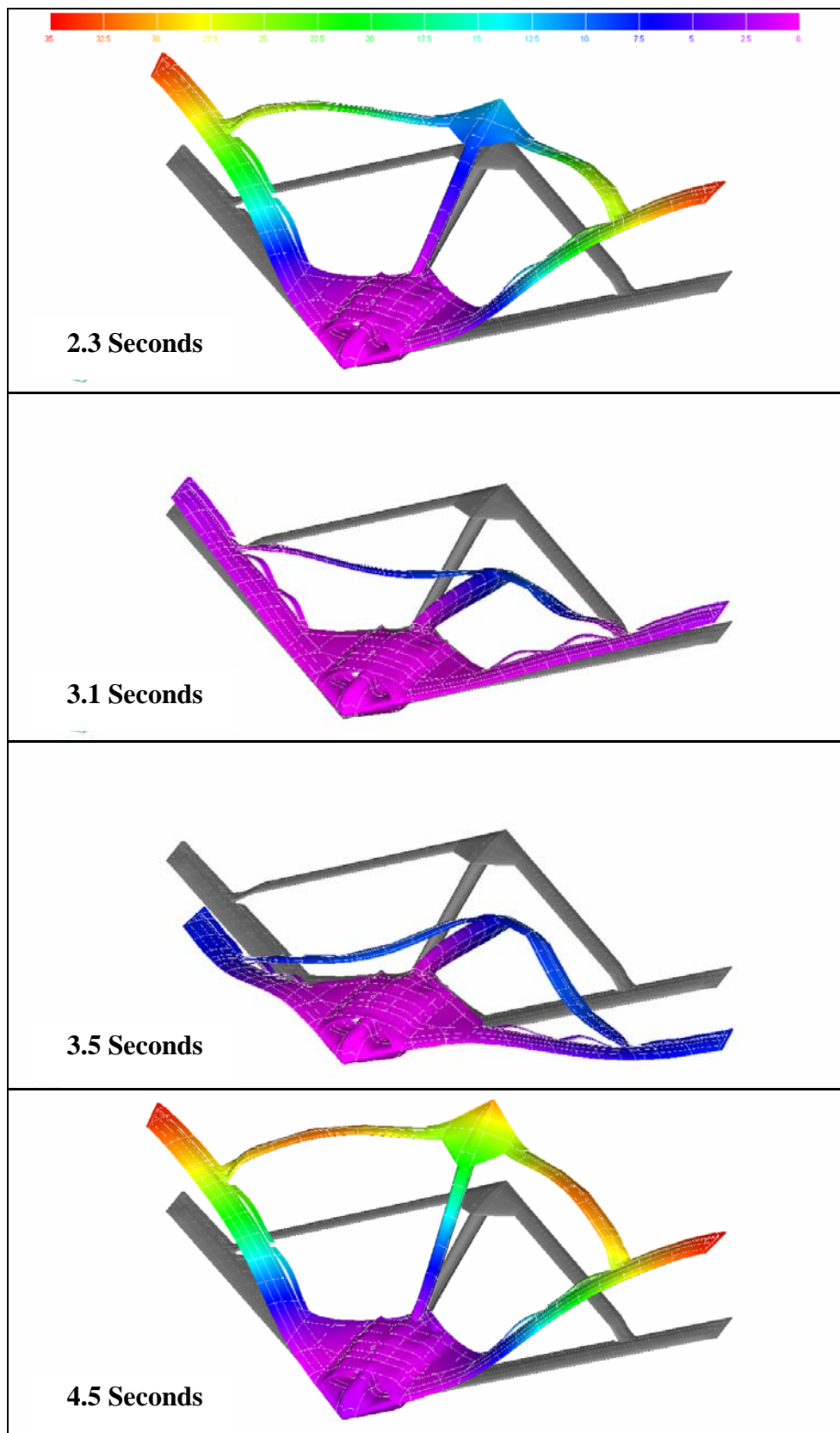


Figure 39: Time History Deformation for 2.50 Second Gust

Following these findings the time history displacement for the 3.75 second gust was also computed. The results for the 3.75 second gust were insightful. The 3.75 second gust as it produced an almost equivalent displacement as the 2.50 second gust. This was interesting considering the maximum acceleration for the 2.50 second gust was twice that of the 3.75 second gust. Considering these results, the significance of the length of the gust becomes apparent. The difference in time that the SensorCraft was exposed to the positive acceleration of the gust is approximately 0.4 seconds. Figure 40 shows the acceleration time history for the 3.75 second gust with the duration of positive acceleration marked by the gold bars.

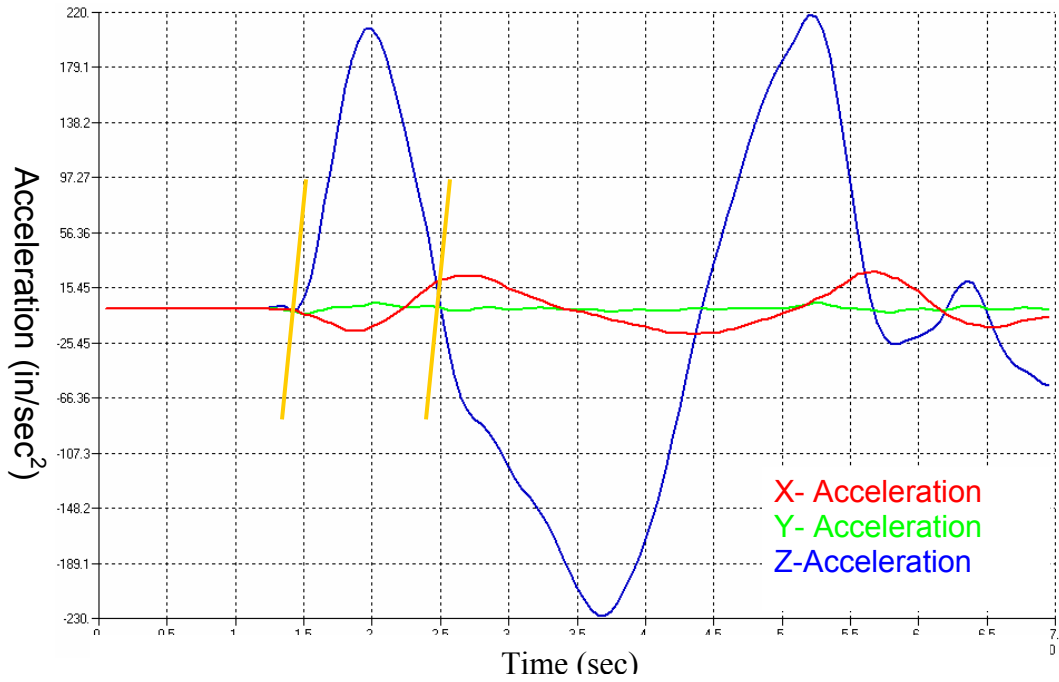


Figure 40: Wingtip Acceleration Time History for 3.75 Second Gust

A 4g pull-up maneuver was also run in order to compare the follower force effects for a trim condition with larger wing displacements, roughly 7.0 feet at the wingtips. It was found that the 4g trim analysis only resulted in a 0.86 larger wingtip displacement when compared with four times the 1g trim case. Figure 41 shows the original

aerodynamic panel model as well as the deformed panel model for trimmed 1g steady-level flight and a 4g pull-up maneuver. From this figure it can bee seen that most of the deformation is in the aft wing and that the direction normal to the forward wings does not change significantly. Two possible explanations for this deformation are the stiffness of the model as well as the geometric properties of the connection region. From Figure 41 the canted region appears to experience significant bending, (red circle). This bending of the aft wing connecting to the forward wings imparts a moment that resists upward bending of the forward wing. The end result is that because the direction normal to the forward does not change significantly, the lift loads required to trim the aircraft do not deviate significantly from a linearly approximation.

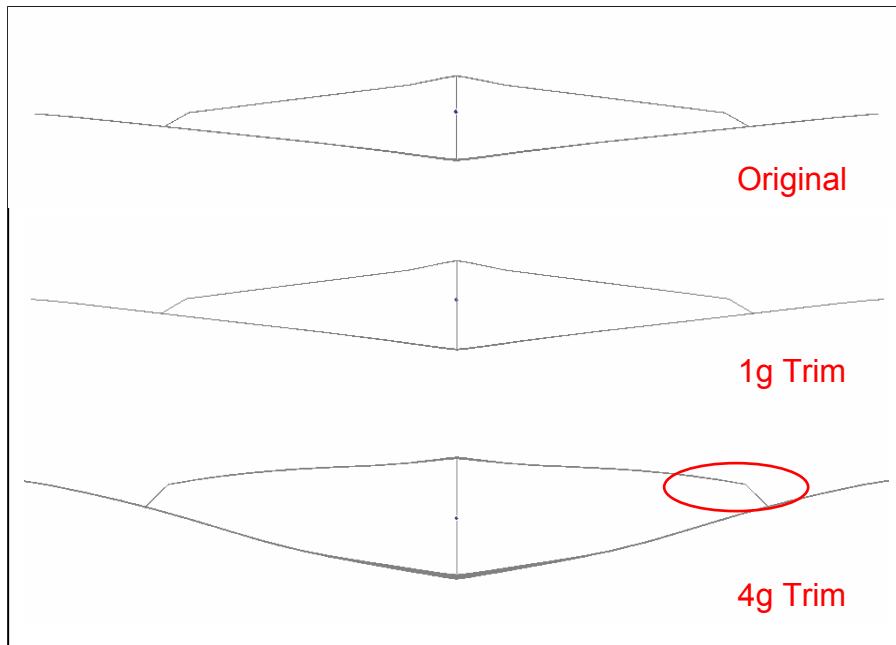


Figure 41: Aerodynamic Panel Model Comparison

V. Conclusions and Recommendations

Boeing Joined-Wing SensorCraft

The current joined wing design was structurally designed by Boeing using over 140 linear static maneuver and gust load conditions [14]. Nevertheless, the current design has not been extensively weight optimized. Thus, it is an idealistically stiff structure. Considering these details, several of the results are not surprising.

This thesis found that global buckling was not a critical condition; if the model is optimized further, buckling of the aft wing may become a critical parameter. Additionally, because the aft wing is offset in the x and z direction, a vertical applied load results in an upward and forward translation. This forward bending is associated with the canted bending plane of joined-wing aircraft, and was seen in this thesis (Figure 37). By joining the forward and aft wings of the SensorCraft, bending and torsion in the forward wing is resisted by axial stiffness of the aft wing and vice versa. This further advocates the critical loading condition as the upward gust, because by displacing the forward wings up and forward, axial compression are induced in the elevated aft wing. This creates a buckling critical condition through axial compression.

It was also found that modifying the buckled panels to prevent panel buckling effects the load factor associated with the global buckling mode even if the section where the global buckling occurs has not been altered.

The results from the modal analysis varied greatly depending on whether the model was constrained or free. Several unique differences are worth noting. First, the

first flexible mode for the clamped case occurs at 0.4Hz while the first flexible for the free case occurs at 0.7Hz. The symmetry of the first six flexible modes is exactly reversed for the two analyses and the order and character of the modes is drastically affected by clamping the model.

Aerodynamic and Structural Coupling

This thesis performed a multidisciplinary design approach with regards to joined-wing aircraft in an attempt to determine the significance of incorporating nonlinear effects. The coupled relationship between the aerodynamic forces and the deformation of the wings was found to be insignificant. That is, as the wings deform accounting for the direction change of the aerodynamic lift to maintain a direction of action normal to the deformed surface was not important. Theoretically, this change in direction requires more lift to be generated due to the developed horizontal component of lift, which should result in a larger deformation. However, because the deformations were not substantial the change in direction of the lift vector was not significant. This was true for both the gust and trim analyses. The results from accounting for nonlinear geometric effects resulted in a slightly larger difference in deformations than the linear analysis. Because the differences were so small no definite conclusions can be drawn concerning the stiffening effect of the nonlinear deformations. For the current design, accounting for the geometric nonlinearities is more influential than the follower force effects. However, should a further optimized design result in larger deformations accounting for the follower force effects may prove to be more important, particularly for the trim condition which will require a larger trim load.

Structural Aeroelastic Analysis Transient Response

The critical gust case for a 1.25 second gust did not result in the SensorCraft reacting during the gust, thus it could not be used to accurately determine the nonlinear follower force effects on the SensorCraft. This coincides with the critical loading condition of 100% fuel, in that the inertia effect is more critical than the aerodynamic loading, for the current design. Though the gust loading condition produced the largest deflection from Boeings loading conditions, this deflection was not a direct result of the aerodynamic flight loads, but was due to the momentum of the structure.

For the 5.00 second gust length the magnitude of deflection that resulted from the gust was unsubstantial, approximately five inches. Thus it was considered too small of a deformation to characterize the follower force effects and was not used as the gust length to account for follower forces.

Both the 2.50 and 3.75 second gust lengths produced the initial peak deflection during the gust. However, in both cases the largest deflection occurred after the gust had subsided, which can be attributed to the inertial forces. From these results, it is apparent that the dynamic effects of the gust are far more substantial than the aerodynamic effects. Furthermore, with the current stiffness of the design, a quasi-steady state with substantial deflection for incorporating the follower force effects cannot be achieved.

Both the maximum acceleration and the duration of gust influence have an effect in developing a state of maximum deflection.

Recommendations

Further study should first include structural and weight optimization to ensure that the rigidity currently associated with the SensorCraft is realistic of future designs. Following this a multi-disciplinary design approach should be exercised accounting for both geometric and aeroelastic nonlinearities.

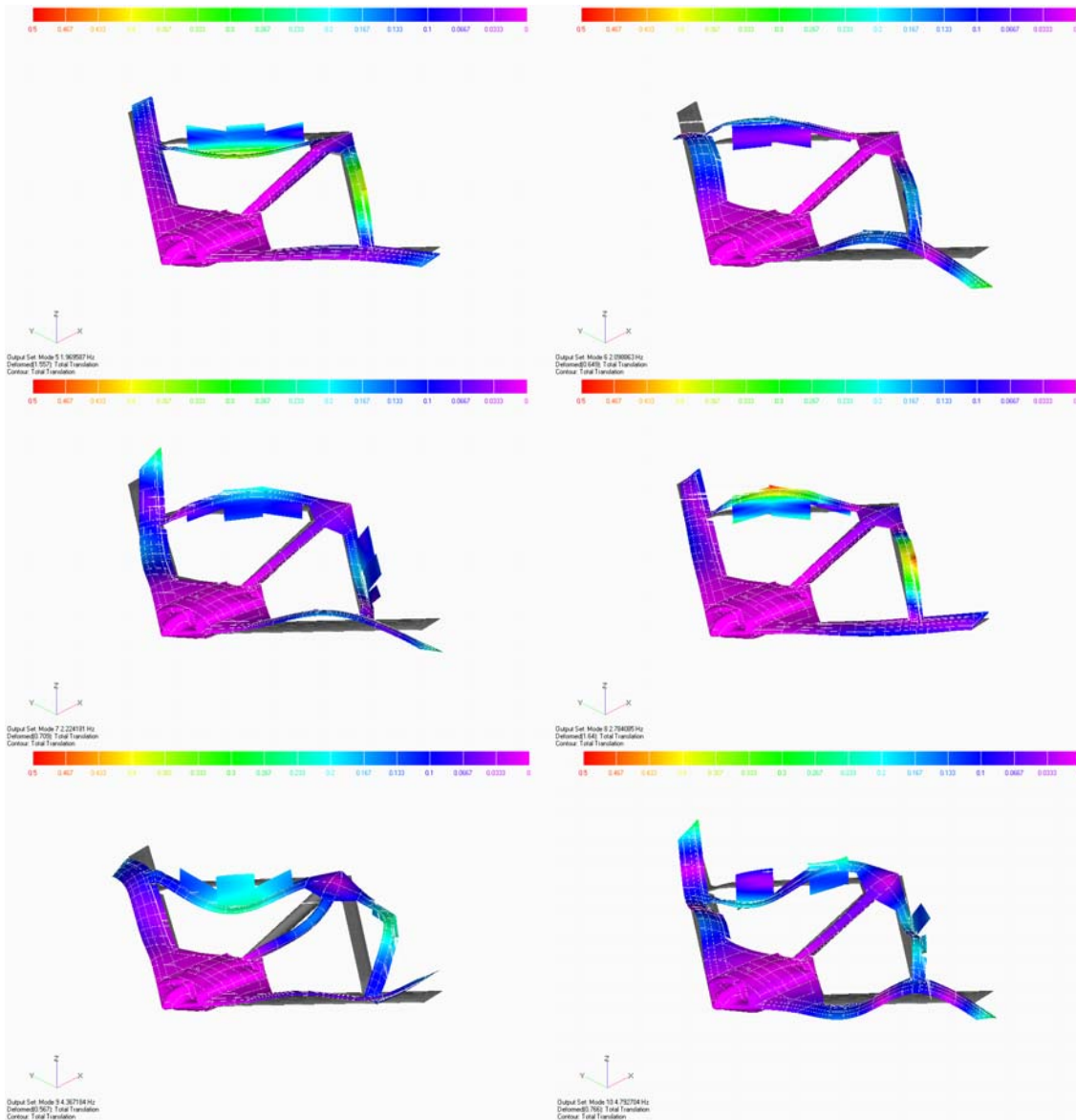
Both the pitch and plunge mode should be included as only the pitch mode was included in this thesis.

Closer examination should be done on the selection of the reduced frequencies and the length of the gust. Both parameters affect the solutions of the trim and gust analyses.

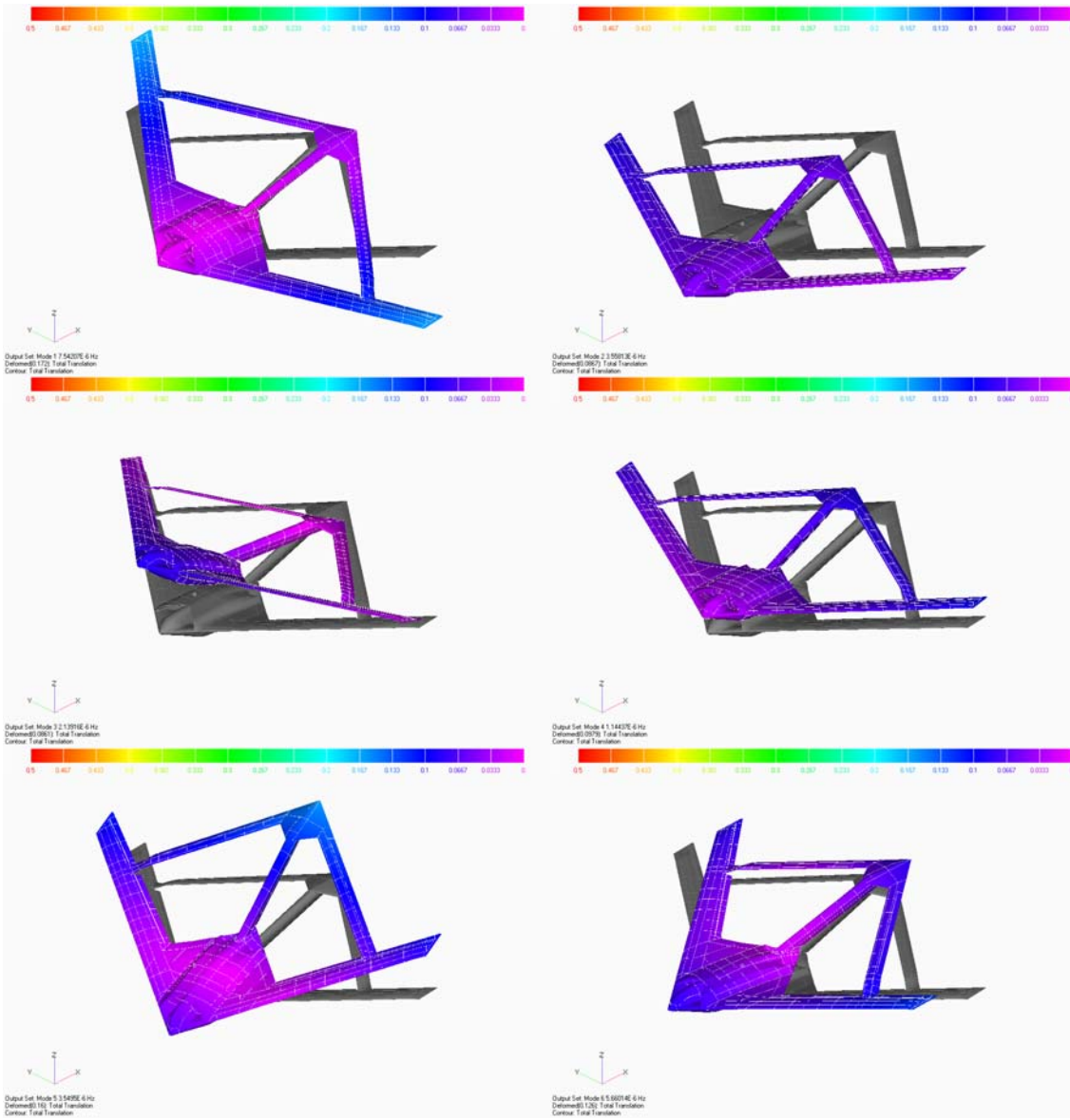
The dynamic effects should be examined to fully characterize the effects of flight loads, as the effect of the gust appears to be acting more as an impulse than as a quasi-steady flight load.

Appendix A

Modes 5-10 for the Clamped Normal Modes Analysis



Modes 1-6 for Free-Free Normal Modes Analysis



Appendix B

Zaero 1G Trim Input

```
$*****
$EXECUTIVE CONTROL SECTION
$*****
MEMORY 1024MB

$ ASSIGN *.f06 & *.mgh FILES FROM NASTRAN MODAL ANALYSIS
ASSIGN FEM=spline_fuel_nm.f06, FORM=MSC, BOUND=ASYM
ASSIGN MATRIX=spline_fuel_mgh.dat,FORM=FORMAT,MNAME=SMGH, SUPORT=123456/48056

CEND

$*****
$Case Control Section
$*****
TITLE= SENSORCRAFT
ECHO = SORT
SUBCASE = 1
    SUBTITLE=SENSORCRAFT PRE-GUST TRIM
    LABEL=M=0.255, ALTITUDE=Sea Level
    TRIM=100

$*****
$BULK DATA SECTION
$*****
BEGIN BULK

$ INCLUDE FILES GENERATED BY CAERONODES.m AND AERO.m
INCLUDE './Include/CAERO7.dat'
INCLUDE './Include/SPLINE.dat'
INCLUDE './Include/CAEROCAMBER_FW.dat'
INCLUDE './Include/CAEROCAMBER_AW.dat'
INCLUDE './Include/CAEROCAMBER_FUSE.dat'
INCLUDE './Include/CAEROCAMBER_TAIL.dat'
INCLUDE './Include/CAEROCAMBER_nCHORD.dat'
INCLUDE './Include/fw_ELEMENT_SPACING.dat'
INCLUDE './Include/CONTROL_SURFACES.dat'

$ INCLUDE SET DATA
INCLUDE './Include/SET_DATA.dat'

$ UNSTEADY AERODYNAMICS GENERATOR - SAVE FIRST TIME, ACQUIRE AFTER
$...1..><...2..><...3..><...4..><...5..><...6..><...7..><...8..><...9..><..10..>
MKAEROZ   37      0.255      0     2001      SAVE      TRIM1.AIC      1      +MK1A
$MKAEROZ   37      0.255      0     2001      ACQUIRE    TRIM1.AIC      1      +MK1A
+MK1A      0.025

$ MEAN FLOW CONDITION SPECIFICATION
$...1..><...2..><...3..><...4..><...5..><...6..><...7..><...8..><...9..><..10..>
TRIMFLT   2001      100      0.0      0.0      0.0      0.0      0.0      0

$ TRIM PARAMETERS
$...1..><...2..><...3..><...4..><...5..><...6..><...7..><...8..><...9..><..10..>
TRIM      100      37      0.67      0      0 219.203      0.0      -65.564      +T1
+T1      0.0025881.456+051.259+101.070+057.683+091.460+097.047+051.950+10      +T2
+T2      G      NONE      NONE      1.0      NONE      NONE      NONE      +T3
```

```

+T3          101      0.0      102      0.0      103      0.0      104      0.0      +T4
+T4          105      0.0      106      0.0      1       FREE      2       1.0

$ TRIM VARIABLES
$...1..><...2..><...3..><...4..><...5..><...6..><...7..><...8..><...9..><..10..>
TRIMVAR      101    LFW_F1
TRIMVAR      102    LFW_F2
TRIMVAR      103    LFW_F3
TRIMVAR      104    RFW_F1
TRIMVAR      105    RFW_F2
TRIMVAR      106    RFW_F3
TRIMVAR      1     ALPHA
TRIMVAR      2     THKCAM

$ CENTER OF GRAVITY DEFINITION
$...1..><...2..><...3..><...4..><...5..><...6..><...7..><...8..><...9..><..10..>
CORD2R   200           219.203 0.        -65.564 219.203 0.        34.436
          319.203 0.        -65.564

$ REFERENCE PARAMETERS
$...1..><...2..><...3..><...4..><...5..><...6..><...7..><...8..><...9..><..10..>
AEROZ      NO      NO      SLIN      IN      142.53  1798.  246187.  +AE1
+AE1      0.      0.      0.

$ OUTPUT PLOTTING AND FORCE OPTIONS
$...1..><...2..><...3..><...4..><...5..><...6..><...7..><...8..><...9..><..10..>
PLTTRIM   235    100FLEX    ELASTIC tecplot aSLm225EL.PLT
PLTTRIM   236    100FLEX    CP      tecplot aSLm225CP.PLT
PLTTRIM   237    100FLEX    FORCE   NASTRAN FLEX.FRC
PLTTRIM   238    100FLEX    DEFORM  NASTRAN DEFORMF.BDF
PLTTRIM   239    100RIGID   FORCE   NASTRAN RIGID.FRC
PLTTRIM   240    100RIGID   DEFORM  NASTRAN DEFORMR.BDF
PLTAERO    34YES              tecplot geo.plt             YES

ENDDATA

```

Zaero 2.50 Second Discrete Gust Input

```

*****
$EXECUTIVE CONTROL SECTION
*****
MEMORY 1024MB

$ ASSIGN *.f06 & *.mgh FILES FROM NASTRAN MODAL ANALYSIS
ASSIGN FEM=spline_fuel_nm.f06, FORM=MSC, BOUND=ASYM ,suport=123456/48056
ASSIGN MATRIX=spline_fuel_mgh.dat,FORM=FORMAT,MNAME=SMGH
DIAG 1,3
GenGUST
CEND

*****
$Case Control Section
*****
TITLE= SENSORCRAFT
ECHO = SORT
SUBCASE=1
SUBTITLE=DISCRETE GUST ANALYSIS
LABEL=M=0.255, ALTITUDE=Sea Level, NO CONTROLS, 100%
GLOADS=44

*****
$BULK DATA SECTION
*****
BEGIN BULK
$
```

```

$      SET OF NORMAL MODES TO BE EXCLUDED FROM ANALYSIS
SET1,4,1,2,3,4,8,9,12,+SE
+SE,14,15,16,18,21,24,26,27,+SR
+SR,29,31,33,35,37,38,39,41,+SU
+SU,43
$
$GUST ANALYSIS
$

$Discrete Gust
$...1..><...2..><...3..><...4..><...5..><...6..><...7..><...8..><...9..><..10..>
GENGUST 10          37           ASYM     1
GLOADS   44          35            345      48       40      49

$      MODES DESCRIPTION AND SETUP
$...1..><...2..><...3..><...4..><...5..><...6..><...7..><...8..><...9..><..10..>
FLUTTER 35          ASYM     36          0          4

$      MACH AND ALTITUDE DESCRIPTION
$...1..><...2..><...3..><...4..><...5..><...6..><...7..><...8..><...9..><..10..>
FIXMACH 36          37           SLIN     IN        1.0          +FIX1
+FIX1    3416.18 1.1456-7

$      GUST PROFILE
$...1..><...2..><...3..><...4..><...5..><...6..><...7..><...8..><...9..><..10..>
DGUST   48          OMCOS   2.50        0.2178 -4270.0 0.0       0.01

$      AIRFRAME INITIAL STATE DESCRIPTIONS
$...1..><...2..><...3..><...4..><...5..><...6..><...7..><...8..><...9..><..10..>
MLDSTAT 345         346           YES      ABMATRIX.DAT          +MS1
+MS1    ALPHA   0.05     Q        0.0       H        0.0       THETA   0.0

$      TRIM CONDITIONS SPECIFICATIONS
$...1..><...2..><...3..><...4..><...5..><...6..><...7..><...8..><...9..><..10..>
MLDTRIM 346         386.4      1.0       YES      SMODAL          +ty
+ty     ALPHA   0.05

$      ANALYSIS START, STOP AND STEP
$...1..><...2..><...3..><...4..><...5..><...6..><...7..><...8..><...9..><..10..>
MLDTIME 40          -1.25     7.0       0.05     1          0

$      NORMAL MODES GRIDPOINT AND CONSTRAINED DEGREES OF FREEDOM
$...1..><...2..><...3..><...4..><...5..><...6..><...7..><...8..><...9..><..10..>
RBRED    7           44          123456  48056

$ UNSTEADY AERODYNAMICS GENERATOR - SAVE FIRST TIME
$                                - ACQUIRE IF PANEL MODEL IS UNCHANGED
$...1..><...2..><...3..><...4..><...5..><...6..><...7..><...8..><...9..><..10..>
MKAEROZ 37          0.255     0          2001     SAVE     LG250_4.AIC     1          +MK1A
$MKAEROZ 37          0.255     0          2001     ACQUIRE LG250_4.AIC     1          +MK1A
+MK1A    0.025     0.05     0.1        1.25

$      INCLUDE FILES GENERATED BY CAERONODES.m AND AERO.m
INCLUDE './Include/CAERO7.dat'
INCLUDE './Include/SPLINE.dat'
INCLUDE './Include/CAEROCAMBER_FW.dat'
INCLUDE './Include/CAEROCAMBER_AW.dat'
INCLUDE './Include/CAEROCAMBER_FUSE.dat'
INCLUDE './Include/CAEROCAMBER_TAIL.dat'
INCLUDE './Include/CAEROCAMBER_nCHORD.dat'
INCLUDE './Include/FW_ELEMENT_SPACING.dat'
INCLUDE './Include/CONTROL_SURFACES.dat'

$      INCLUDE SET DATA
INCLUDE './Include/SET_DATA.dat'

$      MEAN FLOW CONDITION SPECIFICATION
$...1..><...2..><...3..><...4..><...5..><...6..><...7..><...8..><...9..><..10..>
TRIMFLT 2001        2.84      0.0       0.0       0.0       0.0       0

$      TRANSFORMATION MATRIX FROM RIGID BODY MODES TO TRIM CONDITION

```

```

$ TAKEN FROM TRIM OUTPUT FILE
DMI SMODAL 0 2 2 DMIIL 45 1
DMIIL SMODAL 1 1+0.000000000E+00+CONT
+CONT +0.000000000E+00+0.000000000E+00+0.000000000E+00+0.000000000E+00+CONT
+CONT +0.000000000E+00+1.658970337E+02-1.353379369E+00+1.238984093E-01+CONT
+CONT -1.183559132E+01+3.395289183E+00-1.117188811E+00+1.589464951E+01+CONT
+CONT -2.892262936E-01+5.918559432E-02-3.727143764E+00+2.215440385E-03+CONT
+CONT -2.367524624E+00-2.070861310E-01+9.406891768E-04-3.360095434E-03+CONT
+CONT +2.851896584E-01+4.519606475E-03-1.977201998E-01+1.385760261E-03+CONT
+CONT +1.648741402E-02+5.179491043E-01+1.662941463E-02-1.927973353E-03+CONT
+CONT +2.285429239E-01+6.351803988E-02-8.731965208E-04-7.315892726E-04+CONT
+CONT -6.046441849E-03+2.378871141E-04-1.343427412E-02-6.330224569E-04+CONT
+CONT -7.402034476E-03-2.409760054E-04+4.476973321E-03+3.766996088E-04+CONT
+CONT -3.055174462E-02+2.058909042E-03+3.277070820E-01+5.534183001E-04

$ REFERENCE PARAMETERS
$...1..><...2..><...3..><...4..><...5..><...6..><...7..><...8..><...9..><..10..>
AEROZ NO NO SLIN IN 142.53 1798. 246187. +AE1
+AE1 0. 0. 0.

$ OUTPUT PLOTTING AND FORCE OPTIONS

$ FORCE
$...1..><...2..><...3..><...4..><...5..><...6..><...7..><...8..><...9..><..10..>
PLTTIME 50 44 0.0 3.5 2 FORCESOFNASTRAN +P
+P LG250_4.BDF

$ DISPLACEMENT WING
MLDPRNT 49 DISPW.NEU FEMAP +M1
+M1 GRIDXT3 35 GRIDXT2 35 GRIDXT1 35
$ ACCELERATION WING
MLDPRNT 49 ACCEW.NEU FEMAP +M1
+M1 GRIDGT3 35 GRIDGT2 35 GRIDGT1 35

$...1..><...2..><...3..><...4..><...5..><...6..><...7..><...8..><...9..><..10..>
$44863 & 47458 ARE OFFSET ON THE Y AXIS BY 32 INCHES IN OPPOSITE DIRECTIONS,

$ ACCELERATION BODY
MLDPRNT 49 ACCEC.NEU FEMAP +M11
+M11 GRIDGT3 44863 GRIDGT2 44863 GRIDGT1 44863
$ DISPLACEMENT BODY
MLDPRNT 49 DISPC.NEU FEMAP +M11
+M11 GRIDXT3 44863 GRIDXT2 44863 GRIDXT1 44863

$ ACCELERATION BODY
MLDPRNT 49 ACCEC.NEU FEMAP +M11
+M11 GRIDGT3 47458 GRIDGT2 47458 GRIDGT1 47458
$ DISPLACEMENT BODY
MLDPRNT 49 DISPC.NEU FEMAP +M11
+M11 GRIDXT3 47458 GRIDXT2 47458 GRIDXT1 47458

ENDDATA

```

Nastran Nonlinear Initial Input

```

$ NASTRAN input file created by the MSC MSC.Nastran input file
$ BRANDON ADAMS NONLINEAR 1
$
$
ASSIGN MASTER='SCNLff250.MASTER'
INIT MASTER(RAM) LOGICAL=(MASTER(9999999))
ASSIGN DBALL='SCNLff250.DBALL'
INIT DBALL LOGICAL=(DBALL(9999999))
$
$
$ Nonlinear Static Analysis

```

```

SOL 106
CEND

$*****
$      EXECUTIVE CONTROL SECTION      *
$*****
$SEALL = ALL
$SUPER = ALL
TITLE = SENSORCRAFT NONLINEAR ANALYSIS
ECHO = NONE
NLPARM = 1
SPC = 2
DISPLACEMENT(PRINT)=ALL

$*****
$          SUBCASE DEFINITONS      *
$*****
SUBCASE 1
  SUBTITLE=Time_0.0
  LOAD = 44

$*****
$          BULK DATA SECTION      *
$*****
$BEGIN BULK
$PARAM    POST      0
PARAM    AUTOSPC NO
PARAM*   WTMASS      .002588
PARAM    LGDISP     1
PARAM    PRTMAXIM YES
$ITERTECHNIQUES *
$*****
$NEWTON-RAPHSON METHOD
NLPARM   1       10      ITER    1      25      UPW      NO
        .1       .1      .1

$MODIFIED NEWTONS METHOD
NLPARM   3       5      ITER    50      50      UPW      NO
        .1       .1      .1

$$
$FUEL MASS
$*****
$include './LOAD_CASES/Fuel_Mass.FRC'
$GUST LOADS
$*****
$include './LOAD_CASES/LG250_1.FRC'
$SensorCraft
$*****


$ Elements and Element Properties for region : Body.BL032.chord.lwr.beam
PBAR    2       1      2.96    9.806   1.65      .1
$ Pset: "Body.BL032.chord.lwr.beam" will be imported as: "pbar.2"
CBAR    35824   2      48255   48251     0.      1.      0.
CBAR    35825   2      48251   48249     0.      1.      0.
CBAR    35826   2      48249   48247     0.      1.      0.
CBAR    35827   2      48247   48244     0.      1.      0.

.....

```

Nastran Restarted Gust Input

```
$ NASTRAN input file created by the MSC MSC.Nastran input file
$      BRANDON ADAMS NONLINEAR 1
$ 
$ 
$ Direct Text Input for File Management Section
ASSIGN MASTER='SCNLff250.MASTER'
RESTART VERSION=LAST,NOKEEP
$ Nonlinear Static Analysis
SOL 106
CEND
$*****
$      EXECUTIVE CONTROL SECTION      *
$*****
```



```
SEALL = ALL
SUPER = ALL
TITLE = SENSORCRAFT NONLINEAR ANALYSIS
ECHO = NONE
NLPARM = 1
SPC = 2
DISPLACEMENT(PRINT)=ALL
$*****
$      PARAMETERS FOR RESTART      *
$*****
```



```
PARAM,LOOPID,10
PARAM,SUBID,2

$*****
$      SUBCASE DEFINITONS      *
$*****
```



```
SUBCASE 1
    SUBTITLE=Trim_0.0
    LOAD = 44

SUBCASE 2
    SUBTITLE=Trim_0.0
    LOAD = 54

$*****
$      BULK DATA SECTION      *
$*****
```



```
$ 
BEGIN BULK
$ 
$      ONLY NEW CARDS ARE NEEDED FOR RESTART

$*****
$      INSERT UNIQUE LOAD CASE      *
$*****
```



```
$$$$$$$$$$ AT TIME= 0.10000E+01, LOAD SET = 54 $$$$$$$$$
$ 
FORCE      54      1      0-1.33+00  1.000   0.000   0.000
FORCE      54      1      0-1.56+00  0.000   1.000   0.000
FORCE      54      1      0-1.23+01  0.000   0.000   1.000
```

Appendix C

Other Material around Radar Arrays

Material 1

```
Type ISOTROPIC      Color 55      Layer 1      #Prop 95
      Density 0.00014493   Damping 0.          Ref Temp 0.
STIFFNESS           E 15500000.        G 2027000.    Nu 0.
STRENGTH            Tension 0.       Compress 0.   Shear 0.
THERMAL             Alpha 0.        K 0.         SpecHeat 0.
THermal             HtGen 0.
OPTICAL             Front  Off       Reverse  Off
```

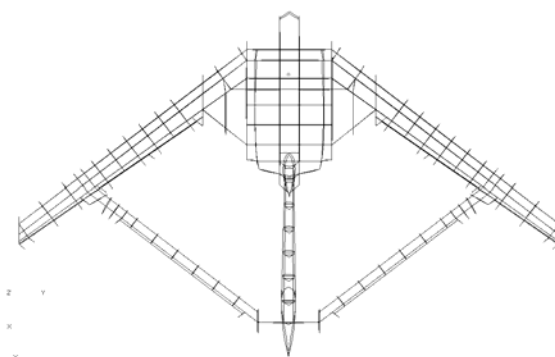


Figure 42 Use of Material 1 throughout Sensorcraft

Material 8

```
Type ISOTROPIC      Color 55      Layer 1      #Prop 1
      Density 0.          Damping 0.          Ref Temp 0.
STIFFNESS           E 16000000.        G 6153846.    Nu 0.3
STRENGTH            Tension 0.       Compress 0.   Shear 0.
THERMAL             Alpha 0.        K 0.         SpecHeat 0.
THermal             HtGen 0.
OPTICAL             Front  Off       Reverse  Off
```

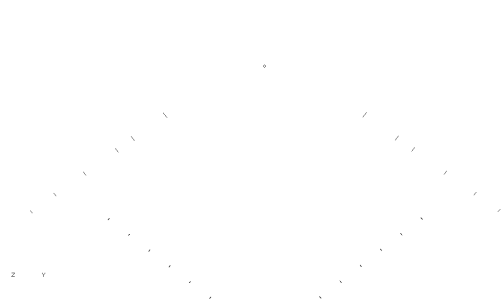


Figure 43 Use of Material 8 throughout Sensorcraft

Appendix D

Gust Load Stress Results

	Load Case	Element Title	Max Stress		Load Case	Element Title	Max Stress
1	31411	Bar EndA Axial Stress	108875.6	51	31412	Bar EndB Max Comb Stress	64472.27
2	31411	Bar EndA Max Comb Stress	108875.6	52	31412	Bar EndB Min Comb Stress	64472.27
3	31411	Bar EndA Min Comb Stress	108875.6	53	31411	Lam Ply1 MajorPrn Stress	62586.9
4	31411	Bar EndB Max Comb Stress	108875.6	54	31411	Lam Ply1 X Normal Stress	62561.9
5	31411	Bar EndB Min Comb Stress	108875.6	55	31411	PltC1 Bot X Normal Stress	62381.82
6	31411	Rod Axial Stress	75451.28	56	31411	PltC1 Top X Normal Stress	62375.36
7	31411	PltC3 Top MajorPrn Stress	75445.7	57	31411	Bar EndA Axial Stress	57257.9
8	31411	PltC3 Bot MajorPrn Stress	75443.45	58	31411	Bar EndA Max Comb Stress	57257.9
9	31411	PltC3 Top Y Normal Stress	75149.62	59	31411	Bar EndA Min Comb Stress	57257.9
10	31411	PltC3 Bot Y Normal Stress	75146.77	60	31411	Bar EndB Max Comb Stress	57257.9
11	31411	PltC2 Top MajorPrn Stress	74229.72	61	31411	Bar EndB Min Comb Stress	57257.9
12	31411	PltC2 Bot MajorPrn Stress	74228.71	62	31411	Lam1 VonMises Stress	56948.81
13	31411	Lam Ply3 MajorPrn Stress	73934.6	63	11411	Rod Axial Stress	50597.68
14	31411	PltC2 Top Y Normal Stress	73238.34	64	31421	Bar EndA Axial Stress	49087.56
15	31411	PltC2 Bot Y Normal Stress	73237	65	31421	Bar EndA Max Comb Stress	49087.56
16	31411	PltC3 Bot VonMises Stress	72794.92	66	31421	Bar EndA Min Comb Stress	49087.56
17	31411	PltC3 Top VonMises Stress	72789.48	67	31421	Bar EndB Max Comb Stress	49087.56
18	31411	PltC2 Top VonMises Stress	72780.63	68	31421	Bar EndB Min Comb Stress	49087.56
19	31411	PltC2 Bot VonMises Stress	72779.54	69	31414	Bar EndA Axial Stress	48649.04
20	31411	Lam Ply3 X Normal Stress	71898.6	70	31414	Bar EndA Max Comb Stress	48649.04
21	31411	Plate Bot MajorPrn Stress	71753.34	71	31414	Bar EndA Min Comb Stress	48649.04
22	31411	Plate Top MajorPrn Stress	71751.41	72	31414	Bar EndB Max Comb Stress	48649.04
23	31411	PltC4 Bot MajorPrn Stress	71734.41	73	31414	Bar EndB Min Comb Stress	48649.04
24	31411	PltC4 Top MajorPrn Stress	71727.84	74	31411	PltC1 Bot Mean Stress	46996.98
25	31411	PltC4 Bot Y Normal Stress	71472.62	75	11411	PltC3 Bot VonMises Stress	46267.61
26	31411	PltC4 Top Y Normal Stress	71465.74	76	11411	PltC3 Top VonMises Stress	46264.31
27	31411	Plate Bot Y Normal Stress	70952.49	77	31411	PltC4 Bot Mean Stress	46188.34
28	31411	Plate Top Y Normal Stress	70950.95	78	31411	PltC4 Top Mean Stress	46188.27
29	31411	Plate Bot VonMises Stress	69315.12	79	11411	PltC2 Top VonMises Stress	46171.47
30	31411	Plate Top VonMises Stress	69308.93	80	11411	PltC2 Bot VonMises Stress	46170.82
31	31411	PltC3 Top X Normal Stress	68868.11	81	31411	PltC3 Top Mean Stress	44247.79
32	31411	PltC3 Bot X Normal Stress	68865.77	82	31411	PltC3 Bot Mean Stress	44247.53
33	31411	PltC1 Bot MajorPrn Stress	68520.02	83	31412	PltC3 Top MajorPrn Stress	44212.7
34	31411	PltC1 Top MajorPrn Stress	68511.62	84	31412	PltC3 Bot MajorPrn Stress	44211.41
35	31411	PltC1 Bot VonMises Stress	68362.34	85	11411	PltC4 Top VonMises Stress	44205.87
36	31411	PltC1 Top VonMises Stress	68355	86	11411	PltC4 Bot VonMises Stress	44205.28
37	31411	PltC4 Bot VonMises Stress	68339.05	87	31412	Rod Axial Stress	44126.84
38	31411	PltC4 Top VonMises Stress	68326.55	88	31412	PltC3 Top Y Normal Stress	44039.75
39	31411	Lam3 VonMises Stress	68045.87	89	31412	PltC3 Bot Y Normal Stress	44038.11
40	31411	PltC1 Bot Y Normal Stress	67986.38	90	11411	Plate Bot VonMises Stress	44022.55
41	31411	PltC1 Top Y Normal Stress	67978.55	91	11411	Plate Top VonMises Stress	44018.81
42	31411	PltC4 Top X Normal Stress	67079.47	92	31411	Lam3 Mean Stress	43934.7
43	31411	PltC4 Bot X Normal Stress	67078.37	93	31412	Lam Ply3 MajorPrn Stress	43891.5
44	31411	PltC2 Bot X Normal Stress	65636.03	94	31411	Plate Bot Mean Stress	43876.5
45	31411	PltC2 Top X Normal Stress	65630.37	95	31411	Plate Top Mean Stress	43876.44
46	31411	Plate Bot X Normal Stress	65024.89	96	31411	PltC1 Top Mean Stress	43698.7
47	31411	Plate Top X Normal Stress	65023.65	97	11411	Lam3 VonMises Stress	43586.02
48	31412	Bar EndA Axial Stress	64472.27	98	11411	PltC1 Top VonMises Stress	43558.37
49	31412	Bar EndA Max Comb Stress	64472.27	99	31412	PltC2 Top MajorPrn Stress	43496.35
50	31412	Bar EndA Min Comb Stress	64472.27	100	31412	PltC2 Bot MajorPrn Stress	43495.77

Appendix E

Displacements from Static Loads

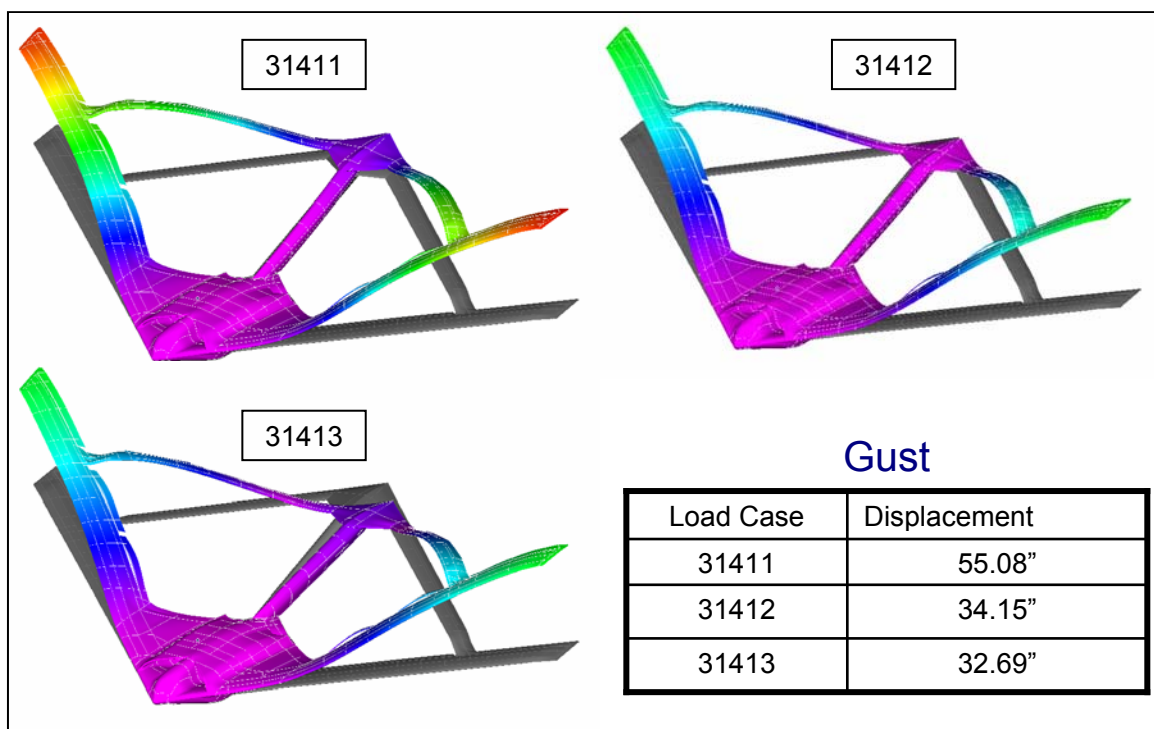


Figure 44: Gust Load Deformations & Magnitude of Maximum Displacement

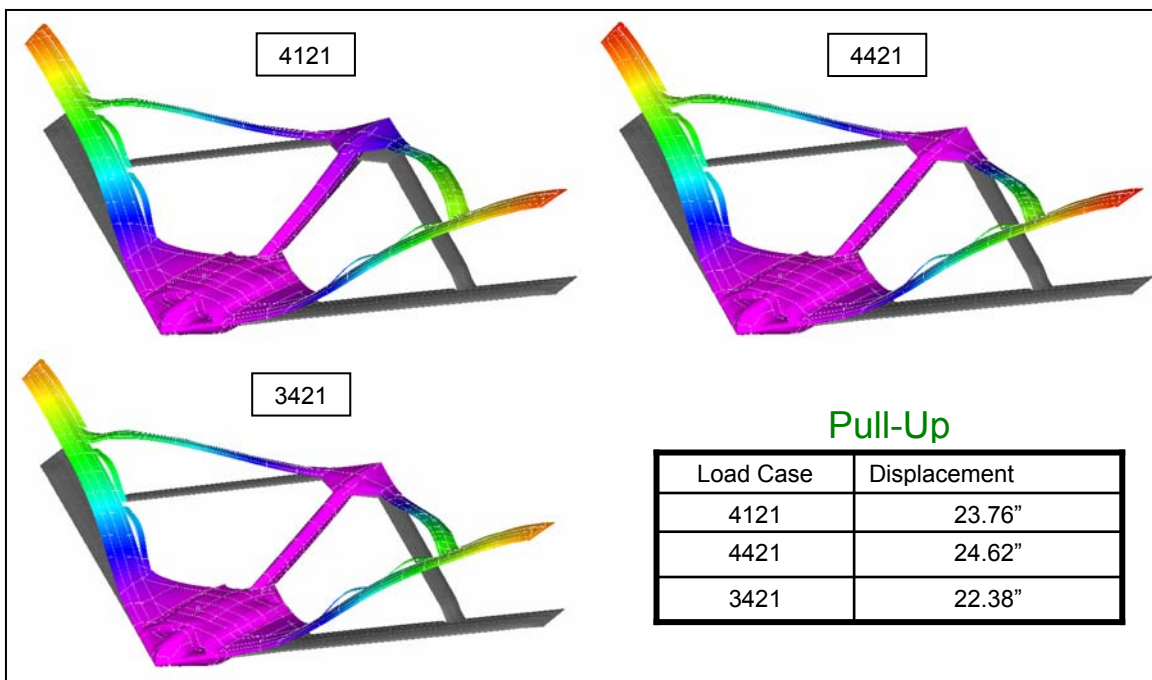


Figure 45: Pull-Up Load Deformations & Magnitude of Maximum Displacement

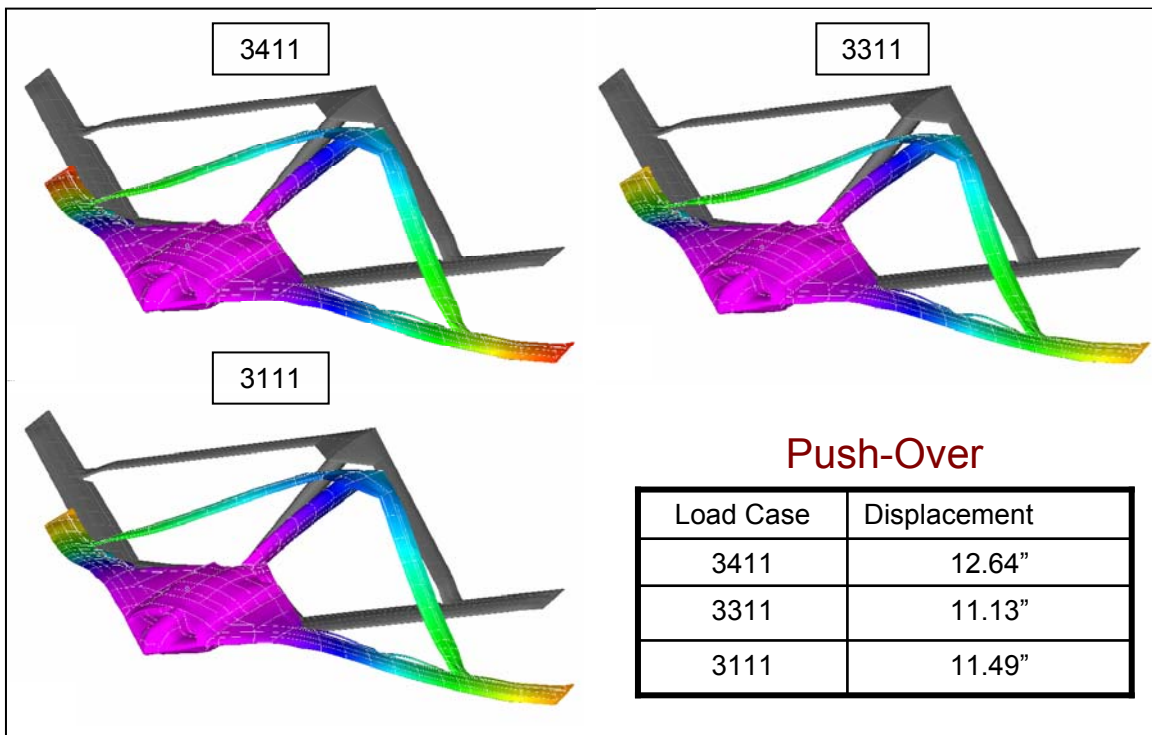


Figure 46: Push-Over Load Deformations & Magnitude of Maximum Displacement

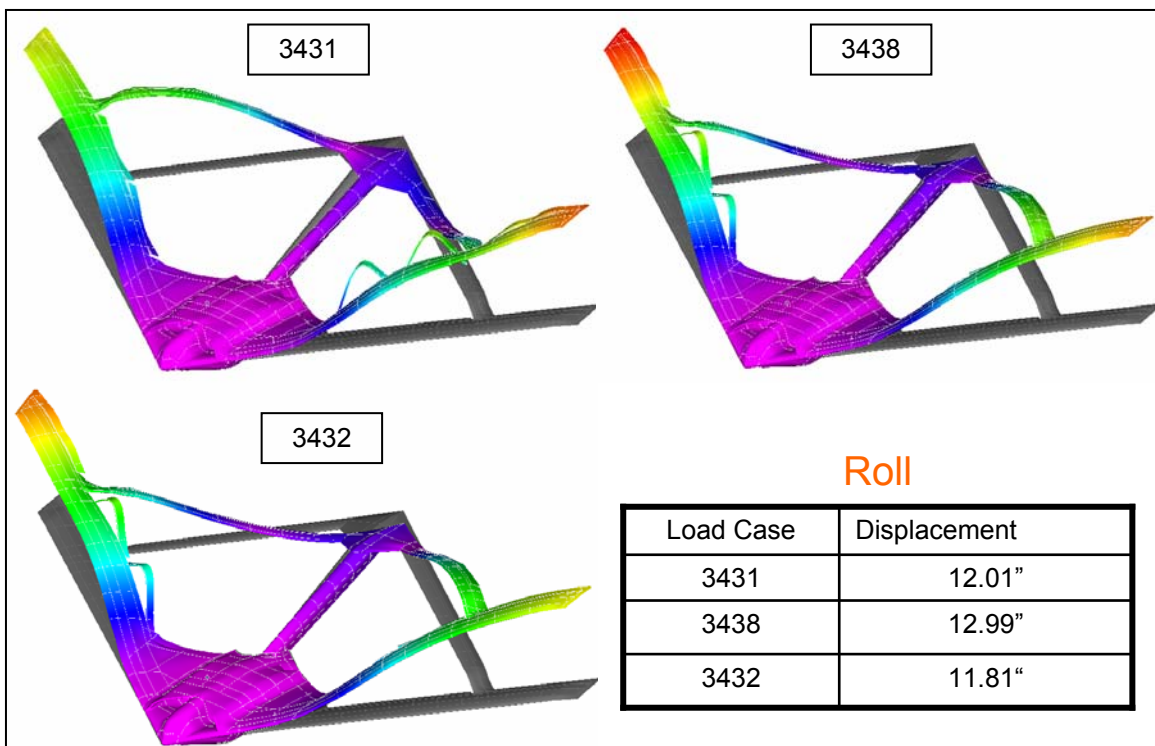


Figure 47: Roll Load Deformations & Magnitude of Maximum Displacement

Bibliography

1. "MSC.Nastran Primer for Linear Analysis 2nd Edition", MSC.Software Corporation, 2001.
2. "MSC.Nastran Getting Started User's Guide 2nd Edition", The MacNeal-Schwendler Corporation, 1996.
3. Wolkovich, J., "The Joined Wing: An Overview," *Journal of Aircraft*, Vol. 23, No. 3, 1986, pp. 161-178.
4. Blair, M., and Canfield, R., "A Joined-Wing Structural Weight Modeling Study", AIAA-2002-1337, presented at the 43rd AIAA/ASME/ASCE/AHS/ASC Structures, Structural Dynamics and Materials Conference, Denver, CO, 22-25 April 2002.
5. Gallman, J.W., and Kroo, I.M., "Structural Optimization for Joined-Wing Synthesis", *Journal of Aircraft*, Vol. 33, No. 1, January-February 1996, pp. 214-223.
6. Nees, C., and Canfield, R., "Methodology for Implementing Fracture Mechanics in Global Structural Design of Aircraft", AIAA-96-1429-CP presented at the 37th AIAA/ASME/ASCE/AHS/ASC Structures, Structural Dynamics and Materials Conference ad Exhibit, Salt Lake City, UT, 15-17 April 1996.
7. Lin, H-H., Jhou, J., and Stearman, R., "Influence of Joint Fixiti on the Aeroelastic Characteristics of a Joined Wing Structure", AIAA Paper 90-0980, Proceedings of the 31st AIAA/ASME/ASCE/AHS/ASC Structures, Structural Dynamics and Materials Conference, Long Beach, CA, April 1990, pp. 1442-1454.
8. Livne, E., "Aeroelasticity of Joined-Wing Airplane Configurations: Past Work and Future Challenges – A Survey", AIAA-2001-1370, presented at the 42nd AIAA/ASME/ASCE/AHS/ASC Structures, Structural Dynamics and Materials Conference, Seattle, WA, 16-19 April 2001.

9. Lee, D., and Chen, P., "Non-linear Aeroelastic Studies on a Joined-Wing With Wing Buckling Effects", AIAA 2004-1944, presented at the 45th AIAA/ASME/ASCE/AHS/ASC Structures, Structural Dynamics and Materials Conference, palm Springs, CA, 19-22 April 2004.
10. Raymer, Daniel P. *Aircraft Design: A Conceptual Approach* (2nd Edition). Washington DC: American Institute of Aeronautics and Astronautics, Inc., 1992.
11. Roberts, R., "Sensor-Craft Analytical Certification", MS thesis, AFIT/GAE/ENY/04-M14. School of Aeronautics and Astronautics, Air Force Institute of Technology (AU), Wright Patterson AFB OH, March 2003 (ADA532552353).
12. Rasmussen, C., "Optimization Process For Configuration of Flexible Joined-Wing", MS thesis, AFIT/GAE/ENY/04-M14. School of Aeronautics and Astronautics, Air Force Institute of Technology (AU), Wright Patterson AFB OH, March 2004 (ADA57457117).
13. Viisoreanu, A., "Preliminary Sensorcraft Buckling Analysis", Aerodynamic Efficiency Improvements (AEI), The Boeing Company, 27 April 2005.
14. Fatta, G., "AEI Final Report", Aerodynamic Efficiency Improvements (AEI), The Boeing Company, 17 July 2006.
15. Dittmar, J., "Integrated Conceptual Design of Joined-Wing SensorCraft Using Response Surface Models", MS thesis, AFIT/GAE/ENY/07-D02, School of Aeronautics and Astronautics, Air Force Institute of Technology (AU), Wright Patterson AFB OH, November 2006 () .
16. 7.0_Model_Sim_Anal.ppt , Aerodynamic Efficiency Improvements (AEI), The Boeing Company, 17 July 2006.
17. ZAERO Version 7.3 User's Manual. MacNeal-Schwendler Corporation, 2005
18. ZAERO Version 7.3 Applications Manual. MacNeal-Schwendler Corporation, 2005

19. Lee, John M., *MSC.NASTRAN Version 69+ Linear Static Analysis User's Guide*. MacNeal-Schwendler Corporation, 1995.
20. Lee, Sang H., *MSC.NASTRAN Handbook for Nonlinear Analysis Version 67*. MacNeal-Schwendler Corporation, 1992.
21. Smith, S.C., Cliff, S.E., and Kroo, I.M., "The Design of a Joined-Wing Flight Demonstrator Aircraft", AIAA Paper 87-2930, AIAA/AHS/ASEE Aircraft Design, Systems and Operations Meeting, St. Louis, MO, 14-16 September 1987.
22. Kroo, I. M., Gallman, J. W., and Smith, S. C., "Aerodynamic and Structural Studies of Joined-Wing Aircraft," *Journal of Aircraft*, Vol. 28, No. 1, January-February 1991, pp. 74-81.
23. ZAERO Version 7.3 Theoretical Manual. MacNeal-Schwendler Corporation, 2005
24. MSC.Nastran 2004 Reference Manual. MSC Software Corporation

REPORT DOCUMENTATION PAGE				<i>Form Approved OMB No. 074-0188</i>
<p>The public reporting burden for this collection of information is estimated to average 1 hour per response, including the time for reviewing instructions, searching existing data sources, gathering and maintaining the data needed, and completing and reviewing the collection of information. Send comments regarding this burden estimate or any other aspect of the collection of information, including suggestions for reducing this burden to Department of Defense, Washington Headquarters Services, Directorate for Information Operations and Reports (0704-0188), 1215 Jefferson Davis Highway, Suite 1204, Arlington, VA 22202-4302. Respondents should be aware that notwithstanding any other provision of law, no person shall be subject to an penalty for failing to comply with a collection of information if it does not display a currently valid OMB control number.</p> <p>PLEASE DO NOT RETURN YOUR FORM TO THE ABOVE ADDRESS.</p>				
1. REPORT DATE (DD-MM-YYYY) 14 Jun 07	2. REPORT TYPE Master's Thesis	3. DATES COVERED (From – To) Jun 2006 – Jun 2007		
4. TITLE AND SUBTITLE Structural Stability of A Joined-Wing Sensorcraft			5a. CONTRACT NUMBER	
			5b. GRANT NUMBER	
			5c. PROGRAM ELEMENT NUMBER	
6. AUTHOR(S) Adams, Brandon, J., Ensign, USN			5d. PROJECT NUMBER	
			5e. TASK NUMBER	
			5f. WORK UNIT NUMBER	
7. PERFORMING ORGANIZATION NAMES(S) AND ADDRESS(S) Air Force Institute of Technology Graduate School of Engineering and Management (AFIT/EN) 2950 Hobson Way WPAFB OH 45433-7765			8. PERFORMING ORGANIZATION REPORT NUMBER AFIT/GAE/ENY/07-J01	
9. SPONSORING/MONITORING AGENCY NAME(S) AND ADDRESS(ES) Dr. Maxwell Blair 2210 8 th St. Room 220 Wright Patterson AFB, OH 45433-7531 Airforce Research Laboratory			10. SPONSOR/MONITOR'S ACRONYM(S) AFRL	
			11. SPONSOR/MONITOR'S REPORT NUMBER(S)	
12. DISTRIBUTION/AVAILABILITY STATEMENT APPROVED FOR PUBLIC RELEASE; DISTRIBUTION UNLIMITED.				
13. SUPPLEMENTARY NOTES				
14. ABSTRACT <p>This thesis employed a multi-disciplinary design approach to determine the structural stability of the Boeing Joined-Wing SensorCraft. Specifically, this thesis sought to characterize the free vibration modes, ensure a buckling safe design and determine the influence of the geometric and aeroelastic nonlinearities associated with this joined-wing design. The clamped free vibration modes were developed for a wind tunnel model and were compared to the free-free vibration modes, several differences were found. Linear static analyses were performed on numerous maneuver loads and gust conditions to determine the critical loading condition. The SensorCraft was then redesigned for the critical load case to be both panel and global buckling safe. The multi-disciplinary design process which incorporated both geometric nonlinearities and aeroelastic follower-force effects was then performed for the pre-gust trim and critical gust conditions. The resulting analysis showed that the deformations that resulted from the aerodynamic forces were not substantial enough to fully characterize the follower force effect. Furthermore this thesis demonstrates that the geometric and aeroelastic nonlinearities are not significant. However, for a fully optimized design incorporation of these coupled nonlinearities is critical.</p>				
15. SUBJECT TERMS Joined-Wing, Buckling, Follower Force Nonlinearities, Geometric Nonlinearities, Clamped Normal Modes, Free Normal Modes, Conformal Load Bearing Antenna Structure, Sensorcraft				
16. SECURITY CLASSIFICATION OF: U		17. LIMITATION OF ABSTRACT UU	18. NUMBER OF PAGES 129	19a. NAME OF RESPONSIBLE PERSON Dr. Robert Canfield (AFIT/ENY) 19b. TELEPHONE NUMBER (Include area code) 937-255-3636x.4723
Standard Form 298 (Rev: 8-98) <i>Prescribed by ANSI Std. Z39-18</i>				